### High Resolution Ion Sensing with Large-Area Graphene Field Effect Transistors at the Thermodynamic and Quantum Limits

Ibrahim Fakih



Department of Electrical and Computer Engineering McGill University Montréal, Québec, Canada

April 2020

Under the supervision of Professor Thomas Szkopek

A thesis submitted to McGill University in partial fulfillment of the requirements for the degree of Doctor of Philosophy.

© 2020 Ibrahim Fakih

#### Abstract

In this thesis, we present the large-area graphene based ion sensitive field effect transistor (ISFET) as an attractive candidate for overcoming the challenges in the ion sensing field. We present a signal to noise ratio model for ISFETs outlining the necessity for a Nernstian limited signal, as well as minimizing noise through maximizing the active sensing area, device carrier mobility, and capacitive coupling, in order to improve sensor resolution. While these parameters are key for any ISFET, graphene is optimal because it enables large-area devices with high charge-carrier mobility using a chemical vapor deposition growth technique that is economical in comparison with traditional semiconductor growth methods.

We demonstrate  $\sim \text{cm}^2$  graphene ISFETs for multiple ions with record sensing resolution for potentiometric sensors by saturating the physical limits of sensitivity, while exhibiting field-effect mobilities as high as 7000 cm<sup>2</sup>/Vs and device capacitances at the quantum limit  $\sim 1~\mu\text{F/cm}^2$  imposed by density of states.

For measuring pH, tantalum pentoxide  $Ta_2O_5$  or aluminum oxide  $Al_2O_3$  sensing layers were grown via atomic layer deposition (ALD). The large-area graphene is encapsulated with ultra-thin layers of parylene, a hydrophobic polymer, to protect the graphene from degradation and act as a seeding layer during ALD to ensure ultra-thin stochiometric oxide layers. We also are able to measure  $K^+$ ,  $Na^+$ ,  $NH_4^+$ ,  $NO_3^-$ ,  $SO_4^{2-}$ ,  $HPO_4^{2-}$  and  $Cl^-$  using ionophore membranes as sensing layers. Due to parylene encapsulation, the devices exhibit minimal hysteresis and remarkable stability over a 5 month period with

limited drift.

To overcome the challenge of poor selectivity, an ISFET array is developed, where each sensor is cross calibrated for interfering ions, and a series of Nikolskii-Eisenman equations is generated to solve for the ion concentrations, even in the presence of interfering ions. With this method, the ISFETs are accurate in multi analyte solutions to within  $\pm 0.01$  and  $\pm 0.05 \log$  concentration for cations and anions respectively. The performance of our ISFETs is more than sufficient for many real-time monitoring applications, where they are tested in a variety of beverages, blood, and in an aquarium.

### Abrégé

Dans cette thèse, nous présentons le transistor à effet de champ sensible aux ions (ISFET) à base de graphène à grande surface comme un candidat attrayant pour surmonter les défis dans le domaine de la détection des ions. Nous présentons un modèle de rapport signal/bruit pour les ISFET soulignant la nécessité d'un signal limité par l'équation de Nernst, ainsi que la minimisation du bruit en maximisant la zone de détection active, la mobilité des porteurs de charge et le couplage capacitif, afin d'améliorer la résolution du capteur. Bien que ces paramètres soient essentiels pour tout ISFET, le graphène est optimal car il permet des dispositifs de grande surface avec une mobilité des porteurs de charge élevée en utilisant une technique de croissance par dépôt chimique en phase vapeur qui est économique par rapport aux méthodes de croissance traditionnelles des semi-conducteurs.

Nous démontrons ISFETs de graphène  $\sim$  cm  $^2$  pour plusieurs ions avec une résolution de détection record pour les capteurs potentiométriques en saturant les limites physiques de la sensibilité, tout en exposant des mobilités à effet de champ pouvant atteindre 7000 cm $^2$ /Vs et l'appareil capacités à la limite quantique  $\sim$  1  $\mu$  F/cm $^2$  imposée par la densité des états.

Pour mesurer le pH, des couches de détection d'oxyde de tantale Ta<sub>2</sub>O<sub>5</sub> ou d'oxyde d'aluminium Al<sub>2</sub>O<sub>3</sub> ont été déposés par dépôt de couche atomique (ALD). Le graphène de grande surface est encapsulé avec des couches ultraminces de parylène, un polymère hydrophobe, pour protéger le graphène de la dégradation et agir comme une couche d'ensemencement pendant l'ALD pour assurer des oxydes stochiométriques ultra-minces. Nous pouvons également

mesurer  $K^+$ ,  $Na^+$ ,  $NH_4^+$ ,  $NO_3^-$ ,  $SO_4^{2-}$ ,  $HPO_4^{2-}$  et  $Cl^-$  en utilisant des membranes ionophores comme couches de détection. En raison de l'encapsulation du parylène, les dispositifs présentent une hystérésis minimale et une stabilité remarquable sur une période de 5 mois avec une dérive limitée.

Pour surmonter le défi d'une mauvaise sélectivité, un réseau ISFET est développé, où chaque capteur est étalonné de manière croisée pour les ions interférents, et une série d'équations Nikolskii-Eisenman est générée pour résoudre les concentrations ionique, même en présence d'ions interférents. Avec cette méthode, les ISFET sont exact dans les solutions multi-analytes à une concentration de  $\pm 0,01$  et  $\pm 0,05$  log pour les cations et les anions respectivement. Les performances de nos ISFET sont plus que suffisantes pour de nombreuses applications de surveillance en temps réel, où elles sont testées dans une variété de boissons, dans du sang et dans un aquarium.

### Acknowledgments

First and foremost, I would like to thank my supervisor, Professor Thomas Szkopek for the patient guidance, encouragement and advice he has provided me; he has made me grow and mature, both as a person and a researcher. His knowledge and experience are invaluable, and he is always available to share them and answer my questions.

I want to thank both Professor Nathaniel Quitoriano and Professor Songrui Zhao, for serving on my PhD supervisory committee, their advice and their guidance. I also want to thank Professor Viviane Yargeau for her advice on measuring ions of concern in water.

I also want to thank my colleagues in the lab, both past and present, who made my time in the lab more enjoyable and for their worthwhile discussion, and in particular those who contributed to the progress of the project: Oliver Durnan, Raed Abdo, Farzaneh Mahvash and Shadi Sabri.

I want to thank Donald Pavlasek and my brother Mustafa Fakih for helping with the design and machining the different measurement setups for our sensors. I thank Prof. Cerruti for giving access to her lab and equipment. I also thank Remi Wolowiec for the Ta<sub>2</sub>O<sub>5</sub> ALD at the University of Toronto. I thank Boutheina Ghaddab and Professor Mohamed Siaj at UQAM and Amaia Zurutuza, Alba Centeno and Ilargi Napal at Graphenea for providing us with graphene for the sensors.

I would also like to thank the Natural Sciences and Engineering Research Council of Canada, the William and Rhea Seath Foundation, and the Canada Research Chairs program for providing the financial resources to keep the project moving forward.

Finally, I thank my parents, sister, and brother for their encouragement and unconditional support. They are always there for me, and I am grateful for them.

## Contents

1	Intr	roduction	1
	1.1	Current Techniques for Measuring Ions	1
	1.2	The ISFET Concept	4
	1.3	Current Ion Sensitive Field Effect Transistors	5
	1.4	Graphene Ion Sensitive Field Effect Transistors	7
	1.5	Original Contributions	
	1.6	Thesis Organization	17
<b>2</b>	The	e ISFET Signal to Noise Ratio Model	20
	2.1	Sensor Terminology	21
	2.2	ISFET signal	22
		2.2.1 The site binding and Gouy-Chapman-Stern models	23
		2.2.2 The Nernstian Limit	26
	2.3	The ISFET Noise	27
	2.4	The Signal to Noise Ratio	31
3	pН	Sensing with Graphene ISFETs at the Nernstian Limit	34
	3.1	Graphene ISFET Fabrication	35
	3.2	Measurement Setup and Characterization	
		3.2.1 Conductance Measurements	37
		3.2.2 Capacitance Measurements	39
	3.3	The ISFETs' Sensitivities	40
	3.4	The ISFET Stability	46
4	pН	Sensing with Graphene ISFETs at the Quantum Limit	48
	4.1	Graphene ISFET Fabrication	49
	4.2	Capacitance measurements approaching the quantum limit	53
	4.3	Conductance measurements approaching the Nernstian limit $$	54
	4.4	ISFET resolution	57

Contents ix

5	Hig	h Resolution K <sup>+</sup> Sensing with Graphene ISFETs	60
	5.1	Graphene ISFET Fabrication	61
		5.1.1 Ionophore membrane preparation	61
		5.1.2 Device Preparation	
		5.1.3 Solution Preparation	
	5.2	Measurement setup and characterization	
		5.2.1 Capacitance Measurement	
		5.2.2 Conductance Measurement	
	5.3	ISFET sensitivity	
	5.4	ISFET Reliability and Reproduciblity	
		5.4.1 ISFET Selectivity	
	5.5	Conclusions	
6	Mu	ti Analyte Sensing with Graphene ISFETs	78
	6.1	The Nikolskii-Eisenman Formulasim	79
	6.2	Device Preparation	
		6.2.1 Ionophore Membrane Preparation	
	6.3	ISFETs Response	
		6.3.1 ISFET Sensitivities	
	6.4	ISFET Cross-Sensitivity	
	6.5	Multiple Analyte Sensing in Real-Time	
	6.6	Monitoring Ion Concentrations in Complex Environment	
7	Cor	clusions and Future Work	97
	7.1	Key Findings and Contributions	97
	7.2	Future work	
		7.2.1 Challenges with Parylene Encapsulation	
		7.2.2 Challenges with the Reference Electrode	
		7.2.3 Printed ISFETs	
Re	efere	nces	105

### List of Tables

1.1	ion concentration	3
2.1	Comparison of the different sources of voltage noise for typical ISFETs	30
5.1	Performance comparison of different potassium sensitive graphene ISFETs with and without parylene encapsulation. Reprinted with permission Elsevier © 2019	72
5.2	Measured potassium content in different liquids with "ISFET 2" and comparing values to a commercial potassium ISE (HI4114). Reprinted with permission Elsevier © 2019	76
6.1	Nikolskii selectivity coefficients for the cation ISFETs with respect to the different cations.	91
6.2	Nikolskii selectivity coefficients for the anion ISFETs with respect to the different anions	91
7.1	Comparison of the different analytical techniques for measuring ion concentration, including our graphene ISFETs	100

# List of Figures

1.1	Schematic comparison of a Si MOSFET and ISFET	4
1.2	The price of CVD grown graphene over the years. Figure has	
	been provided by Graphenea	8
1.3	(a) Semiconductor band structure. (b) Graphene band structure.	9
1.4	Electron mobility versus bandgap for different materials. The	
	data for graphene nanoribbons (GNR) and carbon nanotubes	
	(CNT) are theoretical, while for graphene, it includes both	
	theoretical and experimental. Reprinted with permission from	
	Springer Nature ©2010	11
1.5	(a) Schematic of back-gated graphene FET on a SiO <sub>2</sub> /n <sup>++</sup> Si	
	substrate. The doped Si acts as the gate. (b) A typical current-	
	voltage transfer characteristic curve for a graphene FET	11
1.6	(a) Schematic of top-gated graphene ISFET. (b) Shift in the	
	current-voltage transfer characteristics curve by increasing the	
	pH	14
2.1	Schematic showing an ISFET's sensitivity, detection limit and	
	resolution.	23
2.2	The site binding and Gouy-Chapman-Stern models, where a	
	metal oxide is in contact with an electrolytic solution. The M-	
	OH hydroxyl group accepts a proton, or donates a proton in an	
	acidic and basic solution respectively. An equal but opposite	
	charge appears in the electrolytic solution through two distinct	
	layers, the Helmholtz and diffusive layers	25
2.3	(a) The response of ISFETs with different selective layers to	
	changes in electrolyte pH. (b) The response of ISFETs with	
	different selective layers to changes in NaCl concentration at	
	constant pH 5.8. Reprinted with permission from Sensors and	
	Actuators B: Chemical © 1993	27

3.1	(a) Cross-sectional schematic of graphene ISFET for measuring	
	pH. (b) Optical image of a graphene ISFET. One of the devices	
	has the plastic vessel glued atop and mounted on a chip carrier	
	ready for measurement	36
3.2	(a) The electrical setup for measuring the graphene conductance	
	$G_{ds}$ for different pH solutions. $I_{ds}$ was monitored at a constant	
	bias $V_{ds}$ , while the electrolytic potential was varied through $V_{ref}$	
	and the back gate grounded. (b) $G_{ds}$ of a 2 nm Ta <sub>2</sub> O <sub>5</sub> ISFET	
	versus $V_{ref}$ at $V_{ds}$ =100 mV, for different pH solutions. Reprinted	
	with permission AIP Publishing LLC © 2014	38
3.3	(a) The electrical setup for measuring the graphene capacitance	
	$C_{dev}$ for different pH solutions. (b) The capacitance $C_{dev}$ as a	
	function of $V_{ref}$ for the same 2 nm Ta <sub>2</sub> O <sub>5</sub> ISFET in Fig. 3.2.	
	Reprinted with permission AIP Publishing LLC @ 2014	40
3.4	The potential $V_{np}$ of the minimum conductance and capacitance	
	for the different pH solutions measured with a 2 nm $Ta_2O_5$ IS-	
	FET. Reprinted with permission AIP Publishing LLC © 2014.	41
3.5	(a) $G_{ds}$ of a 150 nm Ta <sub>2</sub> O <sub>5</sub> ISFET versus $V_{ref}$ at $V_{ds}$ =100 mV,	
	for different pH solutions. The minimum conductance obtained	
	from parabolic fits are marked with a cross. Reprinted with	
	permission AIP Publishing LLC $\bigcirc$ 2014	43
3.6	Binding energy peaks of tantalum for our 40 nm and 150 nm	
	thick $Ta_2O_5$ measured using x-ray photoelectron spectroscopy.	43
3.7	(a) The sensitivity factor $\alpha$ of the different ISFETs with re-	
	spect to their Ta <sub>2</sub> O <sub>5</sub> thickness. (b) The intrinsic buffer capacity	
	$\beta_{int}$ of the same ISFETs with respect to their $\text{Ta}_2\text{O}_5$ thickness.	
0.0	Reprinted with permission AIP Publishing LLC @ 2014	45
3.8	The stability of a 5 nm Ta <sub>2</sub> O <sub>5</sub> ISFET with a pH 7 solution over	
	the course of two weeks. The ISFET response was stable to $\pm 1$	
	mV, or equivalently $\pm 0.05$ pH. Reprinted with permission AIP	16
	Publishing LLC © 2014	46
4.1	(a) Cross-sectional schematic of graphene ISFET for measuring	
	pH concentration. (b) Optical image of graphene ISFETs ready	
	for measurement. The left is on a $SiO_2/Si$ substrate, while the	
	right one is on a quartz substrate	51

4.2	(a),(b) Atomic force microscopy image of a 4 nm parylene C	
	layer on a Si substrate with around $\sim 2$ nm variation in unifor-	
	mity. (c) Binding energy peaks of chlorine in parylene C, tanta-	
	lum in Ta <sub>2</sub> O <sub>5</sub> , and aluminum in Al <sub>2</sub> O <sub>3</sub> grown on graphene and	
	measured using x-ray photoelectron spectroscopy. Reprinted	
		52
4.3	High-angle annular dark-field image of Ta <sub>2</sub> O <sub>5</sub> ISFET cross sec-	
	tion. Reprinted with permission American Physical Society © 2017.	52
4.4	Top-gate capacitance measurement of two different graphene IS-	
	FETs. One ISFET had 4 nm of parylene and 3 nm of Al <sub>2</sub> O <sub>3</sub> ,	
	while the other had 8 nm of parylene and 5 nm of $Ta_2O_5$ .	
	Reprinted with permission American Physical Society © 2017.	54
4.5	(a), (b) The electrical setup for measuring the graphene conduc-	
	tance $G_{ds}$ for different pH solutions for the two ISFET structures.	55
4.6	(a), (b) The normalized conductance $G_{ds}/G_{min}$ of 5 nm Ta <sub>2</sub> O <sub>5</sub>	
	and a 3 nm $Al_2O_3$ ISFET versus $V_{ref}$ , for different pH solu-	
	tions. Both forward and backward sweeps are shown for pH	
	3.22 to demonstrate the limited hysteresis of the ISFET. (c)	
	The changes in $V_{np}$ with different pH solutions are plotted for	
	both $Al_2O_3$ and $Ta_2O_5$ ISFETs. (d) FET mobility of the 5 nm	
	$Ta_2O_5$ ISFET for pH solutions of 2.75, 3.22, and 4.37 as well as	
	for a 3 nm Al <sub>2</sub> O <sub>3</sub> ISFET for pH solutions of 6.40, 7.01, and 7.51.	
		56
4.7	(a) The change in current $I_{ds}$ for a 3 nm $\text{Al}_2\text{O}_3$ ISFET with time	
	after adding 35 $\mu$ L of pH 3.22 to 1.2 mL of pH 2.75 at t = 60 s.	
	(b) Monitoring the change in acidity of 1.2 mL carbonated water	
	using a 5-nm Ta <sub>2</sub> O <sub>5</sub> ISFET by measuring the change in current	
	$I_{ds}$ with time. Reprinted with permission American Physical	
		58
5.1	3D model of potassium ionophore III, $C_{46}H_{70}N_4O_{18}$ , and of	
	valinomycin, $C_{54}H_{90}N_6O_{18}$ . Models were generating by <i>The</i>	
	Molview Project	62

5.2	(a) Cross-sectional schematic of graphene ISFET encapsulated with parylene and a layer of potassium ionophore membrane as a sensing layer on a Si/SiO <sub>2</sub> substrate. (b) Schematic of the	
	sensing device. The graphene FET is mounted to a PCB with indium. The PCB has an opening for the gate area to be in con-	
	tact with the liquid being measured. The K <sup>+</sup> ionophore mixture	
	is dropcasted into the opening. Epoxy is used to encapsulate	
	the back gate of the transistor. (c) An optical image showing	
	the front and back of a typical graphene ISFET mounted on	
	a PCB and ready for measurement. Reprinted with permission Elsevier © 2019	63
5.3	(a) Top gate capacitance $C_{dev}$ measurement of "ISFET 1" with	0.0
0.0	respect to the reference electrode $V_{ref}$ in a $10^{-2}$ M K <sup>+</sup> . (b)	
	Nyquist plot of "ISFET 1" in a $10^{-2}$ M K <sup>+</sup> solution. Reprinted	
	with permission Elsevier © 2019	66
5.4	(a) The electrical setup for measuring the graphene conductance	
	$G_{ds}$ . (b) An optical image showing an ISFET immersed in an	
	electrolytic solution and being measured	67
5.5	(a)(b) The current $I_{ds}$ of "ISFET 1" and "ISFET 2" with re-	
	spect to reference electrode $V_{ref}$ in a $10^{-2}$ M. Reprinted with	co
F 6	permission Elsevier © 2019	68
5.6	(a) Schematic of change in K <sup>+</sup> concentration between the ionophor membrane and bulk solution for two different concentrations	е
	K1 and K2. (b) Schematic of change in potential between the	
	ionophore membrane and bulk solution for two different concen-	
	trations K1 and K2	69
5.7	(a) The channel current, $I_{ds}$ , of ISFET 1 versus $V_{ref}$ , for different	
	$\dot{K}^+$ molar concentrations.(b) The changes in $V_{np}$ with different	
	K <sup>+</sup> solutions are plotted for ISFET 1. Reprinted with permission	
	Elsevier © 2019	70
5.8	(c) Continuous real-time measurement of $I_{ds}$ for ISFET 2 when	
	increasing K <sup>+</sup> molar concentrations by 1 decade step while keep-	
	ing $V_{ref} = 0$ V. (b) The linear response in $I_{ds}$ with different K <sup>+</sup>	
	solutions plotted for ISFET 2. Reprinted with permission Elsevier © 2019	71
5.9	(a) The ISFET current, $I_{ds}$ , for "ISFET 2" while varying the K <sup>+</sup>	11
0.0	concentration between $10^{-2}$ M and $0.5 \times 10^{-3}$ M. (b) The ISFET	
	current, $I_{ds}$ , for "ISFET 2" while varying the K <sup>+</sup> concentration	
	between $10^{-4}$ M and $9.75 \times 10^{-5}$ M. Reprinted with permission	
	Elsevier © 2019	73

<ul><li>5.10</li><li>5.11</li></ul>	(a) The ISFET current, $I_{ds}$ , for "ISFET 2", over a 24 hour period for $10^{-6}$ , $10^{-4}$ and $10^{-2}$ M K <sup>+</sup> solutions, which exhibits minimum drift of $\sim 25$ nA/hr. (b) The ISFET current, $I_{ds}$ , measured periodically over five months for $10^{-6}$ , $10^{-4}$ and $10^{-2}$ M K <sup>+</sup> concentrations. Reprinted with permission Elsevier © 2019. (a-d) The cross-sensitivity of "ISFET 1" with Na <sup>+</sup> , Ca <sup>2+</sup> , Mg <sup>2+</sup> , and NH <sub>4</sub> <sup>+</sup> . (e) A comparison of ISFET sensitivity with respect	74
	to its target ion $K^+$ and to interfering ions $Na^+$ , $Ca^{2+}$ , $Mg^{2+}$ , and $NH_4^+$ . Reprinted with permission Elsevier © 2019	75
6.1	(a), (b) Schematic of the fabrication process of the graphene ISFETs. (c) An optical image showing a the ISFETs at different stages of the fabrication process.	83
6.2	stages of the fabrication process	85
6.3	channel $I_{ds}$ for different electrolytic solutions	00
	measurement of $I_{ds}$ for the same Na <sup>+</sup> ISFET when increasing Na <sup>+</sup> molar concentrations by half decade steps while keeping $V_{ref} = 0V$	86
6.4	(a) The changes in $V_{np}$ for the different ISFETs with respect to concentrations of their respective target ions, with a linear fit to extract their voltage sensitivities. (b) The changes in $I_{ds}$ for the different ISFETs with respect to concentrations of their respective target ions, with a linear fit to extract their current	0.5
6.5	sensitivities	87
6.6	ent cation concentrations using the separate solution method The changes in $I_{ds}$ for the anion ISFETs with respect to different	88
6.7	anion concentrations using the separate solution method (a) The change in current $I_{ds}$ for all seven ISFETs measured concurrently in a complex electrolytic solution. The solution was spiked at different intervals with salt mixtures, illustrated by the arrows. (b), (c) The calculated concentrations of the cations and anions from the measured currents and solution of	89
	the nonlinear Nikolskii-Eisenman equations	93
6.8	The accuracy of our ISFET sensors by comparing the calculated concentrations in the shaded time window of Fig. 6.7 with the prepared concentrations as determined from the volume of the	
	mixtures and added salts	94

6.9	(a) An optical image of the ISFET array in the aquarium con-
	taining duckweed while measuring ion concentrations. (b) The
	ion concentrations in the aquarium with the duckweed over the
	course of three weeks

### Abbreviations

1D 1-dimensional2D 2-dimensional

AFM atomic force microscopy
ALD atomic layer deposition

CE counter electrode CNT carbon nanotubes

CVD chemical vapour deposition

DI de-ionized

DOS dioctyl sebacate

FET field effect transistor

GNR graphene nanoribbons

hBN hexagonal boron nitride

HEMTs high electron mobility transistors

ISE ion selective electrode

ISFET ion sensitive field effect transistor

IUPAC International Union of Pure and Applied Chemistry

MBE molecular beam epitaxy

xviii Abbreviations

MOSFET metal-oxide-semiconductor field effect transistor

PCB printed circuit board

PMMA Poly(methyl methacrylate)
PTFE polytetrafluoroethylene
PVC poly(vinyl chloride)

RE reference electrode rms root-mean-square

SNR signal to noise ratio

TEM transmission electron microscope

THF tetrahydrofuran

UV ultra-violet

WE working electrode

XPS X-ray photoemission spectroscopy

# Symbols

 $\hbar$ 

Plank's constant

a	ion activity; the ellective ion concentration
$a_i$	ion activity for primary ion
$a_j$	ion activity for interferring ion
$\alpha$	ISFET sensitivity factor, dimensionless number between 0 and 1
A	transistor channel area
$A_c$	unit cell Area
$eta_{int}$	intrinsic buffer capacity of ISFET sensing layer
$C_{dev}$	transistor capacitance from electrolytic gate to channel per unit area
$C_{diff}$	differential capacitance of the electrolytic solution
$C_{ox}$	capacitance of FET oxide
$C_q$	quantum capacitance
$C_{sl}$	capacitance of ISFET sensing layer
$\epsilon E_F$	dielectric constant of material Fermi energy
f	frequency
$g_m$ $G_{ds}$	transistor transconductance conductance of transistor channel

xx Symbols

$i_{IC}$	intrinsic current voltage noise of readout circuitry
$i_n$	current noise of ISFET
$I_{ds}$	transistor drain-source channel current
$I_i$	drain-source channel current for $i$ th ISFET
$I_i^0$	drain-source channel current constant for $i$ th ISFET for primary ion $i$
$I_{ij}^0$	drain-source channel current constant for $i$ th ISFET for interfering ion $j$
k	wave vector
$k_B$	Boltzmann's constant
$k_c$	confidence level factor for sensor resolution
$K_{ij}$	selectivity coefficient of the $i$ -selective sensor towards interfering ion $j$
L	transistor channel length
$m^*$	effective mass
$\mu$	carrier mobility
n	carrier density
N	noise spectral density
$N_0$	areal density of active sites in the sensitive layer contributing to charge fluctuation
$N_s$	number of surface hydroxyl sites in sensing layer per unit area
$\sigma_0$	surface charge density of sensing layer
$\sigma_{dl}$	double layer charge density in electrolytic solution
$\Theta^+$	the positively charged fraction of the surface hydroxyl sites $N_s$ at equilibrium
$\Theta^-$	the negatively charged fraction of the surface hydroxyl sites $N_s$ at equilibrium

Symbols xxi

p	momentum
$\rho(E)$	density of states
$pH_B$	pH and bulk electrolytic solution
$pH_s$	surface pH at oxide interface
q	elementary charge
$R_{ds}$	resistance of transistor channel
s	ISFET current sensitivity
$s_{ii}$	ISFET current sensitivity of the <i>i</i> -selective sensor towards its respective primary ion
$s_{ij}$	ISFET current sensitivity of the $i$ -selective sensor towards interfering ion $j$
S	ISFET sensitivity
t	thickness of ISFET sensing layer
au	carrier mobility
T	temperature
$v_{BN}$	brownian voltage noise of ISFET
$v_{CF}$	charge fluctuation voltage noise of ISFET
$v_{DP}$	dipole voltage noise of ISFET
$v_F$	Fermi velocity, $\sim 10^6 \text{ m/s}$
$v_{IC}$	intrinsic noise voltage noise of readout circuitry
$v_{JN}$	Johnson voltage noise of ISFET
$v_n$	voltage noise of ISFET
$V_{ds}$	transistor drain-source bias
$V_{gs}$	transistor gate-source bias
$V_{np}$	transistor gate voltage where minimum point of conduction, neutrality point, occurs
$V_{np-c}$	transistor gate voltage where minimum point of capacitance occurs
$V_{np-g}$	transistor gate voltage where minimum point of conduction occurs
$V_{ref}$	reference electrode voltage

xxii Symbols

$V_t \\ \psi_0 \\ \psi_0^0$	transistor threshold voltage surface potential at the sensing layer/electrolyte interface initial surface potential at the sensing layer/electrolyte interface
W	transistor channel width
$x_H$	Helmholtz layer length
$\gamma  an \delta$	white noise parameter of the device loss tangent of the sensitive layer
$z \ z_i \ z_j \ z_j$	valency of element valency of primary ion valency of interfering ion
Z	impedance

### Chapter 1

### Introduction

### 1.1 Current Techniques for Measuring Ions

Measuring very low ion concentrations in liquids is important in a wide range of applications, including genome sequencing [1], medical diagnostics [2], environmental monitoring [3, 4, 5], and industrial process control [6, 7]. There are many different techniques to measure ion concentrations depending on the application; the most common techniques involve either chromatography, spectrophotometry or potentiometry, and each has their advantages and disadvantages.

Ion chromatography measures concentration of ionic species by injecting the electrolytic solutions into an eluent stream and separating the ionic species into columns based on their relative interaction with a resin. The concentration is determined by the retention time of the ion in the resin [8]. Spectrophotometry measures the intensity of light absorbed after it passes through a sample solution. Based on the wavelength dependent absorption spectra, ion concen-

trations can be determined. Indicator dyes are sometimes used to improve accuracy [9]. The main advantages of both these techniques are their reliability, high selectivity, very good accuracy and precision [10, 11]. However, both techniques are time consuming, rely on large costly equipment, and require experts to operate, making them unpractical for either quick, long-term or real-time measurements.

In the particular case of water quality monitoring, ion concentrations are insufficiently measured in both space and time due to these limitations. For example, to monitor the 500 km long St. Lawrence river, water samples are taken to labs from 10 locations once every few weeks to be measured by either chromatography or spectroscopy [12].

On the other hand, potentiometric sensors are more attractive for such applications because of their compactness, ease of integration with electronics, and capacity for real-time, on-site measurement. They measure the potential difference between two electrodes, a working and reference electrode, in the presence of an ionic solution. Most potentiometric sensors are based on the ion selective electrode (ISE) which rely highly selective membranes in the form of either a glass or ionophore mixture. Ions reversibly bind to the ISE to create an electric potential whose strength is dependent on ion concentration [13, 14].

Recently, there is increased interest in the ion sensitive field effect transistor (ISFET) which directly integrates an ISE with a transistor, thereby minimizing noise, minimizing device size and making use of planar manufacturing methods [15]. The gate of an ISFET includes an ion sensitive layer that enables ion binding events to modulate surface potential and thus transistor

channel conduction [16]. Arrays of up to 10<sup>7</sup> micro-scale silicon based ISFETs sensitive to pH are presently fabricated using standard CMOS processes, and the ion sensitive layer is added through back end of line processing, motivated by solid state genome sequencing [1].

Despite the advantages of an ISFET over chromatography and spectrophotometry, they have yet to make an impact on most real world applications due to their inferior selectivity, accuracy and resolution. A comparison between the different state-of-the-art techniques is found in table 1.1 [10, 11, 17]. Note that the price only compares that of the equipment and does not include operating costs. The cost for potentiometry includes a single ISE and a meter. The meter costs around \$1,500 and can be used for multiple ISEs.

**Table 1.1**: Comparison of the different analytical techniques for measuring ion concentration.

Technique	Selectivity	Resolution	Detection limit	Accuracy	Price
Chromatography	High	$10^{-4} \log M$	$10^{-10} \; \mathrm{M}$	$\pm$ 0.03 log M	> \$50,000
Spectrophotometry	High	$10^{-4} \log M$	$10^{-10} { m M}$	$\pm$ 0.03 log M	> \$10,000
Potentiometric ISE with meter	Poor	$10^{-2} \log M$	$10^{-6} \text{ M}$	$\pm$ 0.05 log M	\$2,000

The comparatively poor ISFET selectivity arises from the non-ideal ion selective membranes, while limitations in accuracy arise from contamination of the liquid junction reference electrode over time [18]. Recent work with ion-gel reference electrodes has improved accuracy by at least one order of magnitude [18]. The limitations in precision and resolution arise from the combination of a thermodynamically limited response [13], and noise arising from charge fluctuation in the working electrode [19].

Therefore, the challenge is to develop ISFETs that approach the resolution,

accuracy and selectivity of chromatographic and spectrophotometric methods. The ISFET must saturate the physical limits of sensitivity, while minimizing sources of noise and drift.

### 1.2 The ISFET Concept

The ISFET is very similar to a metal-oxide-semiconductor metal-oxide-semiconductor field effect transistor (MOSFET), with the gate separated from the device in the form of a reference electrode and inserted in an aqueous solution to be measured. The solution is directly in contact with a selective ion sensitive layer, as illustrated in Fig. 1.1.

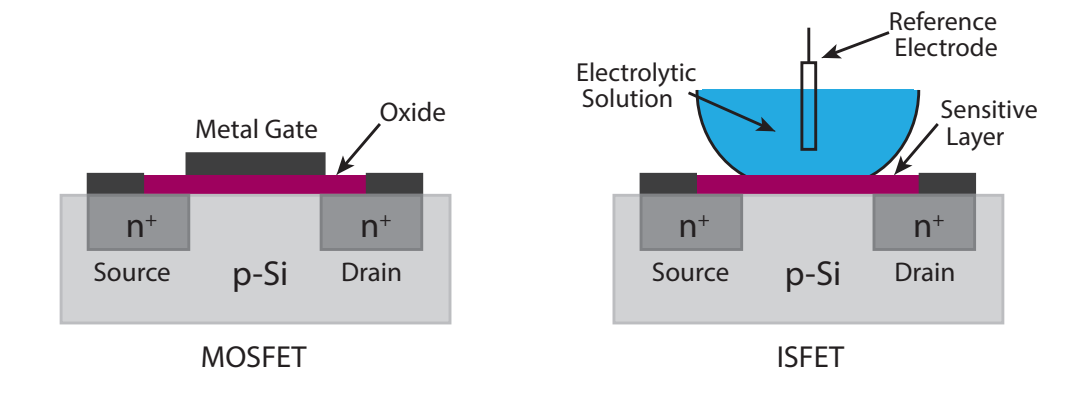


Fig. 1.1: Schematic comparison of a Si MOSFET and ISFET.

In the case of a MOSFET, applying a gate voltage  $V_{gs}$  above a threshold voltage  $V_t$  creates an inversion layer in the semiconductor and a channel for the current to flow between the source and drain. The threshold voltage depends on the difference between the metal gate and silicon workfunctions. In an ISFET system, the same concept still applies; however, since there is no metallic

gate,  $V_t$  is a function of the surface potential  $\psi_0$  at the oxide/electrolyte interface instead of the metal workfunction. The surface potential  $\psi_0$  varies with ion concentration a according to Bergveld's model [15, 16, 20]:

$$\frac{\delta\psi_0}{\delta\log[a]} = -\ln 10 \frac{k_B T}{zq} \alpha \tag{1.1}$$

where  $k_B$  is Boltzmann's constant, T is the absolute temperature, q is the electron charge, z is the valency of ion being measured and  $\alpha$  is a dimensionless sensitivity factor between 0 and 1 that depends on the ISFET sensitive layer. In the ideal scenario, where  $\alpha = 1$ , the sensitivity of an ISFET  $\delta\psi_0/\delta\log{[a]}$  is thermodynamically limited to -59.2 mV/decade of ion concentration at 298 K for an ion with valency 1; this is also known as the Nernstian sensitivity. Sub-Nernstian sensitivities arise from less than ideal ( $\alpha < 1$ ) sensitive layers [15, 20]. With a thermodynamically limited signal, ISFETs need to be further investigated in an effort to reduce noise and improve the resolution of potentiometric sensors so as to be on par with chromatography and spectrophotometry.

#### 1.3 Current Ion Sensitive Field Effect Transistors

Most commercial ISFETs are silicon based since they can easily be fabricated using standard  $\mu$ m CMOS processes, where ion sensitive layers are added through back end of line processing [1, 21]. However this comes with numerous challenges that increase noise and effect resolution. It has been reported that ISFETs get noticeably noisier as they get smaller, resulting in resolutions of 0.02 log concentration for  $\mu$ m sized ISFETs [1, 21, 22]. Another challenge is

due to back end of the line processing and the multiple layers, the ISFET gate becomes an extended gate which further introduces noise and drift [21]. The additional layers will also decrease the gate capacitance and attenuate channel modulation [21], as well as increase 1/f noise [22].

In efforts to reduce noise, other materials and structures have been studied. Si nanowires ISFETs have been developed due to their large surface to volume ratio [23, 24, 25]. Despite near Nernstian limited sensitivities, the IS-FETs report a resolution of 0.016 log concentration [25]. AlGaN/GaN high electron mobility transistors (HEMTs) as ISFETs for nitrate ions have also been studied as an alternative to Si based ISFETs due to diminishing charging effects and higher carrier mobilities [26]. Detection limits down to  $10^{-6}$ have been reported with a Nernstian limited response; however, they exhibited a resolution no lower than 0.2 log concentration. In ISFETs grown via molecular beam epitaxy (MBE) for measuring pH also exhibit a Nernstian response, but with resolutions of only 0.03 log concentration [27]. Exfoliated MoS<sub>2</sub> ISFETs for measuring pH were studied due to their relatively low subthreshold voltage swing and high on/off current ratios [28, 29]. The ISFETs demonstrate remarkable stability; however, they also report a relatively poor resolution of 0.02 log concentration. Carbon nanotubes as the transducing layer of ISFETs has also been demonstrated for K<sup>+</sup> ions [30]. Even though they achieve a detection limit of  $10^{-8}$  M, the ISFET fails for concentrations above  $10^{-5}$  M; furthermore, resolutions no lower than 0.02 log concentration are observed. Despite the efforts of the ISFET community to reduce noise and improve resolution through different devices, ISFETs have yet to achieve their full potential, and further devices need to be explored in order to realize high resolution sensing.

#### 1.4 Graphene Ion Sensitive Field Effect Transistors

Graphene field effect transistors are very attractive candidates for potentiometric sensing due to the ideal coupling between mobile charge carriers and surface potential, high charge carrier mobility (and, thus, low Johnson noise [31]) and a relatively inexpensive fabrication process for large-area devices. Since the first graphene FET was demonstrated in 2004 [32], researchers have been working on realizing its full potential and translating its unique properties to sensing applications in the external environment.

Graphene is a single layer of carbon atoms in a two-dimensional hexagonal lattice. It is the basic structural element of other carbon allotropes, including graphite, carbon nanotubes, and fullerenes. Graphite was first discovered in 1565 by Abraham G. Werner and used to manufacture pencils, but it was not until 2004 that graphene was first isolated by A. Geim and K. Novoselov from the University of Manchester [32]. They exfoliated the  $\sim \mu m$  sized graphene from graphite using adhesive tape, and their work resulted in the 2010 Nobel prize for physics for groundbreaking experiments regarding the two-dimensional material graphene [33].

As the interest in graphene increased due to its properties, major advancements in the synthesis of large-area graphene have been made through epitaxial growth on silicon carbide [34] and chemical vapour deposition (CVD) of carbon on transition metals [35]. Large scale processing is now available with 8 inch

### CVD Graphene price (€cm²)

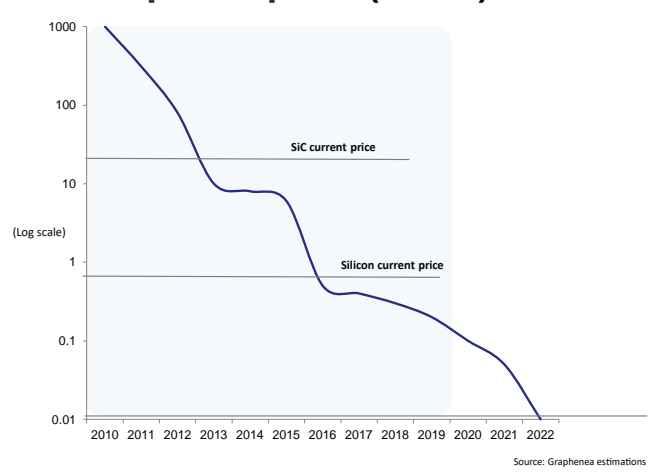


**Fig. 1.2**: The price of CVD grown graphene over the years. Figure has been provided by Graphenea.

graphene wafers [36] as well as 100 meter long graphene with roll-to-roll methods [37], making it more practical for commercial applications. Fig. 1.2 shows the evolution of the price of CVD grown graphene as reported by Graphenea. The price includes the cost of production and transfer to final substrate. The cost of graphene is already less than silicon carbide and silicon wafers per unit area, and it is expected to be less than  $\leq 0.40/\text{cm}^2$  by the end of 2021.

Unlike conventional semiconductors, graphene is a zero-gap material, with the valence and conductance bands meeting at the Dirac point, as seen with the band structures in Fig. 1.3. The energy bands follow a linear dispersion relation  $E = pv_F = \hbar k v_F$ , where p is momentum,  $\hbar$  is the reduced Planck constant, k is the wave vector and  $v_F$  is the Fermi velocity  $v_F \sim 10^6$  m/s. The linear dispersion is due to graphene's crystal structure and sub-lattice symmetry. Consequently, graphene's charge carriers behave as if they are

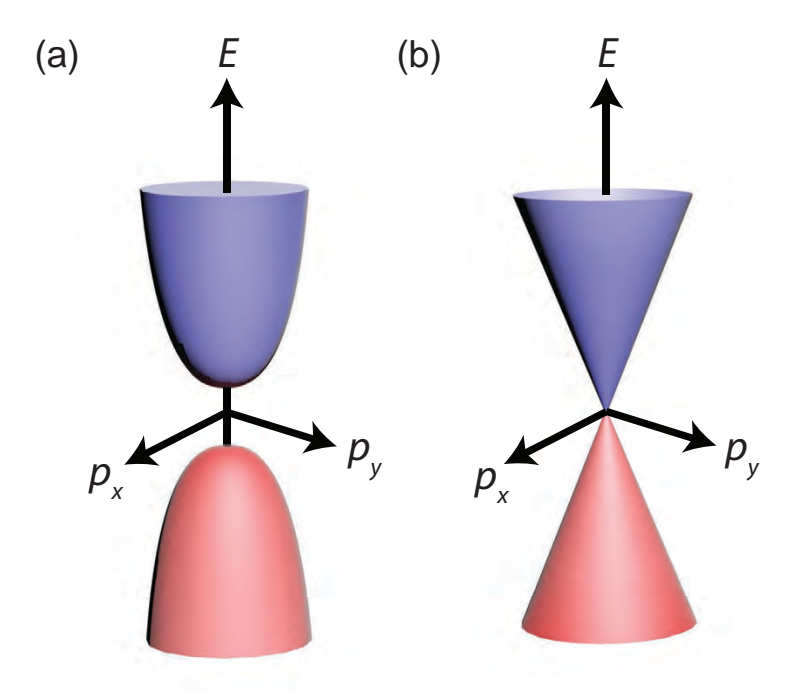


Fig. 1.3: (a) Semiconductor band structure. (b) Graphene band structure.

massless relativistic particles with a constant Fermi velocity  $v_F$ , unlike carriers in conventional semiconductors which are massive.

Close to the Dirac point, the density of states per unit cell is given by  $\rho(E)$   $= \frac{2A_c}{\pi} \frac{|E|}{v_f} \text{ where } A_c \text{ is the unit cell area [38, 39]. Under thermal equilibrium}$ and no applied electric field, the Fermi energy lies at the Dirac point and the density of states is zero. Similar to most 1-dimensional (1D) and 2-dimensional (2D) materials, a quantum capacitance  $C_q = q^2 \delta n/\delta E_F$  arises from the density of states  $\delta n/\delta E_F$ , and in the case of graphene  $C_q = q^2 2E_F/\pi(\hbar v_F)^2$  in the extrinsic limit[38], which is of the order of  $\sim 1\mu\text{F/cm}^2$  in a typical experimental scenario [40].

The massless relativistic particles of graphene coupled with low scattering effects in the material result in very high carrier mobilities  $\mu = q\tau/m^*$ ,

where  $\tau$  is the carrier scattering time, and  $m^*$  is the carrier effective mass. For graphene, the effective mass is  $m^* = E_F/v_F^2$ , where  $E_F$  is the Fermi energy. The dominant scattering mechanisms in graphene are electron-phonon scattering and surface-roughness scattering. In general, a smaller band gap correlates with a smaller effective mass, which in turn correlates to a higher carrier mobility. Consequently, graphene is theoretically predicted to have room temperature mobilities of 200,000 cm<sup>2</sup>/V·s at a carrier density of  $10^{12}$  cm<sup>-2</sup> on SiO<sub>2</sub> substrates [41]. Experimentally, exfoliated graphene encapsulated with WSe<sub>2</sub> had mobilities of 300,000 cm<sup>2</sup>/Vs at a carrier density of  $10^{12}$  cm<sup>-2</sup>, while mobilities upto 30,000 cm<sup>2</sup>/Vs were measured at room temperature for CVD grown graphene encapsulated with hexagonal boron nitride (hBN) [42]. On the other hand, Si MOS devices have mobilities of only 200 cm<sup>2</sup>/Vs. Fig. 1.4 compares the mobility of graphene (theoretical and experimental) to other materials [43].

In terms of devices, the graphene FET is a three terminal device with either a back or top gate. Back-gated devices typically consist of graphene on a 300 nm SiO<sub>2</sub> dielectric and doped silicon substrate as the gate. The standard 300 nm SiO<sub>2</sub> dielectric is optimal for distinguishing the graphene visually due to Fabry-Perot interference, which enhances optical reflection [44]. Such back-gated devices are great for extracting graphene properties and proof-of-concept demonstrations; however, they suffer large parasitic capacitances and are very difficult to integrate for analytical applications [43]. Top gated graphene are much more practical, especially for sensing applications. Dielectrics and contacts are deposited onto the graphene after its transfer to a substrate.

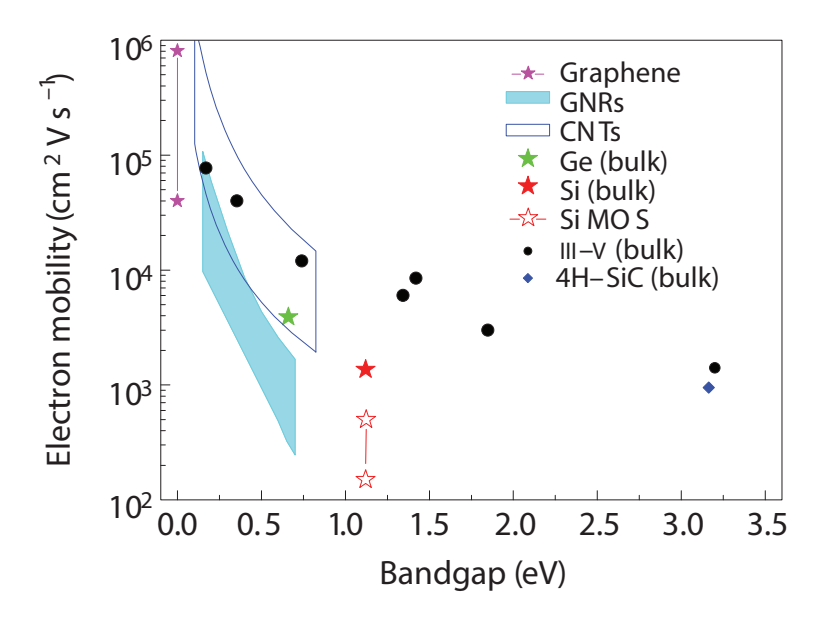
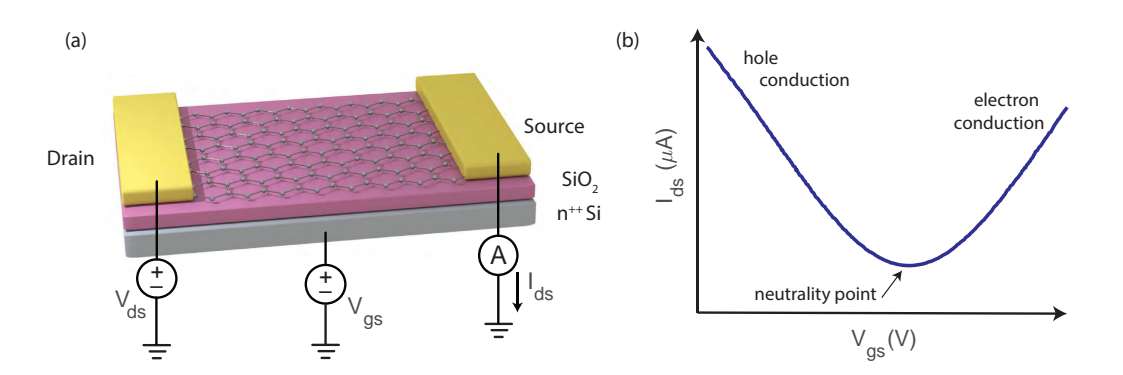


Fig. 1.4: Electron mobility versus bandgap for different materials. The data for GNR and CNT are theoretical, while for graphene, it includes both theoretical and experimental. Reprinted with permission from Springer Nature ©2010.



**Fig. 1.5**: (a) Schematic of back-gated graphene FET on a  $SiO_2/n^{++}$  Si substrate. The doped Si acts as the gate. (b) A typical current-voltage transfer characteristic curve for a graphene FET.

Applying a gate bias  $V_{gs}$  induces charges  $(C \cdot V_{gs})$  of opposite polarity in the graphene similar to a capacitor and moves the Fermi level  $E_F$ . A positive bias  $(V_{gs} > 0)$  increases the electron density in the graphene channel, while a negative bias  $(V_{gs} < 0)$  increases the hole density. This behavior gives rise to a unique current-voltage transfer characteristic with ambipolar conduction, as seen in Fig. 1.5. The minimum point of conduction is the Dirac or neutrality point. The gate voltage at which the neutrality point  $V_{np}$  occurs depends upon the workfunction of the gate and the graphene as well as any doping of the graphene induced from the substrate or surface potential [43]. In general, a smaller band gap material implies a smaller on/off current ratio; for the graphene FET, the conductance never turns off due to the lack of a band gap, and while this might be a problem for some applications, it is not an issue for sensing.

Most mechanisms for sensing with graphene FETs lead to a change graphene conduction ( $\sigma = \mu \cdot C \cdot (V_{gs} - V_{np})$ ) and a transformation of the transfer characteristic curve. Electrostatic gating is the most common mechanism, where a target analyte binds to an insulating surface layer to change the gate potential, thereby moving the graphene Fermi level and shifting the transfer curve [45]. Another mechanism requires the direct adsorbtion of target analytes onto the graphene surface, acting as either acceptors or donors, and leading to a direct charge transfer between the analyte and graphene; this modifies the graphene electrical conductivity. The Manchester group, led by K. Novoselov, have demonstrated resolutions down to a single gas molecule using this technique [31]; however, it is very difficult to differentiate between molecules, and

have very poor selectivity. Graphene conductance can also be modified by modulating the gate capacitance. Sensing layers on the graphene can adsorb molecules, modifying its permittivity, or dielectric constant, to alter the gate capacitance [46]. Another sensing mechanism relies on modulating the carrier mobility to alter the graphene conductance. Carrier mobility changes in graphene can be induced by changes in scattering by charged impurities [47], and target analytes on the surface can screen the effect of those charged impurities [48, 49]. Femtomolar detection limits of bio-molecules have been achieved with graphene FETs by mobility modulation.

In the case of an ISFET, sensing occurs by electrostatic gating. The ion sensitive layer is deposited on top of the graphene, and the change in surface potential  $\psi_0$  at the sensitive layer/electrolyte interface shifts the graphene Fermi level by  $\Delta E_F = q\Delta\psi_0$ . Therefore,  $\Delta\psi_0$  can be directly measured from the shift in the  $V_{np}$  as seen in Fig. 1.6. For the particular case of pH, increasing the H<sup>+</sup> concentration of the electrolytic solution will result in a more negative potential  $V_{np}$  to reach charge neutrality. Considering the Nernst equation eq. 1.1, the shifts in  $V_{np}$  should ideally be 59.2 mV/pH at room temperature. However, graphene ISFETs have not until recently been able to replicate Si ISFETs sensitivities and operate at the thermodynamic Nernstian limit [50, 51, 52, 53, 54]. As a result, graphene ISFETs have only recently realized their full potential to match spectrophotometric and chromatographic techniques in terms of resolution, accuracy and selectivity.

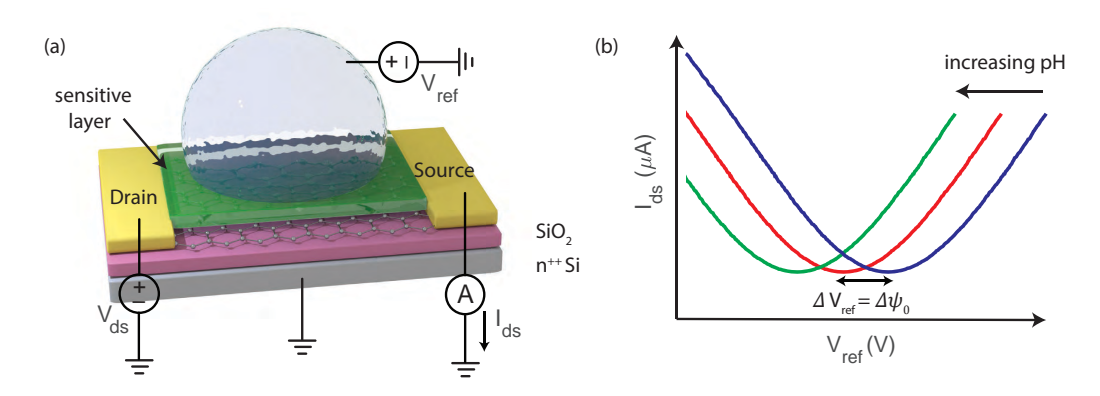


Fig. 1.6: (a) Schematic of top-gated graphene ISFET. (b) Shift in the current-voltage transfer characteristics curve by increasing the pH.

### 1.5 Original Contributions

This thesis explores the potential of graphene FETs for ion sensing, in order to address the biggest challenges of potentiometric ion sensors: resolution and selectivity. The following original contributions to knowledge are made:

- 1. Identification of large device area, high carrier mobility and large device capacitance as ways to reduce sensor noise.
- 2. Nernstian limited pH response using parylene C as a seeding layer for atomic layer deposition of stochiometric metal oxide sensing layers.
- 3. Retention of high graphene mobility in sensors using parylene C as an encapsulation layer.
- 4. Identification of the quantum capacitance limit, and using this to design ultra-thin sensing layers, achieving 0.3 mpH resolution, 10 times better than state of the art potentiometric sensors.

- 5. Extension of graphene ISFET concept to sense K<sup>+</sup>, Na<sup>+</sup>, NH<sub>4</sub><sup>+</sup>, NO<sub>3</sub><sup>-</sup>,  $SO_4^{2-}, HPO_4^{2-} \text{ and } Cl^-.$
- 6. Application of the Nikolskii-Eisenman formulasim to account for ISFET cross-sensitivity, and calculating the ion concentration in multi-analyte solutions, resulting  $\pm 0.05 \log$  concentration accuracy.

With that, the graphene ISFETs demonstrate remarkable resolution, accuracy, and selectivity, all on par with state-of-the-art chromatographic and spectrophotometric techniques, while at the same time, being capable of measuring ions in real-time. The performance is more than sufficient for many real-time applications, including real-time water quality monitoring [3].

The publications resulting from the work presented in this thesis are:

- I. Fakih, S. Sabri, F. Mahvash, M. Nannini, M. Siaj and T. Szkopek, 'Large area graphene ion sensitive field effect transistors with tantalum pentoxide sensing layers for pH measurement at the Nernstian limit', Appl. Phys. Lett. 105, 083101 (2014).
  - F. Mahvash grew the graphene via CVD under the supervision of M. Siaj.
  - I. Fakih fabricated, characterized and analyzed the graphene ISFETs under the supervision of T. Szkopek. S. Sabri contributed to the ISFET design, and the understanding of Bergveld's model. M. Nannini also contributed to the ISFET design. I. Fakih and T. Szkopek wrote the manuscript.
- 2. I. Fakih, F. Mahvash, M. Siaj and T. Szkopek, 'Sensitive precise pH measurement with large-area graphene field-effect transistors at the quantum-

16 Introduction

capacitance limit', Phys. Rev. Applied. 8, 044022 (2017).

- F. Mahvash grew the graphene via CVD under the supervision of M. Siaj.
- I. Fakih fabricated, characterized and analyzed the graphene ISFETs under the supervision of T. Szkopek. I. Fakih and T. Szkopek wrote the manuscript.
- I. Fakih, A. Centeno, A. Zurutuza, B. Ghaddab, M. Siaj and T. Szkopek, 'High resolution potassium sensing with large-area graphene field-effect transistors', Sensors and Actuators B: Chemical. 291, 89-95 (2019).
  - B. Ghaddab grew the graphene via CVD under the supervision of M. Siaj.
  - A. Centeno and A. Zurutuza provided the graphene from Graphenea.
  - I. Fakih designed, fabricated, characterized and analyzed the graphene ISFETs under the supervision of T. Szkopek. I. Fakih and T. Szkopek wrote the manuscript.
- I. Fakih, O. Durnan, F. Mahvash, I. Napal, A. Centeno, A. Zurutuza and T. Szkopek, 'Multi ion sensing with high resolution large area graphene field effect transistors', Under Review (2019).
  - I. Napal, A. Centeno and A. Zurutuza provided the graphene from Graphenea. I. Fakih did the wafer scale processing of the ISFETs, fabricated and characterized the K<sup>+</sup>, Na<sup>+</sup>, HPO<sub>4</sub><sup>2-</sup>, NO<sub>3</sub><sup>-</sup> and SO<sub>4</sub><sup>2-</sup> ISFETs. O. Durnan fabricated and characterized the NH<sub>4</sub><sup>+</sup>, NO<sub>3</sub><sup>-</sup>, and SO<sub>4</sub><sup>2-</sup> ISFETs. F. Mahvash fabricated and characterized the Cl<sup>-</sup> ISFET. I. Fakih conducted the multi-analyte experiments and solved for the Nikolskii-Eisenman equations with input from O. Durnan. I. Fakih

and O. Durnan conducted the aquarium measurements. This work was done under the supervision of T. Szkopek. I. Fakih and T. Szkopek wrote the manuscript.

This work has also resulted in a patent application:

US 62/574,420, "Graphene-based sensor and method of fabricating same",
 I. Fakih and T. Szkopek.

#### 1.6 Thesis Organization

This thesis will adopt the following structure:

#### Chapter 2:

Bergveld's theory, along with the site binding and Gouy-Chapman-Stern models, are introduced to illustrate the origins of the thermodynamic Nernstian limit. A simple model for the resolution and signal to noise ratio of an ISFET is presented, highlighting the key parameters to reducing the minimum resolvable change in ion concentration.

#### Chapter 3:

Large-area graphene ISFETs using tantalum pentoxide (Ta<sub>2</sub>O<sub>5</sub>) sensing layers of varying thickness are investigated. A pH sensitivity approaching the Nernstian limit is achieved for the first time with graphene ISFETs.

#### Chapter 4:

Based on the ISFET signal to noise ratio (SNR) model, large-area graphene ISFETs with ultra-thin oxide sensing layers are fabricated to achieve

18 Introduction

record pH sensing resolutions. An organic polymer (parylene C) is used to encapsulate the graphene and act as a seeding layer for the atomic layer deposition of the oxide.

#### Chapter 5:

The graphene pH ISFET is expanded upon to measure potassium ions using an ionophore mixture as the sensitive layer. The ISFETs demonstrate record detection limits and resolution as well as remarkable stability and reversibility in real-time measurements. The ISFETs were also tested in a variety of multi-solute specimens, including beverages and blood.

#### Chapter 6:

An array of graphene ISFETs is presented for measuring different ions concurrently in real-time. Ionophore mixtures for  $K^+$ ,  $Na^+$ ,  $NH_4^+$ ,  $NO_3^-$ ,  $SO_4^{2-}$ ,  $HPO_4^{2-}$  and  $Cl^-$  are used as sensitive layers for each individual ISFET. The Nikolskii-Eisenman equation, which accounts for ion interference, is presented. The ion concentrations are calculated to a remarkable accuracy and resolution. The sensors were tested by monitoring the ion concentrations in an aquarium with aquatic plants which absorbed different ions to sustain their growth.

#### Chapter 7:

A synopsis of the work is provided which includes the findings and contributions reported in this thesis. Future work is also presented for further studying and improving the ISFETs performance and capabilities for real-time monitoring applications.

### Chapter 2

# The ISFET Signal to Noise Ratio Model

One of the biggest challenges with ion sensing field effect transistors (IS-FETs) is the  $\sim 100$  times poorer resolution compared to chromatographic and spectrophotometric techniques. The minimum resolvable ion concentration is directly related to the signal of an ISFET and the noise associated to the device: the signal to noise ratio (SNR). With a thermodynamically limited signal, it is critical to reduce the noise associated with an ISFET.

This chapter will first discuss the thermodynamic limited response of an ISFET, and then explore the different sources of noise in an ISFET setup. A simple model for the SNR will be presented highlighting the key parameters for reducing the minimum resolvable change in ion concentration: maximizing area, mobility and capacitance. While these parameters are key for any ISFET, graphene is optimal because it enables large-area devices with high

charge-carrier mobility using a chemical vapor deposition growth technique that is economical in comparison with traditional semiconductor growth methods. Some of the work presented in this chapter has been published in a peer reviewed journal:

I. Fakih, F. Mahvash, M. Siaj and T. Szkopek, 'Sensitive precise pH measurement with large-area graphene field-effect transistors at the quantum-capacitance limit', Phys. Rev. Applied. 8, 044022 (2017).

#### 2.1 Sensor Terminology

The ISFET response to change in ion concentration is determined by measuring either the change in surface potential  $\Delta \psi_0$  at the sensitive layer/ electrolyte interface through changes in neutrality point potential  $V_{np}$ , or the change in channel current  $\Delta I_{ds} = g_m \Delta \psi_0$ .  $g_m$  is the ISFET transconductance. Owing to the zero bandgap of graphene, it is not possible to drive the graphene FET into saturation, and thus the  $g_m$  is that of a conventional FET in the triode regime of operation:

$$g_m = \frac{\partial I_{ds}}{\partial \psi_0} = \frac{W}{L} \mu C_{dev} V_{ds} \tag{2.1}$$

where W is the channel width, L is the channel length,  $\mu$  is the field effect mobility,  $C_{dev}$  is capacitance of the device from electrolytic gate to channel per unit area, and  $V_{ds}$  is source-drain dc bias.

According to the Nernst equation eq. 1.1, a linear response is expected between the log of ion concentration and  $\psi_0$ . Therefore, the ISFET sensitivity

(S) is the slope of the linear response, as seen in Fig. 2.1.

ISFETs start to loose sensitivity towards their target ion at lower ion concentrations. The concentration where the ISFET's response deviates from the linear slope is its detection limit. This occurs due to the perturbation of the interfacial sample activity by the sensing layer [14].

The ISFET's resolution is the smallest change it can detect in the quantity that it is measuring. This depends on both the sensor's signal and the noise associated it, and according to the International Union of Pure and Applied Chemistry (IUPAC) [55].

resolution = 
$$k_c \frac{\text{noise}}{S}$$
 (2.2)

where  $k_c$  is a confidence level factor, and noise and sensitivity S can either be expressed in terms of current or voltage. When  $k_c$  is set to 3, a confidence level of 90% is achieved, while  $k_c = 5$  achieves a confidence level of 99.6% [55].

An ISFET's accuracy is the closeness of agreement between a measurement and the true value [55]. An ISFET's precision is the closeness of agreement between independent measurements obtained by applying the experimental procedure under the same stipulated conditions. A measure of precision is the standard deviation [55].

#### 2.2 ISFET signal

Regardless of whether the ISFET's response is measured through changes in  $V_{np}$  or  $I_{ds}$ , it will depend on the change of surface potential  $\Delta \psi_0$  with ion

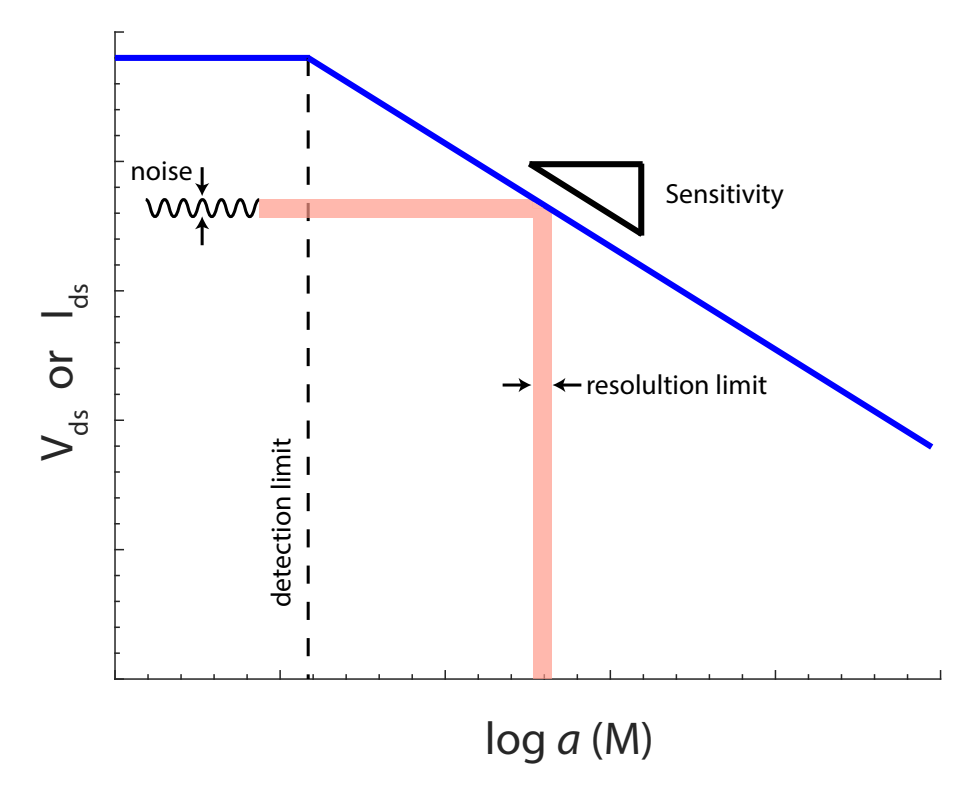


Fig. 2.1: Schematic showing an ISFET's sensitivity, detection limit and resolution.

concentration in the electrolytic solution.

#### 2.2.1 The site binding and Gouy-Chapman-Stern models

The relationship between the surface potential  $\psi_0$  and ion concentration is explained through Bergveld's theory [16], which accounts for the site binding [56] and the Gouy-Chapman-Stern models [13, 20]. For now, we will focus measuring hydrogen ions, but the same relationship holds true for other ions as well. Metal oxides are typically used as selective layers for measuring pH (hydrogen ions). The surface of any metal oxide contains hydroxyl groups M-OH, where M is the metal atom in the oxide. According to the site binding

model, these groups are amphoteric and may donate or accept a proton from the solution, leaving behind a charged surface group. The M-OH hydroxyl group accepts a proton, and becomes  $OH^{2+}$  in an acidic solution, while it donates a proton and becomes  $O^-$  in a basic solution as seen in Fig. 2.2. The surface charge density  $\sigma_0$  in the oxide is given by

$$\sigma_0 = -qN_s(\Theta^- - \Theta^+) \tag{2.3}$$

where q is the electron charge, and  $N_s$  is the number of surface hydroxyl sites per unit area.  $\Theta^-$  and  $\Theta^+$  are the negatively and positively charged fractions of  $N_s$  at equilibrium. Changes in  $\sigma_0$  due to infinitesimal changes in pH at the oxide surface, pH<sub>s</sub>, is the surface's intrinsic buffer capacity  $\beta_{int}$ :

$$\frac{\delta \sigma_0}{\delta p H_s} = -q \frac{\delta (\Theta^- - \Theta^+)}{\delta p H_s} = -q \beta_{int}$$
 (2.4)

On the electrolyte side, an equal but opposite charge  $\sigma_{dl}$  builds up due to charge neutrality. The distribution of charge in the electrolyte is explained by the Gouy-Chapman-Stern model, where two distinct layers appear, the Helmholtz and diffusive layer. The Helmholtz layer models the effect of the finite size of the ions and thus the centers of the ions cannot approach the surface any closer than the ionic radius  $x_H$ . The diffusive layer starts from  $x_H$  and extends to the bulk solution; the ionic distribution is influenced by ordering due to coulombic forces and disorder caused by random thermal motion.

The ability of the electrolyte to store charge in response to a change in

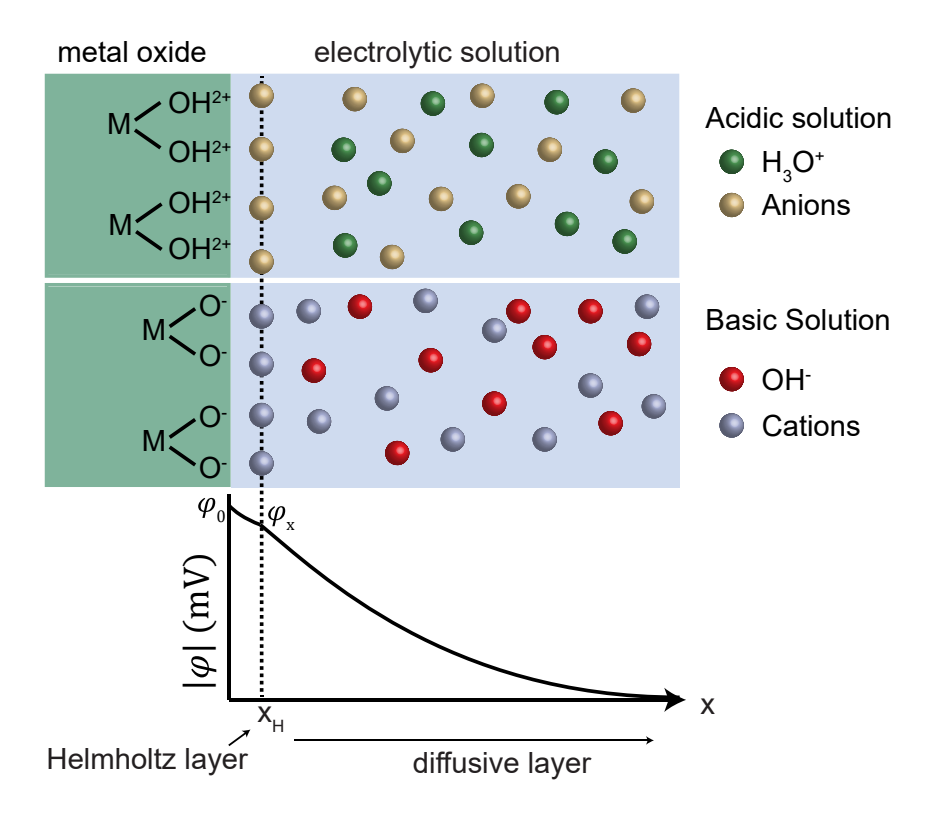


**Fig. 2.2**: The site binding and Gouy-Chapman-Stern models, where a metal oxide is in contact with an electrolytic solution. The M-OH hydroxyl group accepts a proton, or donates a proton in an acidic and basic solution respectively. An equal but opposite charge appears in the electrolytic solution through two distinct layers, the Helmholtz and diffusive layers.

electrostatic potential is the differential capacitance  $C_{diff}$ :

$$\frac{\delta \sigma_{dl}}{\delta \psi_0} = -\frac{\delta \sigma_0}{\delta \psi_0} = -C_{diff} \tag{2.5}$$

#### 2.2.2 The Nernstian Limit

Combining equations from both sides of the interface, eq. 2.4 and eq. 2.5 results in:

$$\frac{\delta \psi_0}{\delta p H_s} = \frac{\delta \psi_0}{\delta \sigma_0} \frac{\delta \sigma_0}{\delta p H_s} = \frac{-q \beta_{int}}{C_{diff}}$$
(2.6)

The hydrogen ion concentration at the surface  $pH_S$  is related to the hydrogen concentration at the bulk  $pH_B$  by a Boltzmann-Poisson equation

$$pH_S - pH_B = \frac{q\psi_0}{k_B T} \tag{2.7}$$

where  $k_B$  is Boltzmann's constant and T is the absolute temperature. Substituting eq. 2.7 into eq. 2.6 gives the Nernstian relationship between surface potential  $\psi_0$  and ion concentration in the bulk:

$$\frac{\delta \psi_0}{\delta p H_B} = -\ln 10 \frac{k_B T}{q} \alpha$$
where 
$$\alpha = \frac{1}{\ln 10 k_B T C_{diff} / q^2 \beta_{int} + 1}$$
(2.8)

The parameter  $\alpha$  is the ISFETs sensitivity factor and is a dimensionless parameter between 0 and 1. It depends on the intrinsic buffering capacity of the metal oxide  $\beta_{int}$  and the differential capacitance of the device  $C_{diff}$ . In the ideal scenario  $\alpha = 1$ , the sensitivity of an ISFET  $\delta \psi_0/\delta pH$  is thermodynamically limited to -59.2 mV/pH at 298 K, and is also known as the Nernstian

sensitivity. Sub-Nernstian sensitivities arise from less than ideal ISFETs, with sensitive layers that have relatively low intrinsic buffering capacity  $\beta_{int}$ .

Fig. 2.3 compares different metal oxides as sensitive layers for pH ISFETs [15]. From Fig. 2.3 (a),  $Ta_2O_5$ 's sensitivity approaches the Nernstian limit, and it can be inferred that it has very large  $\beta_{int}$ . In fact, it is so large that any variation in  $C_{diff}$  does not affect the ISFET's sensitivity, as seen in Fig. 2.3 (b), where increasing the NaCl concentration of solution, increases the differential capacitance of the ISFET.

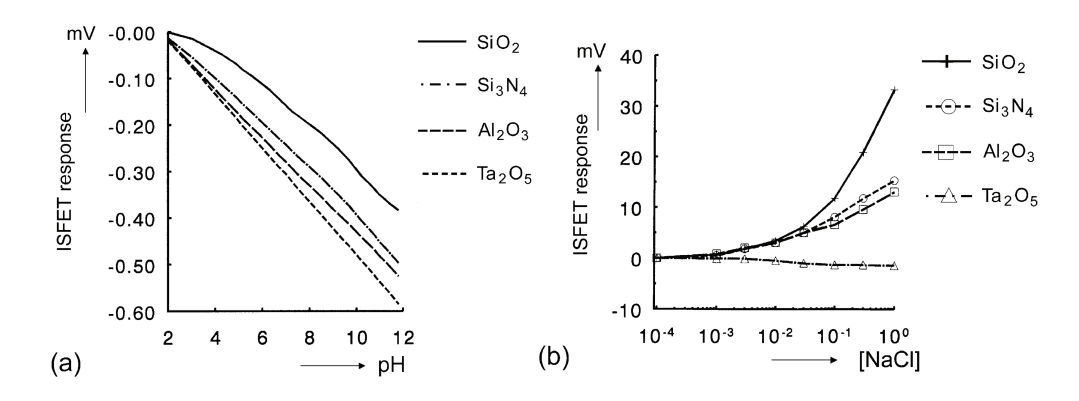


Fig. 2.3: (a) The response of ISFETs with different selective layers to changes in electrolyte pH. (b) The response of ISFETs with different selective layers to changes in NaCl concentration at constant pH 5.8. Reprinted with permission from Sensors and Actuators B: Chemical © 1993.

#### 2.3 The ISFET Noise

As with the signal of an ISFET, one can look at either the voltage noise  $v_n$  of the setup or the current noise  $i_n = v_n g_m$ . The voltage noise is related to the noise power spectral density N by:  $\langle v_n^2 \rangle = \int N df$ , where f is frequency.

There are many different sources of noise in an ISFET, and their typical values for contemporary ISFETs are shown in table 2.1.

#### **Brownian Noise**

The Brownian Noise  $v_{BN}$  arises from the thermal fluctuation of the ions in the electrolytic solution [57]. The voltage noise spectral density associated with the Brownian motion of the ions is [22]:

$$N_{BN} = 4k_B T Re(Z) \tag{2.9}$$

where Re(Z) is the real impedance of the electrolytic solution. This noise contribution is often small compared to other noise sources in ISFETs and is of the order  $0.1 \text{ pV}/\sqrt{\text{Hz}}$ . Note that Brownian motion of ions within the electrolyte induces Johnson-Nyquist noise due to the finite electrical resistance of the electrolyte, as expected from the fluctuation-dissipation theorem.

#### Johnson-Nyquist Noise

The Johnson-Nyquist noise  $v_{JN}$ , also known as white noise, arises from the thermal fluctuation of electrons in the resistive channel, and the voltage noise spectral density for this phenomenon is [58]:

$$N_{JN} = 4k_B T \gamma / g_m \tag{2.10}$$

where  $\gamma$  is the white noise parameter of the device.  $\gamma$  is usually 2/3 for long channel devices at the onset of saturation, and somewhat larger

for short-channel devices. In the triode regime, as is the case for our graphene ISFETs,

$$N_{JN} = 4k_B T R_{ds} (2.11)$$

where  $R_{ds} = 1/G_{ds} = \partial I_{ds}/\partial V_{ds}$ . For a typical ISFET, this noise contribution is also small and of the order 10pV-10 nV/ $\sqrt{\text{Hz}}$ .

#### Dipole Noise

Dipole noise  $v_{DP}$  arises from the thermally induced fluctuation of dipoles in the ISFET sensing layer and grows with reciprocal frequency 1/f. The associated noise spectral density

$$N_{DP} = 4k_B T \frac{\tan \delta}{2\pi f C_{dev}} \tag{2.12}$$

where  $\tan \delta$  is the loss tangent of the sensitive layer, which is a strong function of the material and method of deposition; it relies on empirical study. For a well designed ISFET, this is also typically small and of the order  $10~{\rm nV}/\sqrt{\rm Hz}$  at low frequencies of  $\sim 1~{\rm Hz}$ .

#### Charge Fluctuation Noise

Charge fluctuation  $v_{CF}$ , also known as flicker noise, arises from the charge trapping at the graphene/substrate and graphene/superstrate interfaces as well as the binding and un-binding of charge carriers at the sensitive layer/electrolyte interface. The noise spectral density due to charge fluctuation is [22]:

$$N_{CF} = \frac{q^2 N_0}{C_{dev}^2 WL} \cdot \frac{1}{f} \tag{2.13}$$

where  $N_0$  is the areal density of active sites in the sensitive layer contributing to charge fluctuation.  $N_0$  is dominated by the intrinsic buffer capacity  $\beta_{int}$  of the sensing layer, being typically  $\sim 10^{14}$  sites/cm<sup>2</sup> for Ta<sub>2</sub>O<sub>5</sub> [20]. WL is the channel area A, and although this scaling is known for Si FETs, it has not yet been tested in large graphene FETs.  $v_{CF}$  is by far the most dominating factor for the ISFET noise, and exceeds  $\mu V/\sqrt{\text{Hz}}$  range at the low frequency range < 100 Hz.

#### Read-out Noise

The intrinsic noise  $v_{IC}$  of the amplifiers and integrated circuits connected to the ISFET is small but can contribute to the overall noise of the setup and limit the resolution if the ISFET transconductance  $g_m$  is insufficient. The current noise  $i_{IC}$  is of the order 1pA/ $\sqrt{\rm Hz}$ , and depending on  $g_m$  the input referenced voltage noise could range between 1 nV - 1  $\mu$ V/ $\sqrt{\rm Hz}$ .

**Table 2.1**: Comparison of the different sources of voltage noise for typical ISFETs.

Noise Source	Voltage Noise $v_n$
$v_{BN}$	$0.6~\mathrm{pV}/\mathrm{\sqrt{Hz}}$
$v_{JN}$	$10 \text{ pV} - 10 \text{ nV}/\sqrt{\text{Hz}}$
$v_{DP}$	$10 \text{ nV}/\sqrt{\text{Hz}}$
$v_{CF}$	$> 30 \ \mu V / \sqrt{Hz}$
$v_{IC}$	$1 \text{ nV} - 1 \mu \text{V} / \sqrt{\text{Hz}}$

#### 2.4 The Signal to Noise Ratio

The signal-to-noise ratio is defined as the ratio of the power of the signal to the power of background noise, and can be expressed as

$$SNR = \frac{\langle v_s^2 \rangle}{\langle v_n^2 \rangle}$$

$$= \frac{\langle v_s^2 \rangle}{\langle v_{BN}^2 \rangle + \langle v_{JN}^2 \rangle + \langle v_{DP}^2 \rangle + \langle v_{CF}^2 \rangle + \langle v_{IC}^2 \rangle}$$
(2.14)

However, charge fluctuation and read-out electronic noise dominate the other sources of noise, as seen in table 2.1. Therefore, the SNR can be simplified to

$$SNR \approx \frac{(\Delta\psi_0)^2}{\langle v_{CF}^2 \rangle + \langle v_{IC}^2 \rangle} = \frac{(\Delta\psi_0)^2}{\frac{q^2 N_0}{C^2 A} \frac{\Delta f}{f} + \frac{\langle i_{IC}^2 \rangle}{g_m^2}}$$
(2.15)

from which it can be seen that maximizing FET transconductance  $g_m$  is essential to minimizing the effect of the readout noise  $\langle i_{IC}^2 \rangle$  and achieving noise performance intrinsic to the ISFET. Consequently, both the field effect mobility  $\mu$  and device capacitance  $C_{dev}$  must be maximized (eq. 2.1). In the limit of a large  $g_m$ , the SNR reaches the intrinsic ISFET limit,

$$SNR \approx \frac{C_{dev}^2 A}{e^2 N_0} \frac{f}{\Delta f} (\Delta \psi_0)^2$$
 (2.16)

which gives a clear prescription for optimizing SNR. The density  $N_0$  is expected to be dominated by the intrinsic buffer capacity  $\beta_{int}$  of the sensing layer, yet a large  $\beta_{int}$  is essential to achieving a Nernstian response with the ISFET signal being greatly compromised when  $\beta_{int} < 10^{14}$  sites/cm<sup>2</sup> [20, 59], thus setting a

lower bound for  $\beta_{int}$ .

Maximizing SNR can thus be achieved by maximizing both the device area A and the channel to analyte capacitance  $C_{dev}$  to minimize charge fluctuation noise. Coupled with the need for large  $g_m$  to reach intrinsic noise performance, graphene is an ideal material system to provide large-area devices with high charge-carrier mobility and high capacitive coupling to realize high resolution ion sensing.

The capacitance  $C_{dev}$  for a graphene ISFET is a series combination of the differential capacitance  $C_{diff}$ , the capacitance of the sensing layer  $C_{sl}$  and the quantum capacitance  $C_q = e^2 \delta n/\delta E_F$  arising from the density of states.  $C_{diff}$  is typically around 15-20  $\mu$ F/cm<sup>2</sup> [20]. The sensing layer capacitance is a function of the dielectric constant of the material  $\epsilon$ , its area A, and its thickness t, where  $C_{sl} = \epsilon A/t$ .  $C_{sl}$  can be maximized by minimizing the thickness of the sensing layer, such that the capacitance  $C_{dev}$  is limited by the quantum capacitance  $C_q$  of the channel, which is of the order  $\sim 1 \mu$ F/cm<sup>2</sup> [40]. The SNR of the ISFET with a large  $g_m$ , Nernstian response and quantum capacitance limited coupling becomes:

$$SNR = \left[ (\ln 10) k_B T \frac{\delta n}{\delta E_F} \Delta \psi_0 \right]^2 \frac{A}{N_0} \frac{f}{\Delta f}$$
 (2.17)

In conclusion, improving the ISFETs resolution can be achieved by operating the thermodynamic Nernstian limit while minimizing the noise associated with the setup. In the limit of a large  $g_m$ , the noise is dominated by the charge fluctuation at the sensitive layer/electrolyte interface. Therefore, it is important to maximize the sensor area, the carrier mobility and device capacitance

to the maximize the SNR, and hence the ISFET resolution. This signifies that graphene is an ideal material to realize the potential of potentiometric sensors. This analysis informs the design of graphene ISFETs in subsequent chapters of this thesis in terms of device area and thin-film design for capacitance and mobility.

## Chapter 3

# pH Sensing with Graphene ISFETs at the Nernstian Limit

Graphene ion sensitive field effect transistors (ISFETs) are an attractive candidate for high resolution sensing applications because of their high charge carrier mobility, the ideal coupling between graphene charge carriers and surface potential, and economical growth techniques for large area devices compared to traditional semiconductor methods. Previous work has shown that bare graphene ISFETs, which lack surface adsorption sites for proton or hydroxide binding, exhibit modest pH sensitivity [50, 51, 52]. However, graphene ISFETs with an Al<sub>2</sub>O<sub>3</sub> sensing layer have been demonstrated with a sensitivity up to 17 mV/pH, well below the Nernstian limit of 59.2 mV/pH at room temperature [54], due to difficulties with oxide growth on graphene [60, 61]. Sensing layers other than metal oxides for graphene ISFETs have been studied, such as phenol [53], and have also failed to achieve Nernstian sensitivities.

In this chapter, we report a series of pH sensing experiments with large-area graphene ISFETs using tantalum pentoxide ( $Ta_2O_5$ ) sensing layers of varying thickness. A pH sensitivity of 55 mV/pH, approaching saturation of the Nernstian limit, is observed for the first time with graphene ISFETs. The work presented in this chapter has been published in the following peer reviewed journal:

I. Fakih, S. Sabri, F. Mahvash, M. Nannini, M. Siaj and T. Szkopek, 'Large area graphene ion sensitive field effect transistors with tantalum pentoxide sensing layers for pH measurement at the Nernstian limit', Appl. Phys. Lett. 105, 083101 (2014).

#### 3.1 Graphene ISFET Fabrication

Graphene ISFETs were fabricated using graphene monolayers measuring  $1\times1~\rm cm^2$  grown on poly-crystalline copper foil catalyst (18  $\mu$ m) via chemical vapor deposition using custom built chambers [62]. Cu foils is preferred over other metals due to the low solubility of carbon atoms in copper, relatively large grain size and relative low cost. The Cu foils were chemically treated with acetic acid and acetone, and thermally annealed prior to graphene growth at 1000°C and low pressure. Poly(methyl methacrylate) (PMMA) was spin-coated onto the graphene/copper as a handle. The copper foil was etched with 0.1 M ammonium persulfate for around 6 hours. The low etchant concentration was chosen for better etch control and to preserve graphene integrity. After etching the copper, the graphene was transferred to de-ionized (DI) water for 15 minutes to remove any residual ammonium persulfate.

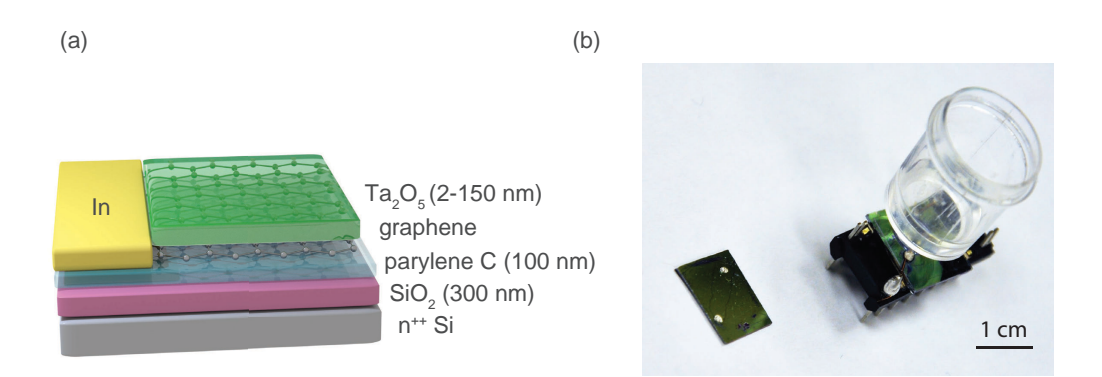


**Fig. 3.1**: (a) Cross-sectional schematic of graphene ISFET for measuring pH. (b) Optical image of a graphene ISFET. One of the devices has the plastic vessel glued atop and mounted on a chip carrier ready for measurement.

The graphene was then transferred to the target substrate and left overnight to dry. The substrates used are  $1\times1$  cm<sup>2</sup> n<sup>++</sup> doped silicon with 300 nm of dry thermal oxide and 100 nm of parylene C. The parylene C was deposited onto the SiO<sub>2</sub>/Si substrates at room temperature by evaporating a dimer at 650°C. The hydrophobic parylene surface improves graphene FET stability [63]. Importantly, the parylene substrate suppresses p-doping related to the O<sub>2</sub>/H<sub>2</sub>O redox couple [64]. Water trapped between the graphene and substrate supplies solvated O<sub>2</sub> to the graphene under the following redox reaction:

$$O_2(aq) + 4H^+ + 4e^-(graphene) \rightleftharpoons 2H_2O$$
 (3.1)

The Fermi level (redox potential) of the electrons associated with this reaction at equilibrium under atmospheric conditions is at  $\sim$  -5.3 eV relative to vacuum, according to the Nernst equation [64]. With the graphene Fermi level at around  $\sim$  4.6 eV [65], it is forced to shift into further down the valence

band resulting in p-doping.

Following the transfer of graphene to the substrate, indium contacts were mechanically applied to act as source and drain. The samples were heated at 175°C for a few seconds to melt the indium and ensure proper Ohmic contact with the graphene. A thin layer of Ta<sub>2</sub>O<sub>5</sub>, from 2 nm to 150 nm in thickness, was then grown by atomic layer deposition (ALD) with a Savannah S100 at the University of Toronto. Water vapor and pentakis(dimethylamino)tantalum(V) precursor were alternatively pulsed at a substrate temperature of 100°C. The relatively low deposition temperature was purposefully chosen to prevent any potential damage to the parylene or graphene. The oxide thickness was confirmed via reflectometery. A plastic vessel was glued atop the sample with a ultra-violet (UV) optical adhesive (Norland NOA 61) to contain 2 ml of electrolytic solution interacting with a 4 mm diameter section of graphene. The devices were then mounted on to a 16-pin chip carrier using conductive silver paint (SPI 05001-AB). An optical image of graphene ISFETs ready to be measured is shown in Fig. 3.1(b).

#### 3.2 Measurement Setup and Characterization

#### 3.2.1 Conductance Measurements

Graphene conductance  $G_{ds} = I_{ds}/V_{ds}$  versus electrolytic gate potential were conducted as illustrated Fig. 3.2(a). The drain-source current  $I_{ds}$  of the graphene ISFET was measured with a semiconductor parameter analyzer (Agilent 1500B) at a constant bias  $V_{ds} = 100$  mV versus an electrolyte potential  $V_{ref}$  applied directly through a Ag/AgCl reference electrode (RE, MF-2078,

BASi with 3M NaCl filling electrolyte). The Ag/AgCl electrode is vital for a stable electrolyte potential  $V_{ref}$ , which is reached through a redox system between the silver and chloride ions. The electrolyte potential  $V_{ref}$  was swept at a rate of up to 2 mV/s. The range of  $V_{ref}$  was controlled to  $\pm 0.8$  V to prevent the electrolysis of the buffer solution. The reference electrode current was monitored and found to be lower than 10 nA, at most 0.1% of measured  $I_{ds}$ . The silicon back gate was grounded, and the leakage current through it was also monitored and found to be at negligible levels of 100 pA or lower.

Six different buffered electrolytic solutions were examined for each graphene ISFET, including sodium citrate solutions at pH 3, 4, 5, and 6 as well as sodium phosphate solutions of pH 7 and 8. The buffered solutions were purchased from Sigma Aldrich. The graphene ISFET surfaces were rinsed with de-ionized water and dried between measurements.

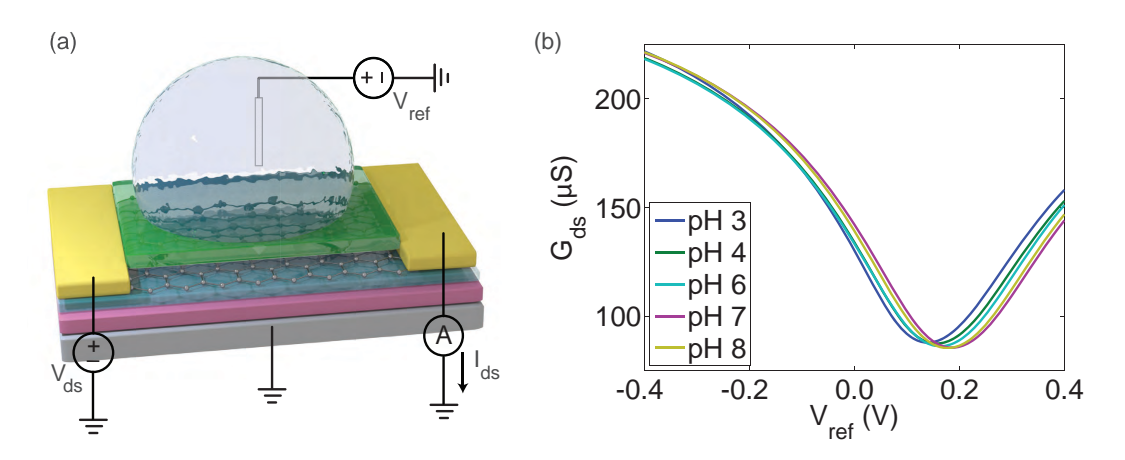


Fig. 3.2: (a) The electrical setup for measuring the graphene conductance  $G_{ds}$  for different pH solutions.  $I_{ds}$  was monitored at a constant bias  $V_{ds}$ , while the electrolytic potential was varied through  $V_{ref}$  and the back gate grounded. (b)  $G_{ds}$  of a 2 nm Ta<sub>2</sub>O<sub>5</sub> ISFET versus  $V_{ref}$  at  $V_{ds}$ =100 mV, for different pH solutions. Reprinted with permission AIP Publishing LLC © 2014.

A representative sequence of conductance  $G_{ds}$  versus  $V_{ref}$  measurements of a graphene ISFET with a 2 nm Ta<sub>2</sub>O<sub>5</sub> sensing layer is shown in Fig. 3.2(b) versus solution pH. At a given pH, the potential  $V_{np-g}$  of minimum conductance was determined by a parabolic fit and used to identify the net charge neutrality point. The applied potential  $V_{np-g}$  required to establish charge neutrality is a measure of the surface potential  $\psi_0$  developed across the oxide/electrolyte interface. There is a general trend of increasing  $V_{np-g}$  with increasing pH, corresponding to an increasingly negative net charge at the oxide/electrolyte interface with reduced proton concentration in the bulk electrolyte and a corresponding increase in hole doping of the graphene sheet.

#### 3.2.2 Capacitance Measurements

To measure the capacitance of the ISFET  $C_{dev}$ , a three electrode configuration was used with the graphene/Ta<sub>2</sub>O<sub>5</sub> acting as working electrode (WE), a platinum wire acting as counter electrode (CE), and a Ag/AgCl reference electrode (RE), as seen in Fig. 3.3(a). A lock-in amplifier (SRS, SR-830) was used to source an ac voltage  $V_{Pt}$  to the counter electrode at a frequency  $\omega/2\pi = 10$  Hz while measuring the counter electrode ac current  $I_{Pt}$ . A dc bias was applied via the counter electrode, while the electrolyte potential was monitored with the reference electrode. The capacitance is determined from  $C_{dev} = i_{ac}/\omega \text{Re}[v_{ac}]$ .

A representative sequence of capacitance  $C_{dev}$  versus  $V_{ref}$  measurements of the same graphene ISFET with a 2 nm Ta<sub>2</sub>O<sub>5</sub> sensing layer is shown in Fig. 3.3(b) versus solution pH. As seen in chapter 2, the capacitance  $C_{dev}$  is a

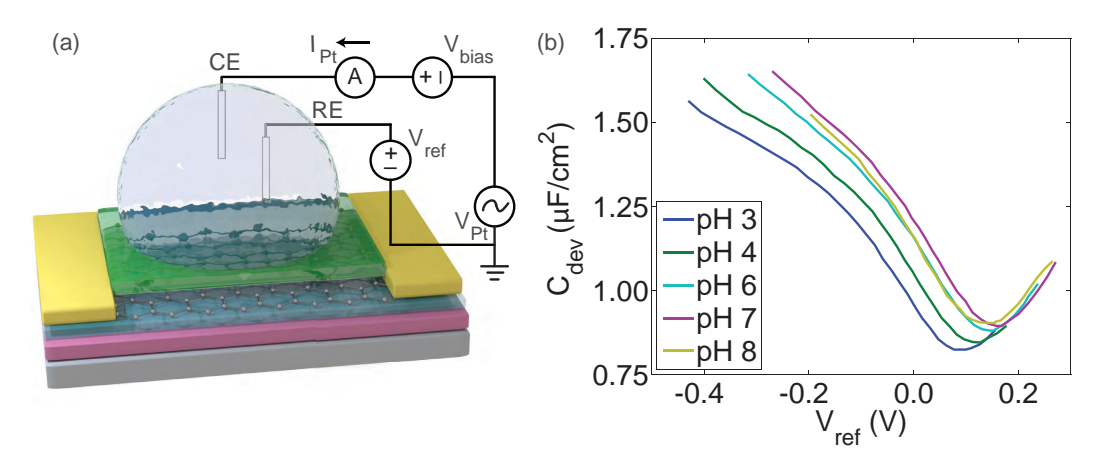


**Fig. 3.3**: (a) The electrical setup for measuring the graphene capacitance  $C_{dev}$  for different pH solutions. (b) The capacitance  $C_{dev}$  as a function of  $V_{ref}$  for the same 2 nm Ta<sub>2</sub>O<sub>5</sub> ISFET in Fig. 3.2. Reprinted with permission AIP Publishing LLC © 2014.

series combination of the differential capacitance  $C_{diff}$  of the Guoy-Chapman-Stern double layer, the capacitance  $C_{ox}$  of the metal oxide, and the quantum capacitance of graphene  $C_q = e^2 \delta n/\delta E_F$  arising from graphene's thermodynamic density of states. For our electrolytic solutions,  $C_{diff}$  ranges between 15 and  $20 \ \mu\text{F/cm}^2$  [20]. The 2 nm Ta<sub>2</sub>O<sub>5</sub> layer has a capacitance  $C_{ox} = 15 \ \mu\text{F/cm}^2$ . Graphene's quantum capacitance is comparatively small,  $C_q = 1 \ \mu\text{F/cm}^2$ , and exhibits a minimum at a potential  $V_{np-c}$  corresponding to graphene's charge neutrality point [40]. The total device capacitance  $C_{dev}$  approaches  $C_q$  with a 2 nm oxide sensing layer, in agreement with our measurements.

#### 3.3 The ISFETs' Sensitivities

The ISFET's sensitivity is extracted by measuring the change in potential of minimum capacitance  $V_{np-c}$  or minimum conductance  $V_{np-g}$  with respect to

changes in pH. A similar variation in both  $V_{np-c}$  and  $V_{np-g}$  was observed versus pH as shown in Fig. 3.4. From pH 3 to pH 7, sensitivities of  $\delta V_{np-c}/\delta$  pH =  $17.9 \pm 0.5 \text{mV/pH}$  and  $\delta V_{np-g}/\delta \text{pH}$  11  $\pm 3 \text{mV/pH}$  were determined by linear fit. An anomalous response deviating from the trend at acidic pH was observed at the basic pH 8. The quantitative discrepancy between capacitive and conductive response may arise due to the difference in electrode configuration, the 100 mV bias across the graphene during conductance measurements, and the electron-hole asymmetry that can impart a discrepancy between conductance minimum and neutrally point. For the remaining of the measurements, we focus on conductance measurements owing to the simplicity of the single electrode configuration and dc conductance measurement.

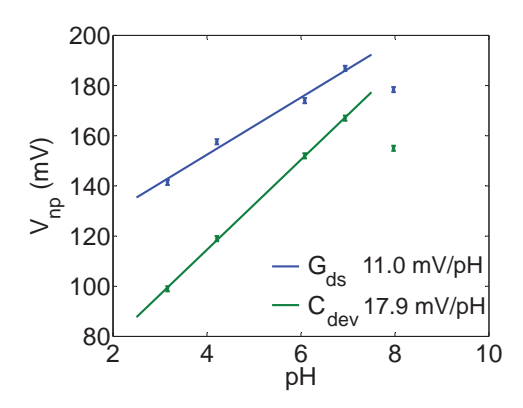


Fig. 3.4: The potential  $V_{np}$  of the minimum conductance and capacitance for the different pH solutions measured with a 2 nm Ta<sub>2</sub>O<sub>5</sub> ISFET. Reprinted with permission AIP Publishing LLC  $\bigcirc$  2014.

The pH response of a bare graphene ISFET and graphene ISFETs with 5 nm, 40 nm, and 150 nm thick layers of  $Ta_2O_5$  were also measured. The conductance of the ISFET with a 150 nm thick  $Ta_2O_5$  is shown in Fig. 3.5(a).

The pH response in conductance minimum shift  $\delta V_{np-g}$  is plotted versus pH for all devices measured in Fig. 3.5(b). A negligible sensitivity of  $0.9 \pm 0.4 \text{ mV/pH}$  was observed for bare graphene, with improved sensitivity with increasing sensing layer thickness reaching  $55 \pm 2 \text{ mV/pH}$  with a 150 nm sensing layer. The near Nernstian response was a first for graphene ISFETs at the time. Furthermore, linear response is observed over the range pH 3 through pH 8 with 5 nm of Ta<sub>2</sub>O<sub>5</sub> and thicker.

The sensitivity factor  $\alpha$  for our graphene ISFETs can be calculated from Bergveld's model (eq. 1.1) by dividing the measured sensitivities with the Nernstian limit,

$$\alpha = (\delta V_{np-g}/\delta pH)/(\ln 10k_BT/q) \tag{3.2}$$

and are shown in Fig. 3.7(a) for the different sensing layer thickness. From eq. 2.8, the sensitivity factor depends on both the differential capacitance  $C_{diff}$  and the intrinsic buffer capacity of the sensing layer  $\beta_{int}$ . With a reasonable estimation of the differential capacitance  $C_{diff} = 18 \,\mu\text{F/cm}^2$  [20] and measured sensitivity factor, the intrinsic buffer capacity  $\beta_{int}$  can in turn be estimated. Fig. 3.7(b) shows the capacity versus sensing layer thickness for our graphene ISFETs.

The minimal sensitivity observed by the bare graphene ISFET has been previously observed by other groups [54]. This is explained by the relative paucity of sites for proton or hydroxyl binding, quantitatively corresponding to an observed buffer capacity of  $\beta_{int} \sim 10^{11}/\text{cm}^2$ . The increase in pH sensitivity with increased Ta<sub>2</sub>O<sub>5</sub> sensing layer thickness can be ascribed predominantly to an increasing buffer capacity. Notably, even with a 40 nm thick Ta<sub>2</sub>O<sub>5</sub>

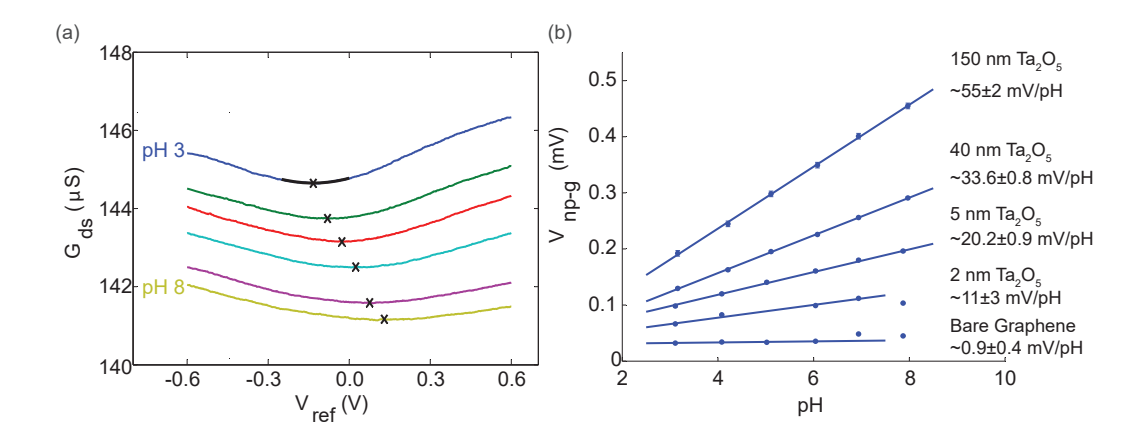
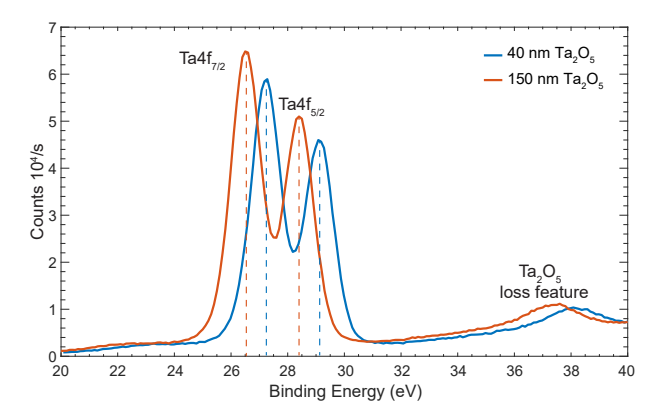


Fig. 3.5: (a)  $G_{ds}$  of a 150 nm Ta<sub>2</sub>O<sub>5</sub> ISFET versus  $V_{ref}$  at  $V_{ds}$ =100 mV, for different pH solutions. The minimum conductance obtained from parabolic fits are marked with a cross. Reprinted with permission AIP Publishing LLC © 2014.

sensing layer, the sensitivity factor is only  $\alpha$ =0.57 and the intrinsic buffer capacity is  $\beta_{int} = 9.7 \times 10^{12} \text{ sites/cm}^2$ . On the other hand, the 150 nm thick Ta<sub>2</sub>O<sub>5</sub> sensing layer resulted in a sensitivity factor  $\alpha$ =0.94 and intrinsic buffer capacity  $\beta_{int} = 1.1 \times 10^{14} \text{ sites/cm}^2$ .



**Fig. 3.6**: Binding energy peaks of tantalum for our 40 nm and 150 nm thick  $Ta_2O_5$  measured using x-ray photoelectron spectroscopy.

X-ray photoemission spectroscopy (XPS) with a Thermo Scientific Al K $\alpha$ source was performed on several graphene ISFETs. The surface of the ISFET with 40 nm of Ta<sub>2</sub>O<sub>5</sub> was found to contain 7% of silicon and 33% of carbon, indicating incomplete coverage by the ALD growth. Due to the lack of dangling bonds on the graphene surface, ALD of metal oxides on graphene can only grow on surface defects or edges [60]. Once the metal oxide nucleates on such defects or edges, the oxide begins to cover the rest of the surface. However, from the binding energy peak of tantalum shown in Fig. 3.6, 40 nm was not enough to ensure the formation of a stochiometric  $Ta_2O_5$ . A doublet of peaks (4f7/2 and 465/2) with binding energies of 27.3 and  $29.1 \pm 0.3$  eV were measured for the 40 nm oxide compared to the 26.56 eV and 28.32 eV reported for high-quality stochiometric  $Ta_2O_5$  [66, 67, 68, 69]. The carbon 1s line (at a binding energy of 284.8 eV) was used to calibrate the binding energy of the XPS measurements. The difference between the measured and reported values confirm that the oxide was some other form tantalum oxide. The higher binding energy peaks for the 40 nm thick  $Ta_2O_5$ , suggests a higher valency for tantalum than 5; however, this is most likely an artifact due to surface charging.

For the 150 nm ISFET, the XPS showed no silicon, but there was 23% carbon on the surface. The carbon is likely originating from incomplete oxidation of the pentakis(dimethylamino)tantalum(V) precursor during ALD growth at the low temperature of 100°C chosen to preserve parylene and graphene quality. Despite the high carbon content, the measured tantalum 4f peaks of 26.5 and  $28.3 \pm 0.3$  eV matches very well with the reported values for Ta<sub>2</sub>O<sub>5</sub>. It can be concluded that the Ta<sub>2</sub>O<sub>5</sub> is stochiometric to yield the large buffer capacity,

and corresponding sensitivity factor, observed with our graphene ISFETs.

Despite achieving a near Nernstian response with the large area graphene ISFETs, both the device capacitance  $C_{dev}$  and field effect mobility  $\mu$  were severely compromised with the 150 nm thick oxide layer. The oxide capacitance  $C_{ox}$  for a 150 nm Ta<sub>2</sub>O<sub>5</sub> is 0.15  $\mu$ F/cm<sup>2</sup>, nearly 10 times smaller than the graphene quantum capacitance  $C_q$ , making it the most dominant component in the device capacitance  $C_{dev}$ . Furthermore, the lengthy ALD process damaged the graphene, with field effect mobilities  $\mu = 350 \text{ cm}^2/\text{Vs}$  calculated from both back and top gated measurements, where

$$\mu = \frac{1}{C_{dev}} \frac{L}{W} \frac{\delta G_{ds}}{\delta V_{qs}} \tag{3.3}$$

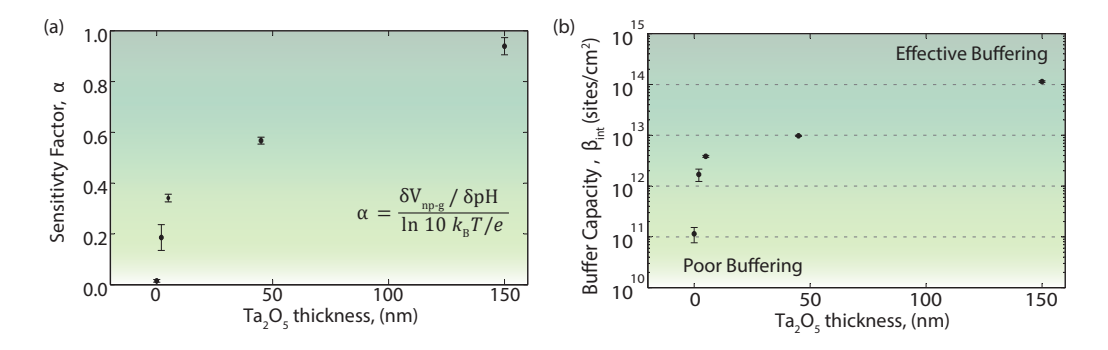


Fig. 3.7: (a) The sensitivity factor  $\alpha$  of the different ISFETs with respect to their Ta<sub>2</sub>O<sub>5</sub> thickness. (b) The intrinsic buffer capacity  $\beta_{int}$  of the same ISFETs with respect to their Ta<sub>2</sub>O<sub>5</sub> thickness. Reprinted with permission AIP Publishing LLC © 2014.

#### 3.4 The ISFET Stability

The stability of the graphene ISFETs response was tested over the course of approximately two weeks. The neutrality point  $V_{np-g}$  of a graphene ISFET with 5 nm Ta<sub>2</sub>O<sub>5</sub> layer thickness was monitored with a pH 7 electrolytic solution as gate. Evaporation of the solution was prevented by a simple seal, and the response monitored over a period of two weeks. The experimentally measured neutrality point  $V_{np-g}$  versus elapsed time in days is plotted in Fig. 3.8, with the corresponding pH scale as determined from the mean sensitivity of 20.2 mV/pH for 5 nm of Ta<sub>2</sub>O<sub>5</sub>. The measured neutrality point was stable at  $V_{np-g} = 206 \pm 1$  mV, or equivalent to  $\pm 0.05$  pH, over the two week observation window. The surface charge at the liquid/Ta<sub>2</sub>O<sub>5</sub> interface and the graphene/Ta<sub>2</sub>O<sub>5</sub> interface is thus stable.

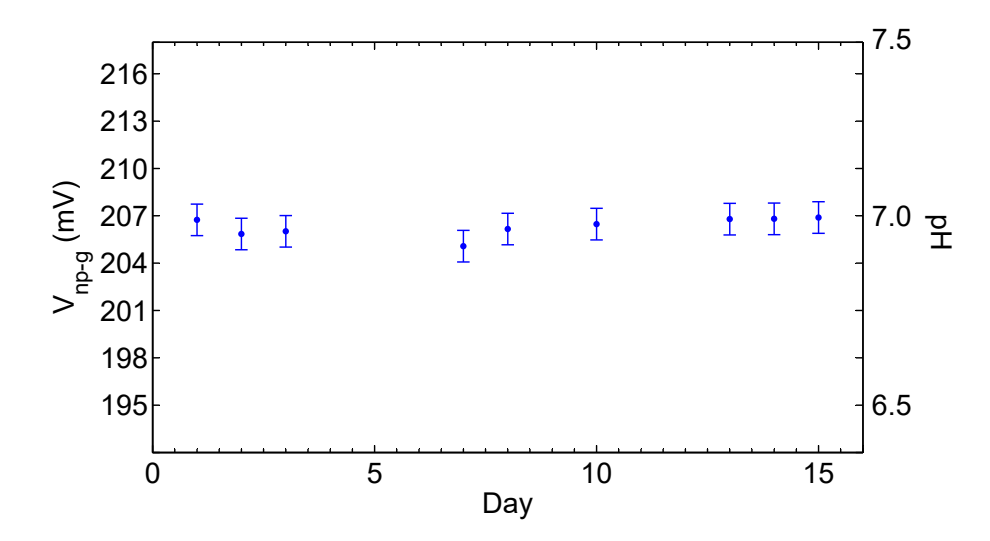


Fig. 3.8: The stability of a 5 nm  $Ta_2O_5$  ISFET with a pH 7 solution over the course of two weeks. The ISFET response was stable to  $\pm 1$  mV, or equivalently  $\pm 0.05$  pH. Reprinted with permission AIP Publishing LLC © 2014.

In conclusion, we have developed and demonstrated  $Ta_2O_5$ /graphene IS-FETs that approach the Nernstian limit of response  $\delta V_{np-g}/\delta pH = 59 \text{ mV/pH}$ . Bergveld's ISFET model allows us to determine that the increased sensitivity with increasingly thick  $Ta_2O_5$  sensing layers arises from an increase in buffer capacity. Difficulties with ALD of metal oxides on graphene due to its lack of dangling bonds leads to incomplete coverage at thinner layers. Only until 150 nm do we observe high quality stochiometric  $Ta_2O_5$  for achieving large buffering capacity and in turn higher sensitivities. However, the thicker metal oxides lead to lower  $C_{dev}$  and  $\mu$  which need to be maximized for better SNR. Development of improved processes for ALD growth of oxides on graphene will enable the use of thinner sensing layers, lowered fabrication cost, higher field effect mobility for better sensing resolution.

## Chapter 4

# pH Sensing with Graphene ISFETs at the Quantum Limit

High quality stochiometric metal oxides are necessary for large intrinsic buffering capacity and Nernstian limited response in ISFETs. However, as seen in the previous chapter, depositing such layers on graphene is quite difficult due to the lack of dangling bonds on the graphene surface. 150 nm of  $Ta_2O_5$  was required to ensure optimum oxide quality and complete surface coverage to achieve near-Nernstian limited sensitivities of 55 mV/pH. The thick oxide layer resulted in very small device capacitance (0.1  $\mu$ F/cm<sup>2</sup>) and also degraded the quality of the graphene with carrier mobilities  $\sim 350$  cm<sup>2</sup>/Vs, which both need to be maximized for improved sensor resolution. There have been attempts by other research groups to deposit thin high quality oxides on graphene by various techniques including functionalizing the graphene surface with perylene tetracarboxylic acid [60], water vapor pre-treatments [70], and

evaporating aluminum and oxidizing it [61, 71]; however, these attempts still degraded graphene's electrical properties, including an increase in device hysteresis. In this chapter, a new ALD approach is presented, where the graphene is encapsulated with an ultra-thin layer of parylene to protect the graphene from degradation, improve stability and promote nucleation of oxide growth during the ALD process. With only  $\sim 3$  nm of metal oxide required to ensure high-quality and complete coverage, we observe near-Nernstian limited sensitivities, carrier mobilities of  $\sim 7000$  cm<sup>2</sup>/Vs, gate capacitances approaching the quantum-capacitance limit  $\sim 0.6 \ \mu F/cm^2$ . Consequently, a record potentiometric pH resolution of 0.3 mpH is observed in a 60-Hz bandwidth. The work presented in this chapter has been published in a peer reviewed journal:

I. Fakih, F. Mahvash, M. Siaj and T. Szkopek, 'Sensitive precise pH measurement with large-area graphene field-effect transistors at the quantum-capacitance limit', Phys. Rev. Applied. 8, 044022 (2017).

#### 4.1 Graphene ISFET Fabrication

Graphene ISFETs were fabricated similar to those in section 3.1, and the structures are schematically illustrated in Fig. 4.1(a). Graphene monolayers grown on copper foils by CVD were transferred to target substrates. Two different 1 × 1 cm<sup>2</sup> substrates were explored for the ISFETs: n<sup>++</sup> doped silicon with 300 nm of dry thermal oxide and 100 nm of parylene C, and single crystal quartz with 100 nm of parylene C. The Si substrates were chosen for back gate characterization measurements, while the quartz was chosen to fully immerse the sensors in solutions without risk of developing a short circuit to

the electrolyte.

After transferring the graphene, indium was used as the source and drain contacts. A thin layer of parylene C, between 4 to 8 nm, was then deposited onto the graphene by evaporating a dimer (SCS 200 at the McGill micro and nanotools facility). The encapsulating hydrophobic parylene was deposited to protect the graphene during the ALD processing, improve stability, and promote nucleation of the oxide. The thickness of the parylene layers was measured by spectroscopic ellipsometry (GES-5E ellipsometer at the McGill micro and nanotools facility). The uniformity of the ultra-thin layer is measured with atomic force microscopy (AFM). The atomic-force-microscopy images in Figs. 4.2(a) and (b) for a 4 nm layer of parylene on a Si substrate shows around  $\sim$ 2 nm variation in thickness. The quality of the polymer is confirmed via XPS, where the measured characteristic Cl2p peaks matched those reported in the literature [72] at  $\sim$  200.4 eV and  $\sim$  202.0 eV (Fig. 4.2(c)), indicating that the chloride ion is bound to one of the carbons in the benzene ring.

For the sensing layers, thin layers of metal oxide (3-12 nm), either  $Ta_2O_5$  or  $Al_2O_3$ , were grown on the parylene by ALD at a substrate temperature of 175°C. While the mechanism behind ALD of stoichiometric metal oxides on polymers is an active area of research [73], AFM and XPS measurements confirmed complete surface coverage as well as the quality of both materials. The XPS measurements are seen in Fig. 4.2(c). Two peaks,  $Ta4f_{5/2}$  and  $Ta4f_{7/3}$ , were measured to be at ~26.6 and 28.4 eV, respectively, matching the reported average values found in the literature [74, 75]. The measured Al2p binding energy peak at 74.5 eV also matches that in the reported literature

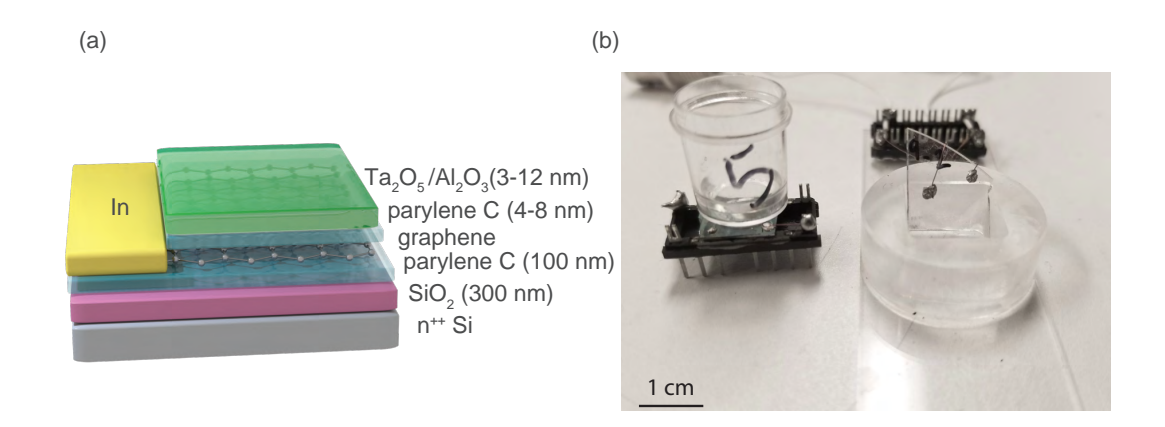


Fig. 4.1: (a) Cross-sectional schematic of graphene ISFET for measuring pH concentration. (b) Optical image of graphene ISFETs ready for measurement. The left is on a  $SiO_2/Si$  substrate, while the right one is on a quartz substrate.

[76].

A high angle annular dark-field image of a  $Ta_2O_5$  ISFET cross section was also taken with a scanning transmission electron microscope (TEM) (FEI Tecnai 12 BioTwin 120 kV TEM at the McGill Facility for Electron Microscopy Research) and shown in Fig. 4.3. The monolayer graphene cannot be distinguished within the parylene stack. The two layers of parylene appear as one, dark in colour due to the low-scattering cross-section of the low atomic number elements in parylene. The  $Ta_2O_5$  layer is bright and is 12 nm thick for this particular device.

To measure the perfromance of the ISFETs, those devices with a  $Si/SiO_2$  substrate had plastic vessels glued atop to contain 2 mL of electrolytic buffer solution interacting with a  $0.09 \text{ cm}^2$  section of graphene. The ISFETs on quartz were immersed directly in solution, as shown in Fig. 4.5.

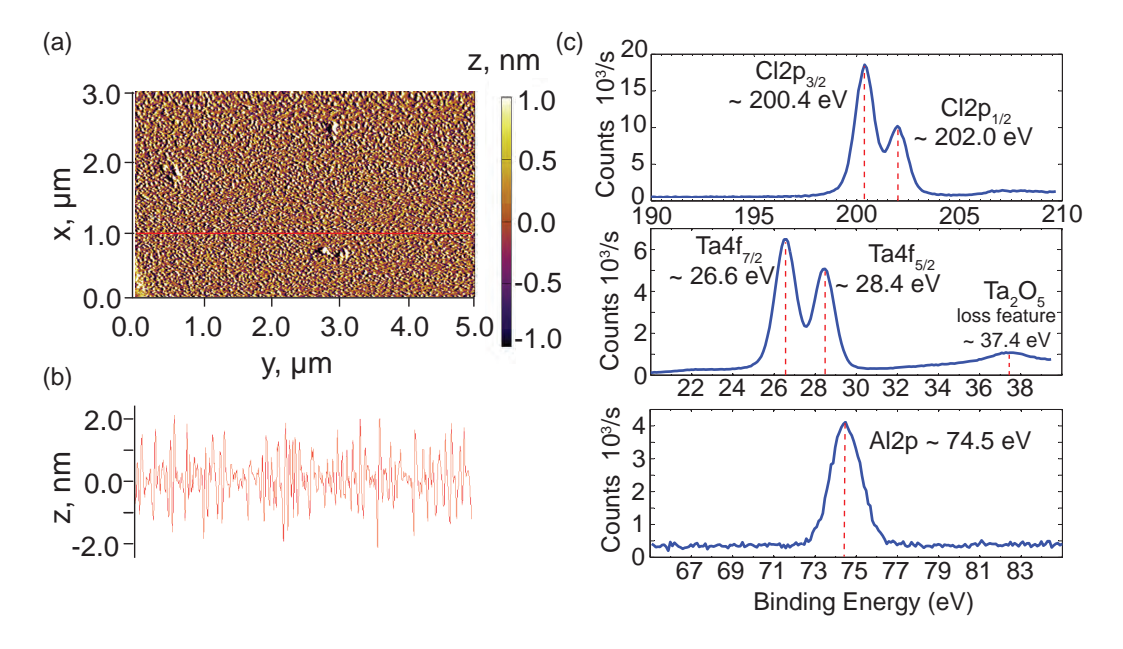
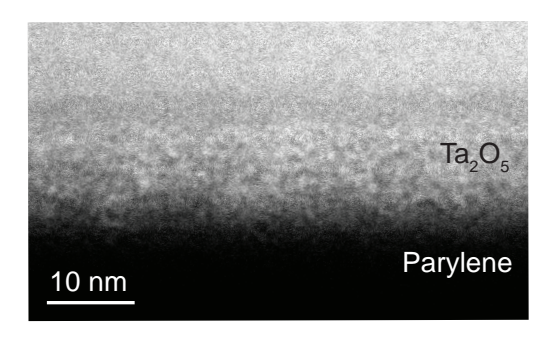


Fig. 4.2: (a),(b) Atomic force microscopy image of a 4 nm parylene C layer on a Si substrate with around  $\sim 2$  nm variation in uniformity. (c) Binding energy peaks of chlorine in parylene C, tantalum in  $Ta_2O_5$ , and aluminum in  $Al_2O_3$  grown on graphene and measured using x-ray photoelectron spectroscopy. Reprinted with permission American Physical Society © 2017.



**Fig. 4.3**: High-angle annular dark-field image of  $Ta_2O_5$  ISFET cross section. Reprinted with permission American Physical Society © 2017.

# 4.2 Capacitance measurements approaching the quantum limit

The ISFET gate capacitance between the analyte and graphene channel was measured using a three-electrode geometry as previously reported in section 3.2.2. A lock-in amplifier (SRS, SR-124) was used to source an ac voltage at a frequency  $\omega/2\pi = 13$  Hz superposed with a 0.1 V dc bias to a platinum counter electrode immersed in an electrolytic buffer solution while measuring the ac current flowing through one of the graphene contacts and monitoring the electrolyte potential  $V_{ref}$  with a Ag/AgCl reference electrode. Fig. 4.4 shows the measured capacitance of two different graphene-based ISFETs with a pH 4.37 sodium-phosphate buffer solution. One ISFET had 4 nm of parylene and 3 nm of  $Al_2O_3$  as a gate dielectric while the other ISFET had an 8 nm layer of parylene and 5 nm layer of Ta<sub>2</sub>O<sub>5</sub>. The characteristic dip in capacitance is a result of the quantum-capacitance minimum at charge neutrality. At a 0 V electrolytic gate bias  $V_{ref}$ , the measured capacitance  $C_{dev} \sim 0.6~\mu \text{F/cm}^2$  for the  $Al_2O_3$  ISFET and  $0.4 \mu F/cm^2$  for the  $Ta_2O_5$  ISFET, in good agreement with the calculated values using the measured thickness of the dielectric layers. Parylene's relatively low dielectric constant of  $\epsilon_r \approx 3.15$  leads to a significant difference between the two ISFETs, and while the thicker parylene layer for the  $Ta_2O_5$  ISFET reduces the total capacitance of the device, the graphene is better protected during the ALD process, and a larger modulation in capacitance is observed. These measurements show significant improvements in gate capacitances  $C_{dev}$  compared to the earlier ISFETs with 150 nm thick Ta<sub>2</sub>O<sub>5</sub> sensing layers in chapter 3.

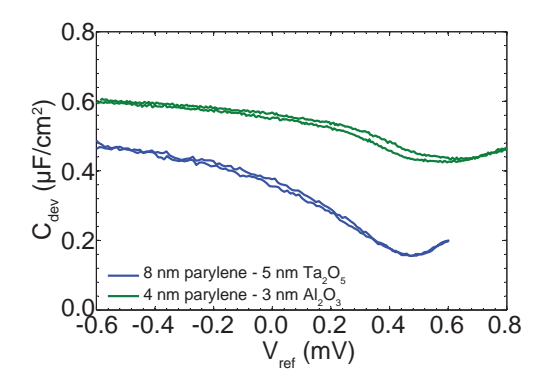


**Fig. 4.4**: Top-gate capacitance measurement of two different graphene IS-FETs. One ISFET had 4 nm of parylene and 3 nm of  $Al_2O_3$ , while the other had 8 nm of parylene and 5 nm of  $Ta_2O_5$ . Reprinted with permission American Physical Society © 2017.

#### 4.3 Conductance measurements approaching the

#### Nernstian limit

To study the ISFETs' sensitivities, the graphene conductance  $G_{ds} = I_{ds}/V_{ds}$  were measured versus electrolytic gate potential  $V_{ref}$  regulated through the Ag/AgCl reference electrode. The setup for the different substrates are shown in Fig. 4.5. The drain-source current  $I_{ds}$  of the graphene ISFET was measured with a semiconductor parameter analyzer (Agilent 1500B) at a constant bias  $V_{ds} = 100$  mV with a swept electrolyte potential  $V_{ref}$ . The range of  $V_{ref}$  was controlled to  $\pm$  0.8 V to prevent the electrolysis of the buffer solution and limit the current through the electrolytic gate to no more than 0.5% of the measured  $I_{ds}$ . Forward and backward sweeps of  $V_{ref}$  with a sweep rate of 2 mV/s were taken to study the stability and hysteresis of the ISFETs. All buffer solutions used in our experiments are 20 mM sodium-phosphate based purchased from Sigma Aldrich. A Thermofisher Orion 3 pH meter was used to verify the pH

of all test analytes before the experiments, and the devices are rinsed with 5  $M\Omega$  de-ionized water between measurements to avoid cross-contamination.

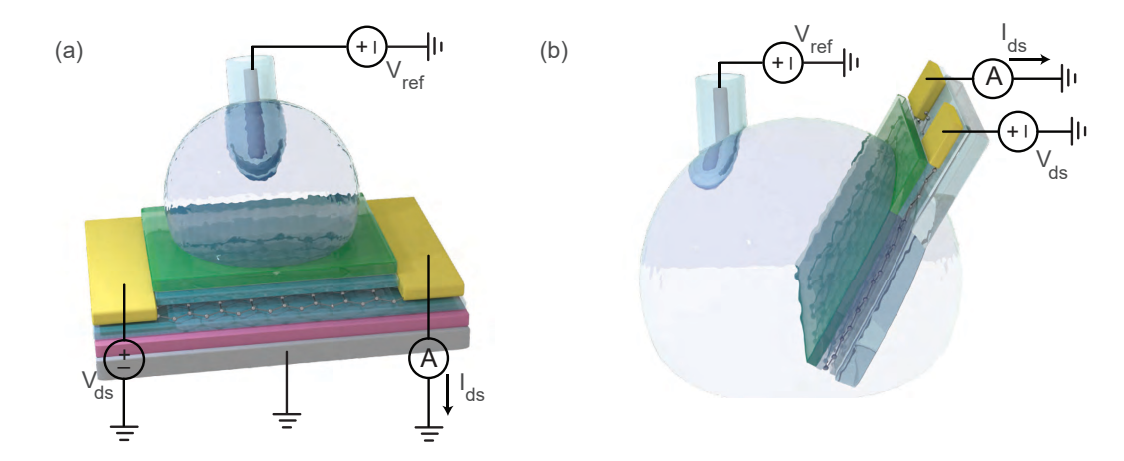


**Fig. 4.5**: (a), (b) The electrical setup for measuring the graphene conductance  $G_{ds}$  for different pH solutions for the two ISFET structures.

A representative sequence of measurements for graphene ISFETs, one with 5 nm of  $Ta_2O_5$  and another with 3 nm  $Al_2O_3$  sensing layers, for different pH buffer solutions are shown in Figs. 4.6(a) and (b), where the forward and backward sweeps are shown only for a pH = 3.22 buffer solution for clarity. It is important to note that the choice of substrate, whether quartz or  $Si/SiO_2$ , had no observable effect on the pH sensitivity of the ISFET.

At increasing analyte pH, an increase in the potential required to reach the point of net charge neutrality  $V_{np}$  is observed. A parabolic fit was used to find the potential  $V_{np}$  of minimum conductance at each pH, with the resulting dependence on pH plotted in Fig. 4.6(c). A line of best fit was used to calculate the overall sensitivity of our devices. The effects of hysteresis on  $V_{np}$  were accounted for in our uncertainty calculations. For the Al<sub>2</sub>O<sub>3</sub> graphene ISFETs, we observe a sensitivity of  $\sim 47 \pm 2$  mV/pH, near its empirical limit [15],

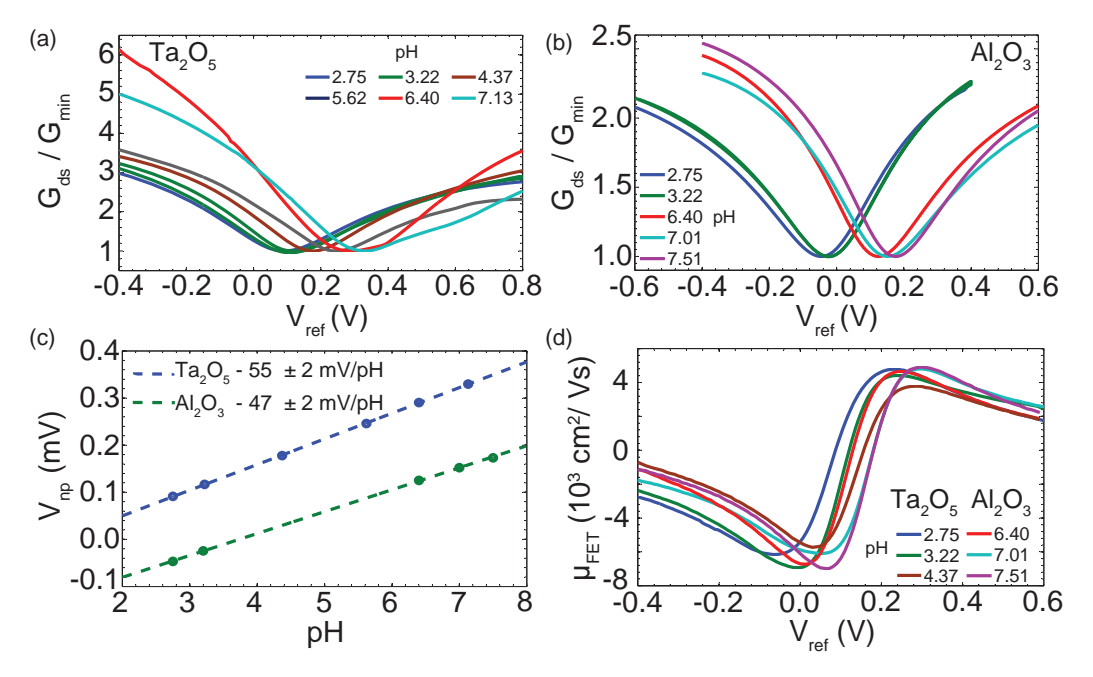


**Fig. 4.6**: (a), (b) The normalized conductance  $G_{ds}/G_{min}$  of 5 nm Ta<sub>2</sub>O<sub>5</sub> and a 3 nm Al<sub>2</sub>O<sub>3</sub> ISFET versus  $V_{ref}$ , for different pH solutions. Both forward and backward sweeps are shown for pH 3.22 to demonstrate the limited hysteresis of the ISFET. (c) The changes in  $V_{np}$  with different pH solutions are plotted for both Al<sub>2</sub>O<sub>3</sub> and Ta<sub>2</sub>O<sub>5</sub> ISFETs. (d) FET mobility of the 5 nm Ta<sub>2</sub>O<sub>5</sub> ISFET for pH solutions of 2.75, 3.22, and 4.37 as well as for a 3 nm Al<sub>2</sub>O<sub>3</sub> ISFET for pH solutions of 6.40, 7.01, and 7.51. Reprinted with permission American Physical Society © 2017.

and near-Nernstian sensitivity of  $\sim 55 \pm 2$  mV/pH for Ta<sub>2</sub>O<sub>5</sub> graphene IS-FETs. We also observe significant transconductance in our graphene ISFETs, with at least threefold modulation of  $G_{ds}$  for Ta<sub>2</sub>O<sub>5</sub> ISFETs and twofold modulation for Al<sub>2</sub>O<sub>3</sub> ISFETs. Importantly, the parylene encapsulation provides remarkable stability with little hysteresis as is evident in the forward and backward sweeps for pH = 3.22 for both the Ta<sub>2</sub>O<sub>5</sub> and Al<sub>2</sub>O<sub>3</sub> ISFETs shown in Figs. 4.6(a) and (b). From the capacitance and conductance measurements, we determine the field effect mobility  $\mu$  of our graphene ISFETs (eq. 3.3). Peak mobility as high as  $\sim 7000$  cm<sup>2</sup>/Vs, as shown in Fig. 4.6(d) was observed, indicating that the high electronic quality of the graphene was preserved during ISFET fabrication. Note that the FET mobility is signed, being positive for electron conduction and negative for hole conduction.

#### 4.4 ISFET resolution

In an effort to improve the SNR (eq. 2.16) and ISFET resolution, significant improvements in gate capacitance and transconductance compared to our earlier work were achieved while still operating at near-Nernstian pH sensitivities. Consequently, we set out to measure the real-time response of graphene ISFET current  $I_{ds}$  to pH changes, including the measurement of the root-mean-square current noise  $\sqrt{\langle i_n^2 \rangle}$ . A representative measurement for a 3 nm Al<sub>2</sub>O<sub>3</sub> ISFET on quartz, is shown in Fig. 4.7(a). The ISFET analyte was 1.2 mL pH 2.75 solution, and the current  $I_{ds}$  was monitored with a 60 Hz electrical bandwidth, while  $V_{ds}$  and  $V_{ref}$  were held constant at 100 and 0 mV, respectively. After 60 s of measurement, 35  $\mu$ L of pH 3.22 analyte was added,

corresponding to an 8 mpH change, and an instantaneous current change of  $i_s = \Delta I_{ds} = 85$  nA was observed. This is equivalent to a response of  $\delta i_s/\delta \rm pH$  = 10.6  $\mu \rm A/pH$ . Similar responses were observed in other graphene ISFETs.

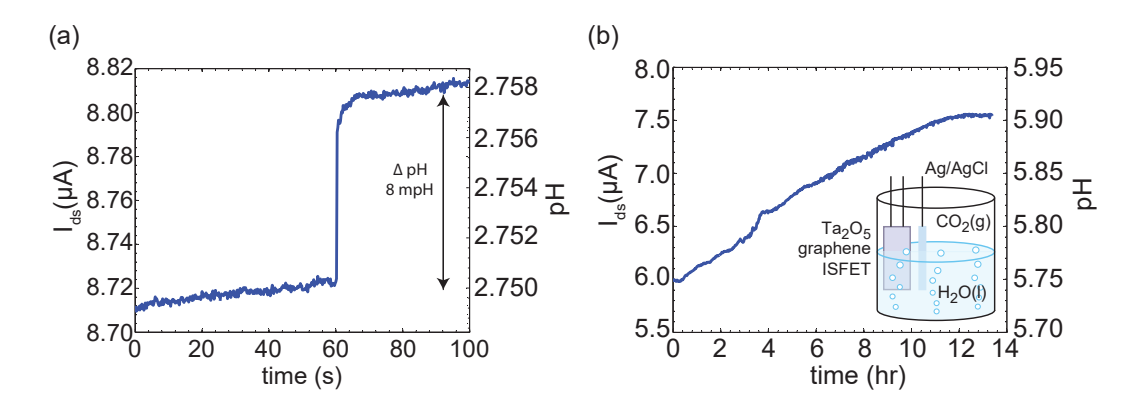


Fig. 4.7: (a) The change in current  $I_{ds}$  for a 3 nm Al<sub>2</sub>O<sub>3</sub> ISFET with time after adding 35  $\mu$ L of pH 3.22 to 1.2 mL of pH 2.75 at t = 60 s. (b) Monitoring the change in acidity of 1.2 mL carbonated water using a 5-nm Ta<sub>2</sub>O<sub>5</sub> ISFET by measuring the change in current  $I_{ds}$  with time. Reprinted with permission American Physical Society © 2017.

The root-mean-square (rms) noise current was determined from the measured current over a time interval of 60 s, giving  $\sqrt{\langle i_n^2 \rangle} \sim 1$  nA; the slope in current due to drift was subtracted when calculating the rms current. The minimum resolvable pH change (eq. 2.2) in these conditions is  $\delta \text{pH} = k\sqrt{\langle i_n^2 \rangle} /(\delta i_s/\delta \text{pH}) = 0.3$  mpH units, where  $k_c = 3$  for a confidence level of 90%. This is approximately one order of magnitude lower than the state-of-the-art potentiometric pH sensors [17]. This agrees and confirms our SNR model, where setting the SNR = 3 in eq. 2.17 (for a confidence level of 90%), and the device parameters of  $q^2\delta n/\delta E_f \sim 1$   $\mu \text{F/cm}^2$ ,  $N_0 \sim 10^{14}$  /cm<sup>2</sup>,  $A \sim 0.3 \times 0.3$  cm<sup>2</sup>, and  $\Delta f/f \sim 1$  leads to a minimum detectable  $\delta \text{pH} \sim 0.3$  mpH.

Last, we tested the ISFETs in measuring the evolution of pH in carbonated water in real time over a duration of 13 h. The analyte was 1.2 mL of potable carbonated water with pH = 5.75. A 5 nm Ta<sub>2</sub>O<sub>5</sub> ISFET was used, and the measured  $I_{ds}$  versus time is shown in Fig. 4.7(b) as carbon dioxide desorbed from the water. After approximately 11 h, the solution settled to a new pH. The current change  $\Delta I_{ds} = 1.60 \ \mu\text{A}$  over this interval corresponds to a final pH = 5.90, with a current sensitivity  $\delta s = \delta \text{pH} = 0.7 \ \mu\text{A/pH}$ .

In conclusion, we have improved the resolution of potentiometric pH sensors by encapsulating large-area graphene with ultrathin layers of parylene. The parylene imparts stability to the graphene, protects it from degradation, and acts as a seeding layer for the metal-oxide deposition. With only 3 nm of Al<sub>2</sub>O<sub>3</sub> or Ta<sub>2</sub>O<sub>5</sub> required to achieve near-Nernstian sensitivities, we have reduced the detection limit to 0.3 mpH units. This confirms our SNR model in chapter 2, and that increasing the area of an ISFET will decrease the noise significantly, and therein lies the advantage of large-area graphene. The approach outlined here could be applied to the problem of sensing the concentration of ionic species other than the proton, through the substitution of appropriately sensitive and selective layers.

## Chapter 5

# High Resolution K<sup>+</sup> Sensing with Graphene ISFETs

After demonstrating record potentiometric resolution for pH with graphene ISFETs by maximizing their area, carrier mobility and device capacitance in the previous chapter, the concept can be expanded upon to measure other ions by substituting the proton sensitive oxide layer with ionophore membranes. Ionophore membranes are typically used as selective layers in potentiometric ISEs [14, 77]. Ionophores are chemical species, naturally occurring or synthetic, that can reversibly bind to ions.

In this chapter, high resolution potassium ion sensitive parylene encapsulated graphene FETs are demonstrated. Using a potassium ionophore III membrane as a sensing layer, detection limits of  $K^+$  ion concentration down to  $10^{-9}$  M are observed. By encapsulating the large area graphene with parylene, we observe resolutions of  $2\times10^{-3}$  log  $[K^+]$ , 10 times better than state-of-the-

art potentiometric devices [78, 79, 80]. Furthermore, parylene encapsulation improves the long-term stability and reliability of the graphene ISFET, where their response was characterized over a five month period. We also performed selectivity and sensitivity tests in a variety of multi-solute specimens, including beverages and blood. The performance is more than sufficient for many real-time monitoring applications, including real-time water quality monitoring.

The work presented in this chapter has been published in a peer reviewed journal:

I. Fakih, A. Centeno, A. Zurutuza, B. Ghaddab, M. Siaj and T. Szkopek, 'High resolution potassium sensing with large-area graphene field-effect transistors', Sensors and Actuators B: Chemical. 291, 89-95 (2019).

#### 5.1 Graphene ISFET Fabrication

#### 5.1.1 Ionophore membrane preparation

To selectively detect potassium ions in liquid, potassium ionophore III (2-Dodecyl-2-methyl-1,3-propanediyl bis[N-[5'-nitro(benzo-15- crown-5)-4'-yl] carbamate]) was selected for use in the ion sensitive membranes. The structure of potassium ionophore III is shown in Fig. 5.1. There are a variety of known K<sup>+</sup> ionophores, including naturally occurring valinomycin which is commonly used in ISEs due to its superior sensitivity and selectivity [81]. However, valinomycin is classified as a hazardous substance [82], unlike potassium ionophore III.

To prepare the ionophore membrane, 22 mg of the ionophore was mixed

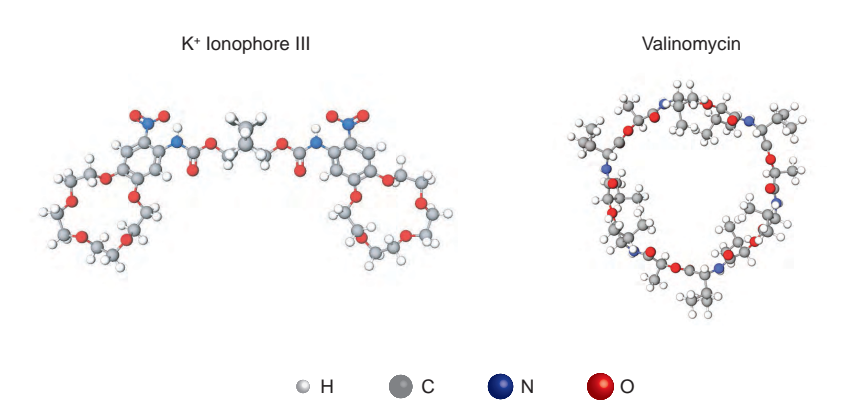


**Fig. 5.1**: 3D model of potassium ionophore III,  $C_{46}H_{70}N_4O_{18}$ , and of valinomycin,  $C_{54}H_{90}N_6O_{18}$ . Models were generating by *The Molview Project*.

with 10 mg of the lipophilic salt potassium tetrakis (4-cholorophenyl) borate (K-TCPB), 330 mg of poly(vinyl chloride) (PVC) and 660 mg of dioctyl sebacate (DOS) plasticizer. The ionophore, salt and PVC were in solid phase (powder), while the plasticizer was in liquid phase. The salt provides exchange sites, thus lowering the electrical resistance of the membrane, reducing anionic interference and consequently improving sensitivity [14]. The 1:2 ratio of PVC to plasticizer is a standard matrix for ionophore membranes [14, 83]. The mixture was dissolved in 4 mL of tetrahydrofuran (THF) and sonicated overnight. All chemicals were sourced from Sigma Aldrich.

#### 5.1.2 Device Preparation

Graphene ISFETs, schematically illustrated in Fig. 5.2(a), were fabricated with two different sources of graphene. In addition to the graphene monolayers grown on Cu foil via CVD in custom built chambers [62] (similar to previous chapters), they were also grown in a cold wall CVD Reactor (Aixtron BM) at

Graphenea to test the viability of mass production. The graphene was transferred from the Cu foils to target substrates using a poly(methyl methacry-late) (PMMA) handle and sacrificial etch of the Cu growth substrate. For the Graphenea samples, the etch and transfer were performed at their facilities by an automated process.

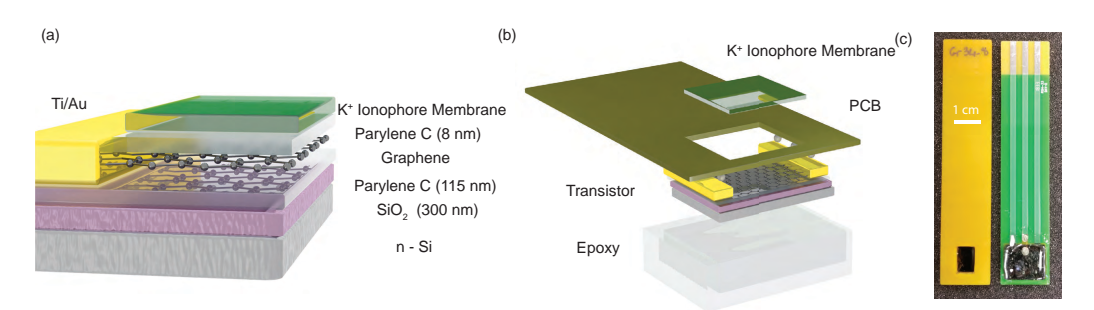


Fig. 5.2: (a) Cross-sectional schematic of graphene ISFET encapsulated with parylene and a layer of potassium ionophore membrane as a sensing layer on a Si/SiO<sub>2</sub> substrate. (b) Schematic of the sensing device. The graphene FET is mounted to a PCB with indium. The PCB has an opening for the gate area to be in contact with the liquid being measured. The K<sup>+</sup> ionophore mixture is dropcasted into the opening. Epoxy is used to encapsulate the back gate of the transistor. (c) An optical image showing the front and back of a typical graphene ISFET mounted on a PCB and ready for measurement. Reprinted with permission Elsevier © 2019.

The substrates were  $1.1\times1.3~\mathrm{cm^2}$  n-doped Si with 300 nm of dry thermal SiO<sub>2</sub> and 115 nm of parylene C. After transferring the graphene onto these substrates, Ti/Au (20 nm/80 nm) contacts were evaporated onto the graphene with the aid of a shadow mask to act as source and drain contacts. This was to provide better control and more consistency in the fabrication process compared to the previous method of applying indium contacts mechanically. From there, two different device types were prepared. In one set, the graphene FETs did not undergo further processing. In the second set, a thin layer of

parylene C,  $\sim 8$  nm, was deposited for the purpose of encapsulation. The work from chapter 4 has shown that parylene encapsulation can protect the graphene FET channel from degradation during the deposition of sensing layers, and that hysteresis can also be significantly reduced by parylene encapsulation. The parylene layer thickness is minimized so as to maximize the capacitance  $C_{dev}$  between graphene FET channel and the sensing layer.

Both sets of devices were then mounted on a printed circuit board (PCB) with In solder connecting the source and drain contacts (Fig. 5.2(b)). The PCB has a  $0.8\times0.5~\rm cm^2$  opening for the graphene FET area to be exposed to the analyte. We stress again the importance of the large area sensing area, which is orders of magnitude larger than commercial ISFETs, for reducing the charge-fluctuation noise and hence the ISFET noise current. The Si substrate was also connected to the PCB with silver paste to enable back-gate measurements. The ionophore membranes were formed on the graphene FETs by drop-casting  $50~\mu L$  of the K<sup>+</sup> ionophore membrane mixture onto the graphene through the PCB opening and left to dry overnight in ambient conditions. The resulting membrane is  $\sim 25~\mu m$  thick and creates a seal between the graphene surface and PCB. Two component epoxy (EpoTek-302) was applied and left to cure overnight to encapsulate the Si back gate and prevent electrical contact with the analyte. Fig. 5.2(c) shows an image of the front and back of a typical graphene ISFET mounted on a PCB and ready for measurement.

#### 5.1.3 Solution Preparation

KCl, NaCl, CaCl<sub>2</sub>, NH<sub>4</sub>Cl and MgSO<sub>4</sub> anhydrous salts with  $\geq$ 99% purity were used to prepare solutions for studying ISFET sensitivity and selectivity. The concentrations were carefully prepared and diluted with de-ionized water (> 10M $\Omega$ ), using both a micro-balance and micropipette. All devices, glassware and components were thoroughly rinsed with de-ionized water prior to and between measurements to minimize cross-contamination.

#### 5.2 Measurement setup and characterization

To confirm that the electronic quality of the graphene ISFETs after the fabrication process, back-gate transfer characteristics were first investigated. The drain-source current  $I_{ds}$  of the graphene ISFETs were measured with a semiconductor parameter analyzer (Agilent 1500B) versus the voltage applied to the Si substrate  $V_{Si}$  at a constant drains source bias voltage  $V_{ds} = 100 \text{ mV}$ . There was less variation between the Graphenea devices compared to those grown via our custom built chambers. The devices that were encapsulated with parylene were more stable, with negligible hysteresis, as compared to those without parylene encapsulation. Peak field effect mobilities of  $\sim 5000 \text{ cm}^2/\text{Vs}$  were observed.

#### 5.2.1 Capacitance Measurement

The ISFET gate capacitance  $C_{dev}$  between electrolytic analyte and graphene channel was measured using a three-electrode geometry as previously reported in section 3.2.2. Fig. 5.3 (a) shows the electrolytic gate capacitance  $C_{dev}$  for

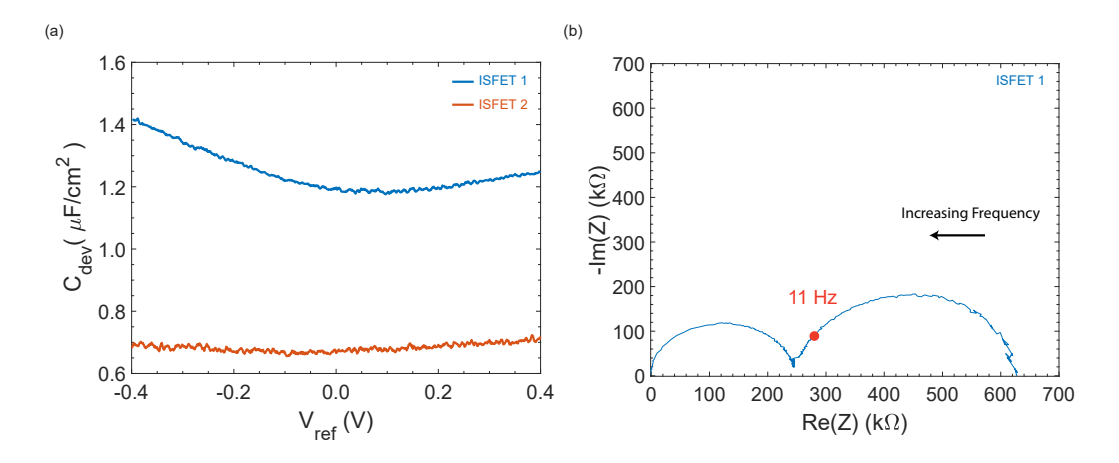
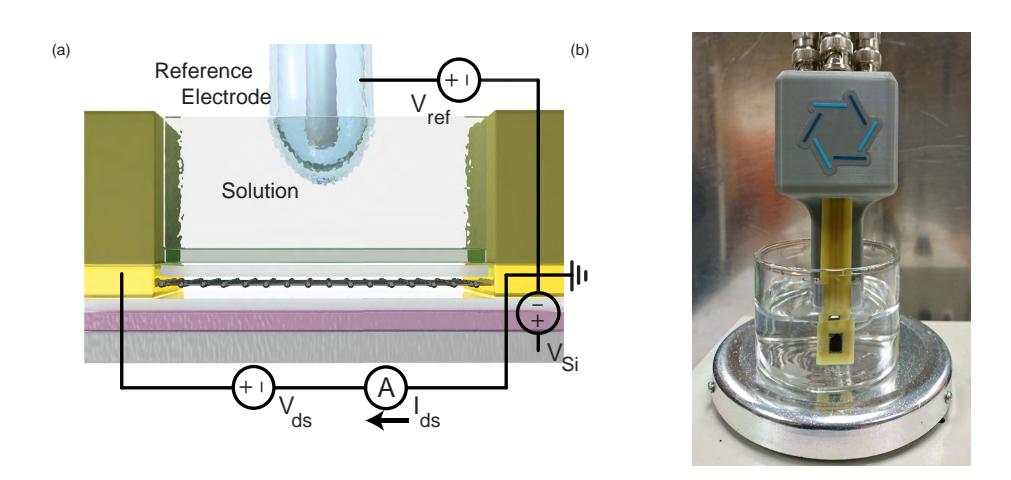


Fig. 5.3: (a) Top gate capacitance  $C_{dev}$  measurement of "ISFET 1" with respect to the reference electrode  $V_{ref}$  in a  $10^{-2}$  M K<sup>+</sup>. (b) Nyquist plot of "ISFET 1" in a  $10^{-2}$  M K<sup>+</sup> solution. Reprinted with permission Elsevier © 2019.

two representative ISFET devices immersed in a  $10^{-2}$  M K<sup>+</sup> solution, one for an ISFET without parylene encapsulation (ISFET 1) and one with parylene encapsulation (ISFET 2). For these measurements, a lock-in amplifier (SRS, SR-124) was used to source an ac current of  $i_{ac} = 1 \mu A$  through the platinum counter electrode at a frequency  $\omega/2\pi = 11$  Hz super-posed with a dc current, while measuring the ac voltage  $v_{ac}$  between the platinum electrode and the graphene source contact. The electrolyte potential  $V_{ref}$  was monitored with a Ag/AgCl reference electrode (RE, MF-2078, BASi with 3M NaCl filling electrolyte). A frequency of 11 Hz is a low enough frequency that the combination of the analyte resistance and reference electrode capacitance do not dominate the impedance, as confirmed by a Nyquist plot of impedance over a frequency range 0.2 Hz-20 kHz in Fig. 5.3(b). For "ISFET 1", the characteristic dip in  $C_{dev}$  versus potential is a signature of the quantum capacitance  $C_q$ , which follows the density of states of graphene and reaches a minimum at charge

neutrality. With  $C_{dev}$  approaching a minimum of  $\sim 1.2~\mu\text{F/cm}^2$  at the charge neutrality, it is indeed at the quantum limit set by the graphene, indicating that the  $\sim 25~\mu\text{m}$  PVC ion sensitive membrane is permeable to the electrolytic analyte solution. For "ISFET 2", the series addition of the 8 nm parylene layer (which has a capacitance of  $\sim 3~\mu\text{F/cm}^2$ ) decreases the overall capacitance to  $\sim 0.7~\mu\text{F/cm}^2$ , and suppresses the modulation in capacitance. However, it is important to note that the  $\sim 0.7~\mu\text{F/cm}^2$  is still an order of magnitude better than our initial ISFETs in chapter 3.

#### 5.2.2 Conductance Measurement



**Fig. 5.4**: (a) The electrical setup for measuring the graphene conductance  $G_{ds}$ . (b) An optical image showing an ISFET immersed in an electrolytic solution and being measured.

As with the previous chapters, the graphene ISFET response was studied by measuring the current  $I_{ds}$  versus electrolytic gate potential  $V_{ref}$  regulated through the Ag/AgCl reference electrode at a constant drain-source bias voltage  $V_{ds} = 100$  mV and  $V_{Si} = 0$  V. The range of  $V_{ref}$  was controlled to  $\pm 0.8$  V to prevent electrolysis of the analyte and to limit the current through the electrolytic gate to no more than 0.5% of the measured channel current  $I_{ds}$ . Forward and backward sweeps of  $V_{ref}$  were taken to study the stability and hysteresis of the ISFETs. Fig. 5.4(a) illustrates the electrical setup for the ISFETs, while Fig. 5.4(b) is an optical image of an ISFET immersed in an electrolytic solution and being measured.

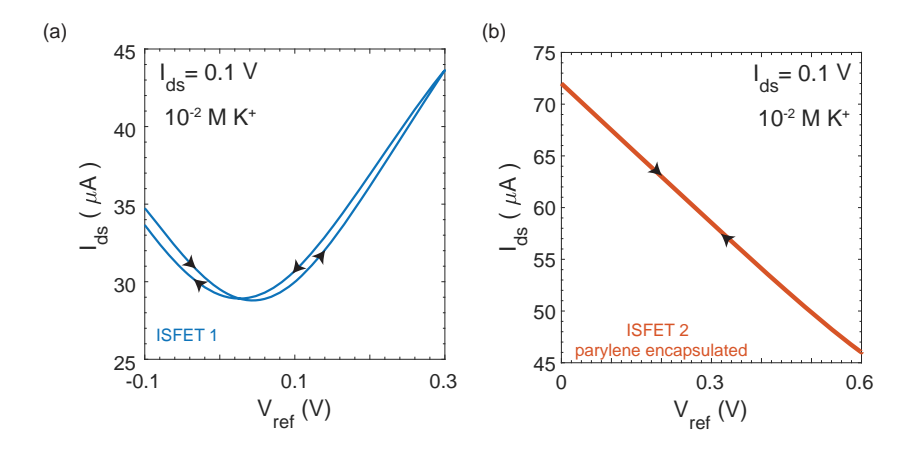


**Fig. 5.5**: (a)(b) The current  $I_{ds}$  of "ISFET 1" and "ISFET 2" with respect to reference electrode  $V_{ref}$  in a  $10^{-2}$  M. Reprinted with permission Elsevier  $\bigcirc$  2019.

A representative measurement of the same two graphene ISFETs, "ISFET 1" and "ISFET 2", immersed in  $10^{-2}$  M K<sup>+</sup> solutions are shown in Fig. 5.5(a) and (b) respectively. The electrolytic gate was not able to induce charge neutrality in "ISFET 2" nor in any of the parylene encapsulated graphene ISFETs. However, charge neutrality was reached with the Si back-gate in both parylene encapsulated and unencapsulated devices. The inability of the electrolytic gate to induce charge neutrality in the parylene encapsulated graphene ISFET is thus most likely due to a reaction between the THF in the ionophore

membrane and the parylene, degrading the dielectric properties of the parylene. This was confirmed in a separate test, where a parylene coated wafer lost its hydrophobicity when exposed to THF. Nevertheless, the parylene encapsulated graphene ISFETs demonstrated remarkable stability with no hysteresis compared to those that were not encapsulated.

#### 5.3 ISFET sensitivity

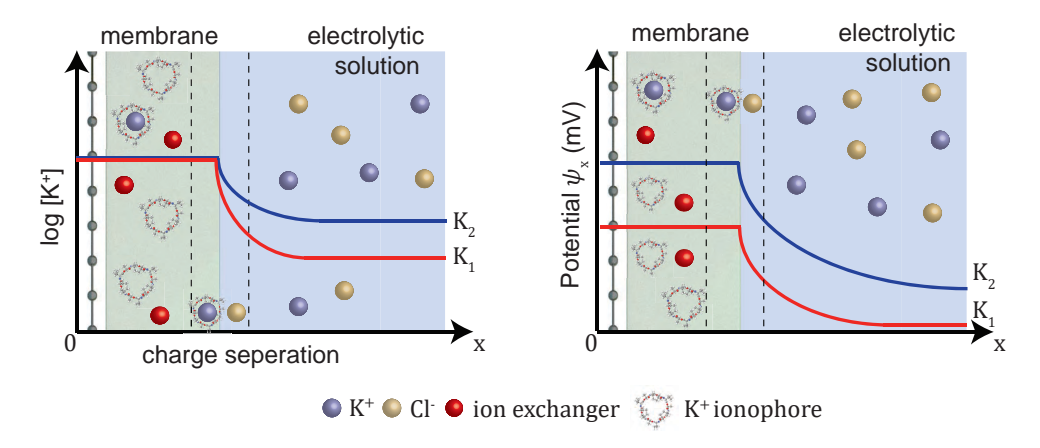


**Fig. 5.6**: (a) Schematic of change in K<sup>+</sup> concentration between the ionophore membrane and bulk solution for two different concentrations K1 and K2. (b) Schematic of change in potential between the ionophore membrane and bulk solution for two different concentrations K1 and K2.

The ISFETs' response were measured across a wide range of K<sup>+</sup> molar concentrations. Since the ionophore membranes are permeable, the potential across the sensitive layer is slightly different compared to the metal oxides used for measuring pH. Fig. 5.6 illustrates the mechanism for detecting changes in K<sup>+</sup> concentrations with graphene ISFETs in a potassium chloride solution. As the potassium concentration in the electrolytic solution changes from K1

to K2, the concentration in the membrane remains buffered to at a constant value [20, 77]. A few nm thick charge separation layer (diffusion layer) appears at the membrane/electrolyte interface. Since there is a concentration gradient between the bulk solution and the membrane, a potential difference appears at the solution. Due to the buffered membrane and presence of counter ion exchange sites, the potential across the membrane and thus that seen across the graphene is constant at  $\psi_0$ , and according to the Nernst equation, eq. 1.1:

$$\psi_0 = -\alpha \ln 10 \frac{k_B T}{zq} \frac{\log[K^+]_{membrane}}{\log[K^+]_{solution}}$$
(5.1)

As the potassium concentration changes from K1 to K2,  $\psi_0$  also changes, and a shift in the potential  $V_{np}$  required to reach charge neutrality is observed.

$$\Delta \psi_0 = \alpha \ln 10 \frac{k_B T}{q} (\Delta \log[K^+]) \tag{5.2}$$

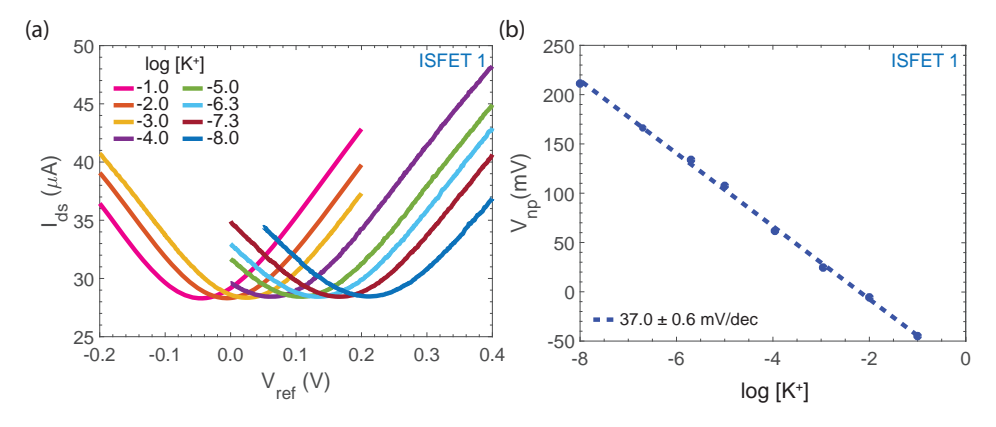


Fig. 5.7: (a) The channel current,  $I_{ds}$ , of ISFET 1 versus  $V_{ref}$ , for different K<sup>+</sup> molar concentrations.(b) The changes in  $V_{np}$  with different K<sup>+</sup> solutions are plotted for ISFET 1. Reprinted with permission Elsevier © 2019.

A representative sequence of measurements is shown in Fig. 5.7(a) for "IS-

FET 1". At increasing K<sup>+</sup> concentration, the transfer curve shifts uniformly, and we observe a decrease in the potential  $V_{np}$ . A parabolic fit was used to find the potential  $V_{np}$  of minimum conductance at every ion concentration, with the resulting dependence on K<sup>+</sup> concentration plotted in Fig. 5.7(b). A line of best fit was used to calculate the overall sensitivity of our devices. We observe a sensitivity of  $\sim 37$  mV/decade for "ISFET 1", which is lower than the Nernstian limit of  $\ln 10k_BT/q = 59$  mV/decade at room temperature observed for ISFETs with valinomycin ionophore membranes[84, 85]. The sub-Nernstian response can be attributed to the use of a less ideal ionophore as well as the ionophore to lipophilic salt ratio, which may require further optimization. Nevertheless, "ISFET 1" exhibits linear response down to  $10^{-8}$  M concentration, equivalent to 391 ng/L of K<sup>+</sup>.

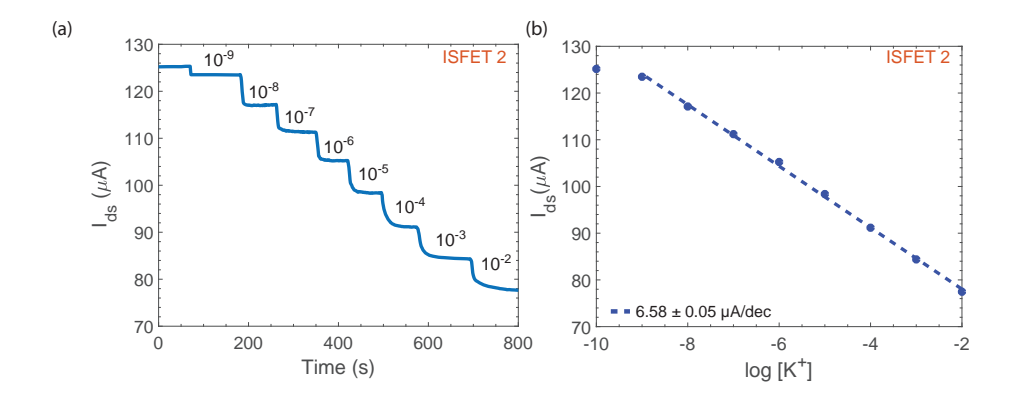


Fig. 5.8: (c) Continuous real-time measurement of  $I_{ds}$  for ISFET 2 when increasing K<sup>+</sup> molar concentrations by 1 decade step while keeping  $V_{ref} = 0$  V. (b) The linear response in  $I_{ds}$  with different K<sup>+</sup> solutions plotted for ISFET 2. Reprinted with permission Elsevier © 2019.

We also characterized the real-time response of graphene ISFETs to  $K^+$  concentration, measuring  $I_{ds}$  versus time with a constant  $V_{ref}$  and  $V_{ds}$  as the

 $\rm K^+$  concentration was varied. Starting with a  $10^{-10}~\rm M~K^+$  solution, the concentration tration was increased decade wise at uniform time intervals. A representative measurement is shown in Fig. 5.8(a) for "ISFET 2", with  $V_{ref} = 0$  V, where discrete changes in current are observed as the concentration is varied from  $10^{-10}$  M K<sup>+</sup> up to  $10^{-2}$  M K<sup>+</sup>. The response time of the graphene ISFET to changes in K<sup>+</sup> concentration is limited by the electrical bandwidth of the experiment. Fig. 5.8(b) is a plot of steady state  $I_{ds}$  versus the K<sup>+</sup> molar concentration, and a linear fit gives a response of 6.58  $\mu$ A/decade down to a record  $10^{-9}$  M K<sup>+</sup>. The latter is three orders of magnitude lower than that of commercial state-of-the-art potentiometric sensors [78, 79, 80]. Furthermore, with the parylene encapsulation, we observe a root mean square noise  $\sqrt{\langle i_n^2 \rangle}$ 5 nA in a 60 Hz electrical bandwidth, resulting in a minimal resolvable concentration of  $\sim 2 \times 10^{-3} \, \log[\mathrm{K}^+]$  with 90% confidence level. A comparison of the sensitivity and resolution for the K<sup>+</sup> ISFETs with and without parylene encapsulation is seen in table 5.1. The parylene encapsulation improves the resolution by two orders of magnitude.

**Table 5.1**: Performance comparison of different potassium sensitive graphene ISFETs with and without parylene encapsulation. Reprinted with permission Elsevier © 2019.

Device	Parylene Encapsulation	$\begin{array}{c} {\rm Sensitivity} \\ {\rm (mV/decade)} \end{array}$	$\begin{array}{c} \textbf{Sensitivity} \\ (\mu \textbf{A}/\textbf{decade}) \end{array}$	Sensing Resolution (log $[K^+]$ M)
Gr34-18 (ISFET 1)	No	37	1.93	$1.1 \times 10^{-1}$
Gr31-2	No	41	0.25	$3.2 \times 10^{-1}$
Gr31-6	No	41	0.44	$1.8 \times 10^{-1}$
Gr33-1	No	39	0.61	$1.6 \times 10^{-1}$
F16971 (ISFET 2)	Yes	-	6.58	$2.0 \times 10^{-3}$
F16991	Yes	-	4.45	$2.2 \times 10^{-3}$
Gr34-8	Yes	-	0.4	$2.2 \times 10^{-3}$

#### 5.4 ISFET Reliability and Reproducibility

The graphene ISFET reliability and reproduciblity were tested by alternating between two different K<sup>+</sup> concentrations. The  $I_{ds}$  for "ISFET 2" was monitored while alternating the K<sup>+</sup> concentration between  $10^{-2}$  M and  $0.5 \times 10^{-3}$  M, and a second experiment was performed with K<sup>+</sup> concentration alternating between  $10^{-4}$  M and  $9.75 \times 10^{-5}$  M as shown in Fig. 5.9(a) and (b) respectively. The bias voltages  $V_{ref}$  and  $V_{ds}$  were set at 0 and 0.1 V respectively. The ISFET channel current settles to the same values upon alternation of the concentration with minimal drift, exhibiting stability and reproduciblity.

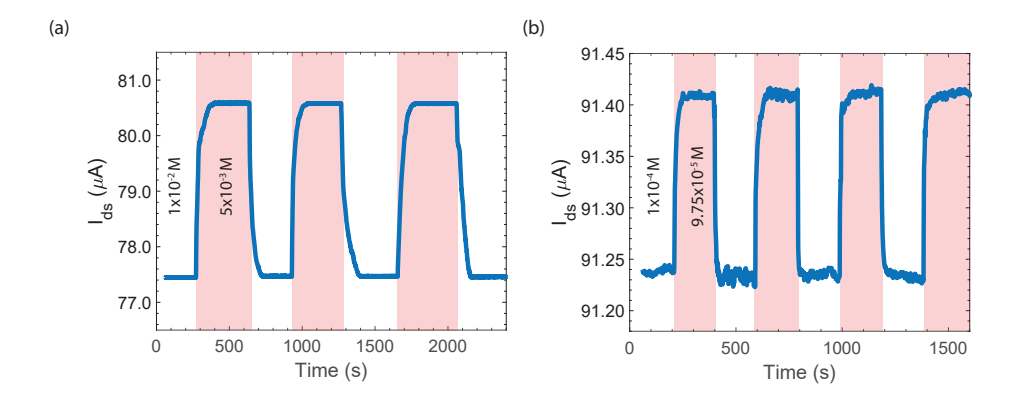
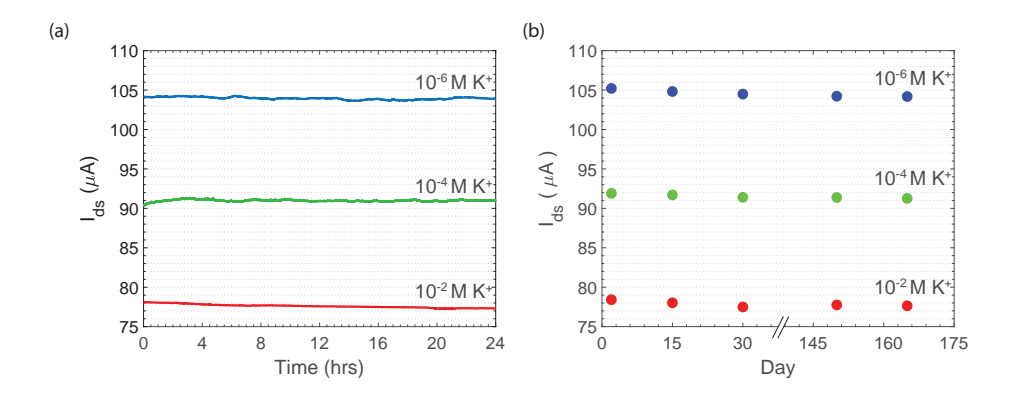


Fig. 5.9: (a) The ISFET current,  $I_{ds}$ , for "ISFET 2" while varying the K<sup>+</sup> concentration between  $10^{-2}$  M and  $0.5 \times 10^{-3}$  M. (b) The ISFET current,  $I_{ds}$ , for "ISFET 2" while varying the K<sup>+</sup> concentration between  $10^{-4}$  M and  $9.75 \times 10^{-5}$  M. Reprinted with permission Elsevier © 2019.

The same ISFET was also studied over time, by measuring the drift in  $I_{ds}$  over a 24 hour period for  $10^{-6}$ ,  $10^{-4}$  and  $10^{-2}$  M K<sup>+</sup> solutions under the same bias voltage conditions. A minor drift (25 nA/hr) is observed at irregular intervals throughout the measurement. The performance and stability of the ISFET was also looked at over a five month period, where the  $I_{ds}$  was

measured periodically for the same three K<sup>+</sup> concentrations,  $10^{-6}$ ,  $10^{-4}$  and  $10^{-2}$  M under the same bias conditions. Throughout this time, there was little change in the corresponding currents for each concentration ( $\pm$  0.5  $\mu$ A) and a linear current sensitivity is maintained which varied  $\pm$  0.2  $\mu$ A/decade from the original 6.58  $\mu$ A/decade measured when the device was fabricated, despite being stored in ambient conditions when not in use.



**Fig. 5.10**: (a) The ISFET current,  $I_{ds}$ , for "ISFET 2", over a 24 hour period for  $10^{-6}$ ,  $10^{-4}$  and  $10^{-2}$  M K<sup>+</sup> solutions, which exhibits minimum drift of  $\sim 25$  nA/hr. (b) The ISFET current,  $I_{ds}$ , measured periodically over five months for  $10^{-6}$ ,  $10^{-4}$  and  $10^{-2}$  M K<sup>+</sup> concentrations. Reprinted with permission Elsevier © 2019.

#### 5.4.1 ISFET Selectivity

ISFET selectivity against other ions is critical for sensing applications because other ions are inevitably present in analytes of interest. Ions other than the target  $K^+$  can bind to the ionophore, albeit with reduced efficacy [14]. This was tested for the ISFETs against Na<sup>+</sup>, Ca<sup>2+</sup>, Mg<sup>2+</sup>, and NH<sub>4</sub><sup>+</sup> which are either of similar size or charge to  $K^+$ , over the concentration range of  $10^{-6}$  M to  $10^{-2}$  M. As shown in Fig. 5.11, we observed minimal response in "ISFET 1"

for Na<sup>+</sup>, Ca<sup>2+</sup>, Mg<sup>2+</sup>, with 9 mV/decade for NH<sub>4</sub><sup>+</sup>. The cross-sensitivity is an intrinsic property of the ionophore used, as well as the ionophore to lipophilc salt ratio. Improved selectivity could be achieved with valinomycin. Moreover, the development of an ISFET array with preferential selectivity to a variety of ions can be used to more accurately infer ion concentrations.

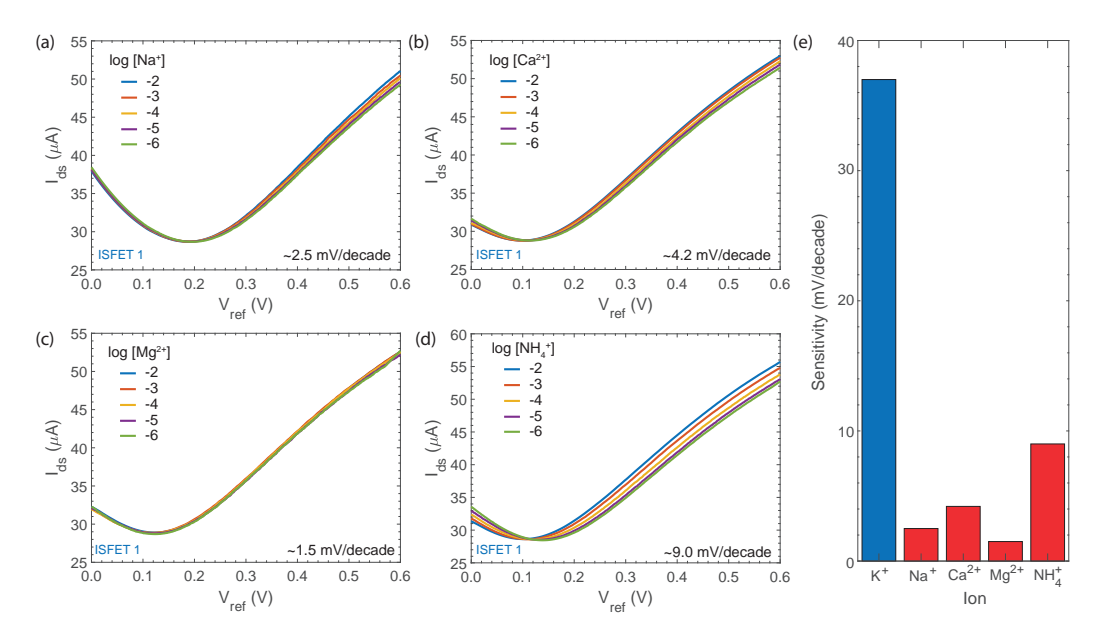


**Fig. 5.11**: (a-d) The cross-sensitivity of "ISFET 1" with Na<sup>+</sup>, Ca<sup>2+</sup>, Mg<sup>2+</sup>, and NH<sub>4</sub><sup>+</sup>. (e) A comparison of ISFET sensitivity with respect to its target ion K<sup>+</sup> and to interfering ions Na<sup>+</sup>, Ca<sup>2+</sup>, Mg<sup>2+</sup>, and NH<sub>4</sub><sup>+</sup>. Reprinted with permission Elsevier © 2019.

Lastly, we tested our ISFETs in a more practical scenario, measuring the K<sup>+</sup> concentration of liquids with multiple solutes, including common beverages and mammalian blood. The measured current and the inferred K<sup>+</sup> concentration were then compared to concentration measured with a commercial potassium ISE (HI4114); the values are shown in table 5.2 for "ISFET 2". The ISFET was first calibrated by measuring the current at 3 different K<sup>+</sup>

**Table 5.2**: Measured potassium content in different liquids with "ISFET 2" and comparing values to a commercial potassium ISE (HI4114). Reprinted with permission Elsevier © 2019.

Liquid	$\begin{array}{c} \textbf{ISFET-} \ \textbf{I}_{ds} \\ (\mu \textbf{A}  \pm  \textbf{0.005}   \mu \textbf{A}) \end{array}$	${ m ISFET}$ - ${ m [K^+]}$ ${ m (M} \pm 0.002 { m \ M})$	$egin{array}{c} { m HI4114 - [K^+]} \ { m (M \pm 0.01 \ M)} \end{array}$
$10^{-2} \; \mathrm{M} \; \mathrm{K}^{+}$	77.415	$1.00 \times 10^{-2}$	$1.00 \times 10^{-2}$
Milk, 2% Fat	73.658	$3.686 \times 10^{-2}$	$3.64 \times 10^{-2}$
Grape Juice	74.772	$2.547 \times 10^{-2}$	$2.32 \times 10^{-2}$
Lemon Juice	77.298	$1.041 \times 10^{-2}$	$1.03 \times 10^{-2}$
Orange Juice	73.113	$4.455 \times 10^{-2}$	$4.32 \times 10^{-2}$
Bovine Blood	76.152	$1.550 \times 10^{-2}$	$1.30 \times 10^{-2}$
Sheep Blood	77.572	$9.469 \times 10^{-3}$	$9.65 \times 10^{-2}$

concentrations,  $10^{-6}$ ,  $10^{-4}$  and  $10^{-2}$  M K<sup>+</sup> and a calibration curve extracted by using a line of best fit. The relation between current  $I_{ds}$  and concentration [K<sup>+</sup>] was:

$$\log([K^+]/[K_o^+]) = -(I_{ds} - I_{ds_o})/s$$
(5.3)

where  $[K_o^+]$  is the base reference concentration,  $I_{ds_o}$  is the ISFET drain current for the reference concentration, and s is the ISFET current sensitivity. For the experiments reported here,  $[K_o^+]$ ,  $I_{ds_o}$ , S were  $10^{-2}$  M, 77.415  $\mu$ A, and 6.63  $\mu$ A/decade respectively. From the results in table 5.2, it can concluded that the ISFET can be used with complex heterogeneous fluids.

#### 5.5 Conclusions

In conclusion, we have improved the performance of potentiometric potassium sensors over current state-of-the-art by using parylene encapsulated large5.5 Conclusions 77

area graphene ISFETs. They have the advantage of high charge carrier mobility, approach the quantum capacitance limit, and are easily fabricated as large-area devices, all of which are critical for improving the SNR. We observe a detection limit of  $10^{-9}$  M, equivalent to 39 ng/L, three orders better than state-of-the-art, and a precision of  $2 \times 10^{-3}$  log[K<sup>+</sup>]. Furthermore, we demonstrate remarkable selectivity, stability and reproduciblity of the sensors over a five month period. The approach outlined here could be applied to wafer scale processing for better reproduciblity between sensors, and expanded upon to the problem of sensing other ionic species, by incorporating ionophores selective to other ions. However, it is important to note that the reaction between the encapsulating parylene layer and THF causes uncontrolled doping of the graphene which negatively influences sensitivity and increases device to device variation. Engineering the layers deposited on the graphene has the potential to mitigate this problem.

### Chapter 6

## Multi Analyte Sensing with Graphene ISFETs

A major challenge for potentiometric ion sensors, whether ion selective electrodes or ion sensitive field effect transistors, is their poor selectivity compared to other ion measuring techniques. Ions other than the target ion, might also bind to the selective membrane, creating false positives and unreliable measurements in multiple analyte solutions. In this chapter, we overcome this challenge by expanding upon our previous work and fabricating an array of graphene ISFETs for detecting different ions. The ISFETs are calibrated against the different ions to extract the relationship between each ISFET and its interfering ions. Consequently, we can then account for the ion interference and reliably estimate multiple ion concentrations. We achieve detection limits down to at least  $10^{-5}$  M and resolutions of  $\sim 3 \times 10^{-3}$  log concentration. We also achieve an accuracy of  $\pm 0.01$  and  $\pm 0.05$  log concentration for the cations

and anions respectively. We also perform a real-time study in an aquarium with duckweed over three weeks, and measure the evolution of the ions in the water which act as nutrients for the plants. The performance is more than sufficient for many real-time applications, including real-time water quality monitoring [3].

The work presented in this chapter has been submitted for review in a peer reviewed journal:

I. Fakih, O. Durnan, F. Mahvash, I. Nepal, A. Centeno, A. Zurutuza, and T. Szkopek, 'Multi ion sensing with high resolution large area graphene field effect transistors', Under Review (2020).

#### 6.1 The Nikolskii-Eisenman Formulasim

The Nernst eq. concentration, eq. 1.1 can be written as

$$\psi_0 = \psi_0^0 + \alpha \log 10 \frac{k_B T}{zq} \log[a]$$
 (6.1)

where  $\psi_0^0$  is an initial surface potential and z and a are the charge number and activity, respectively, of the primary (target) ion. In most cases, except for high ion concentration approaching 1 M, the activity a is equal to the ion concentration. In the presence of multiple (interfering) ions, Nikolskii and Eisenman modified the Nernst equation to include the contribution to potential from multiple ionic species [86, 87]. We use the index i to identify quantities associated with the primary ion, and the index j to identify physical quantities associated with interfering ions. Thus,  $a_i$  is the activity of the primary ion,

 $a_j$  is the activity of an interfering ion, and  $z_i$  and  $z_j$  are the charge numbers of the primary and interfering ions, respectively. The potential  $\psi_{0i}$  developed at a membrane for target ion i in the Nikolskii-Eisenman theory is,

$$\psi_{0i} = \psi_{0i}^{0} + \alpha \log 10 \frac{k_B T}{z_i q} \log \left( a_i + \sum_{j \neq i} K_{i,j} a_j^{z_i/z_j} \right)$$
 (6.2)

where  $K_{ij}$  is the selectivity coefficient of the *i*-selective sensor towards interfering ion j. For a set of N ions, a suite of ISFETs targeting each ion  $1 \le i \le N$ can be characterized such that the selectivity coefficients  $K_{i,j}$  are known for all  $1 \leq i \leq N$  and  $1 \leq j \leq N$ , with  $K_{i,i} = 1$  by definition. A measurement of N potentials  $\psi_{0i}$  from N ISFETs will thus allow accurate determination of N ion concentrations  $a_i$ , assuming  $K_{i,j}$ ,  $\psi_{0i}^0$  and  $z_i$  have been determined. Importantly, the determination of the  $a_i$  from the measured  $\psi_{0i}$  requires the simultaneous solution of N nonlinear equations. Additionally, it is important to select the N ions carefully such that no ionic species which may cause non-negligible interference is excluded from measurement. There-in lies an advantage of graphene ISFETs, where it is more economical to fabricate multiple sensors than other potentiometric devices. To demonstrate this, we create a sensor array for measuring  $K^+$ ,  $Na^+$ ,  $NH_4^+$ ,  $NO_3^-$ ,  $SO_4^{2-}$ ,  $HPO_4^{2-}$  and  $Cl^-$  due to their prominence in agricultural runoff and their need to be measured for water quality monitoring [88, 89]. Water quality monitoring offers a great opportunity to demonstrate the suitability of graphene ISFETs for environmental monitoring.

#### **6.2** Device Preparation

To demonstrate the feasibility of fabricating multiple ISFETs, the graphene devices were fabricated via wafer scale processing, schematically illustrated in Fig. 6.1. A 100 mm diameter graphene monolayer was grown on polycrystalline Cu foil catalyst (18  $\mu$ m) via chemical vapor deposition in a cold wall CVD Reactor (Aixtron BM) at Graphenea. The graphene was wet-transferred via an automated process from the Cu foil to a target substrate wafer using a poly(methyl methacrylate) (PMMA) handle and sacrificial etch of the Cu growth substrate.

The target wafer was a 100 mm diameter, 500  $\mu$ m thick fused silica wafer (PRIME JGS2) with a 115 nm layer of parylene C. Without the need for back-gate measurements, silica wafers are a much cheaper alternative for mass production than oxidized silicon wafers. The parylene C was deposited at SCS coatings. After transferring the graphene onto these substrates, Ti/Au (20 nm/80 nm) contacts were evaporated onto the wafer as source and drain contacts with the aid of a shadow mask. The wafer was then diced into individual 1.1 cm× 1.1 cm devices, where they were then mounted on a printed circuit board (PCB) with two part silver epoxy (EpoTek-H20E) connecting the source and drain contacts (Fig. 6.1(b)). The PCBs have a  $0.8 \times 0.5$  cm<sup>2</sup> opening for the graphene FET to be exposed to the analyte.

The ionophore membranes were formed on the graphene FETs by dropcasting 50  $\mu$ L of a pre-prepared mixture onto the graphene through the PCB opening and left to dry overnight in ambient conditions. Two component epoxy (EpoTek-302) was applied and left to cure overnight to encapsulate the back of transistor and prevent electrical contact with the electrolytic solution. Figure 6.1(c) shows an image of the graphene ISFETs at different stages of the fabrication process.

It is important to note that while the previous chapters have showed that parylene encapsulation of the graphene protects the graphene, and ensures high resolution as well as long-term stability, the reaction between the THF in the ionophore mixtures with the parylene is still not fully understood. Since this chapter will be focusing on selectivity and not resolution or stability, it was decided to forgo parylene encapsulation for this set of devices.

#### 6.2.1 Ionophore Membrane Preparation

To selectively detect the different ions in liquid, we used ionophore mixtures for the following ions:  $K^+$ ,  $Na^+$ ,  $NH_4^+$ ,  $NO_3^-$ ,  $SO_4^{2-}$ ,  $HPO_4^{2-}$  and  $Cl^-$ . We prepared our own mixtures for  $K^+$ ,  $Na^+$ ,  $NH_4^+$ , and  $SO_4^{2-}$ , while we purchased ready made cocktails for  $Cl^-$ ,  $NO_3^-$  and  $HPO_4^{2-}$  from CleanGrow. Potassium ionophore III ( 2-Dodecyl-2-methyl-1,3-propanediyl bis[N-[5'-nitro(benzo-15-crown-5)-4'-yl] carbamate] ), ammonium ionophore I, sodium ionophore X (4-tert-Butylcalix[4]arene-tetraacetic acid tetraethyl ester), and sulfate ionophore I (1,3-[Bis(3-phenylthioureidomethyl)]benzene) were used for our own mixtures. The composition of the cocktails from CleanGrow are not known, as they are confidential.

To prepare the ionophore mixture, 20-25 mg of the ionophore was mixed with 10 mg of lipophilic salt, 330 mg of poly(vinyl chloride) (PVC) and 660 mg of dioctyl sebacate (DOS) plasticizer. The lipophylic salt was potassium

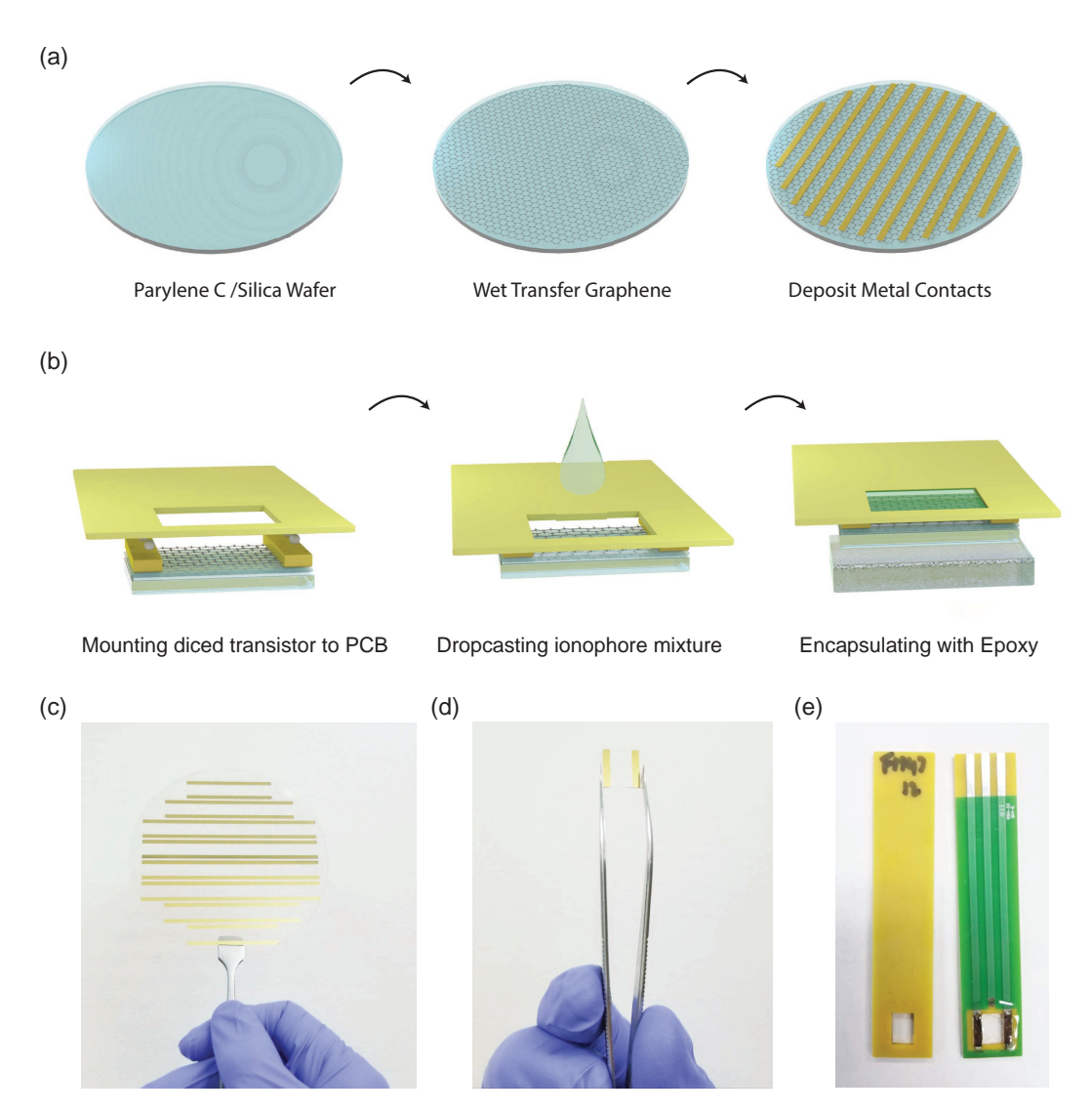


**Fig. 6.1**: (a), (b) Schematic of the fabrication process of the graphene ISFETs. (c) An optical image showing a the ISFETs at different stages of the fabrication process.

tetrakis (4-cholorophenyl) borate (K-TCPB) for cation sensors, and tridode-cylmethylammonium chloride (TDMAC) for the anion sensors. The mixtures were dissolved in 4 mL of tetrahydrofuran (THF) and sonicated overnight. All chemicals were sourced from Sigma Aldrich.

#### 6.3 ISFETs Response

#### 6.3.1 ISFET Sensitivities

To study the ISFETs' response to their respective target ions, they were individually immersed in electrolytic solutions of controlled concentration, as shown in Fig. 6.2. As in the previous chapter, two sets of measurements were conducted. In the first, the drain-source currents  $I_{ds}$  of the graphene ISFETs were measured with a semiconductor parameter analyzer (Keithley 1500B) versus electrolytic gate potential  $V_{ref}$  regulated through a Ag/AgCl reference electrode (RE, MF-2078, BASi with 3M NaCl filling electrolyte) at a constant drain-source bias voltage  $V_{ds} = 100$  mV for different ionic concentrations. The range of  $V_{ref}$  was controlled to  $\pm$  0.8 V to prevent electrolysis of the analyte and to limit the current through the electrolytic gate to no more than 0.5% of the measured channel current  $I_{ds}$ . In the second set of measurements, the drain-source currents  $I_{ds}$  were measured versus time at a constant  $V_{ref}$  and  $V_{ds}$ , while spiking the concentration at regular time intervals.

A representative set of measurements for a Na<sup>+</sup> ISFET is shown in Fig. 6.3 (a-b) when changing the concentration of NaCl from 10<sup>-6</sup> to 10<sup>-1.5</sup> M by half decade steps. The temperature and pH were closely monitored and were 23°C and 7.5 pH respectively. At increasing Na<sup>+</sup> concentration, the transfer curve

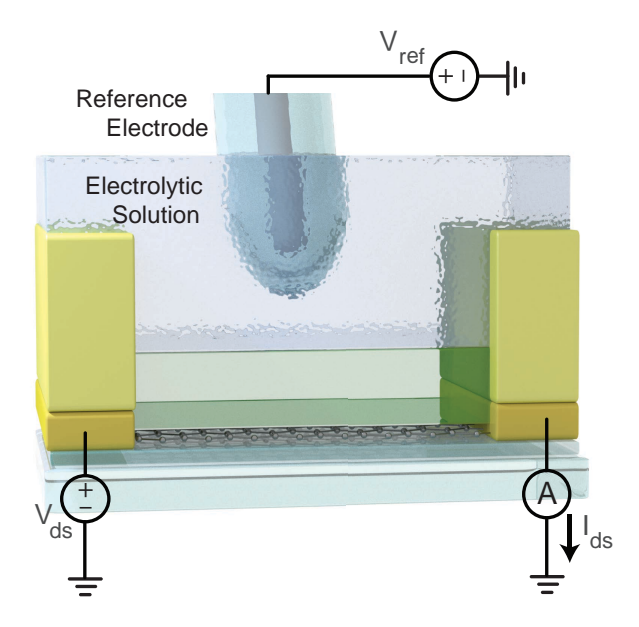


Fig. 6.2: Electrical setup for measuring the current through the graphene channel  $I_{ds}$  for different electrolytic solutions.

shifts uniformly, and we observe a decrease in the potential  $V_{np}$  required to reach charge neutrality. By measuring  $I_{ds}$  in real-time at a constant  $V_{ref}$  when changing the concentration, an instantaneous change in current is observed. The current values at different concentrations match those of Fig. 6.3(a) when  $V_{ref} = 0$  V. Similar measurements were performed for K<sup>+</sup>, NH<sub>4</sub><sup>+</sup>, NO<sub>3</sub><sup>-</sup>, SO<sub>4</sub><sup>2-</sup>, HPO<sub>4</sub><sup>2-</sup> and Cl<sup>-</sup> with their respective ISFETs.

From the transfer curve measurements (Fig. 6.3(a)), a parabolic fit was used to find the potential  $V_{np}$  of minimum conductance at every ion concentration, with the resulting dependence on ion concentration plotted in Fig. 6.4(a). A line of best fit was used to calculate the overall sensitivity of our devices. The sensitives between cations and anions differ in sign due to the charge of the target ion. Both NH<sub>4</sub><sup>+</sup> and NO<sub>3</sub><sup>-</sup>, approached the Nernstian limit of

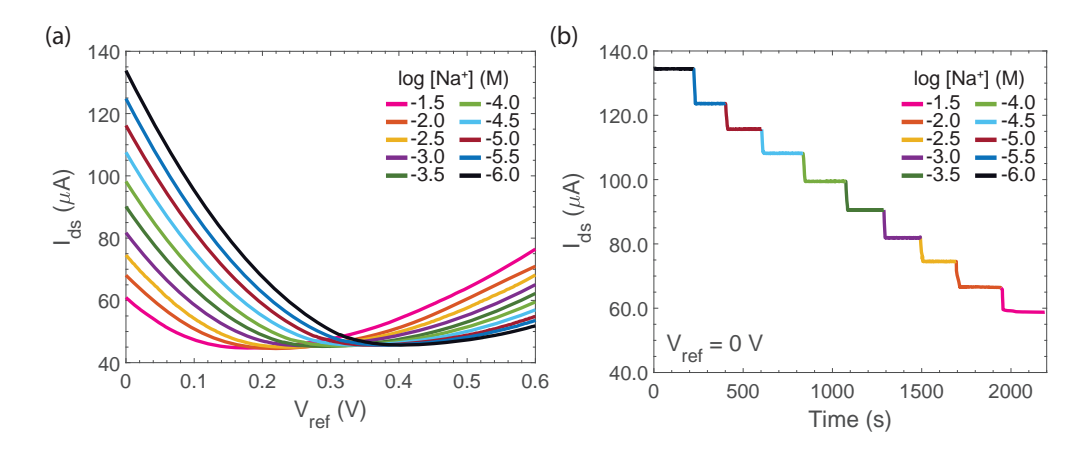


Fig. 6.3: (a) The channel current,  $I_{ds}$ , of an Na<sup>+</sup> ISFET versus  $V_{ref}$ , for different Na<sup>+</sup> molar concentrations. (b) Continuous real-time measurement of  $I_{ds}$  for the same Na<sup>+</sup> ISFET when increasing Na<sup>+</sup> molar concentrations by half decade steps while keeping  $V_{ref} = 0V$ .

58.8 mV/decade at 23°C with 58.6 and -56.7  $\pm 0.2$  mV/decade respectively, while for Na<sup>+</sup>, K<sup>+</sup> and Cl<sup>-</sup> they were slightly less at 49.2, 45.7 and -43.0  $\pm 0.2$  mV/decade. The sub-Nernstian response can be attributed to ionophore to lipophilic salt ratio [77], which may require further optimization. Both SO<sub>4</sub><sup>2-</sup> and HPO<sub>4</sub><sup>2-</sup> have a valency of 2, meaning their Nernstian limit is  $\sim 29.4$  mV/decade. However, the super-Nernstian response from the HPO<sub>4</sub><sup>2-</sup> is most likely due to the speciation of phosphate at different pH levels. At pH 7.5, 40% of the phosphate becomes H<sub>2</sub>PO<sub>4</sub><sup>-</sup>, which is valency 1 [90]. As a result, the ionophore membrane becomes sensitive to the two ions and a sensitivity higher than 29.4 mV/decade is observed. Nevertheless, all the sensors exhibit linear response down to at least  $10^{-5}$  M concentration, which exceeds the requirements water quality monitoring applications. It is import to note that in all the measurements, changing the counter-ion in the electrolytic solution had no observable effect on the measured sensitivities.

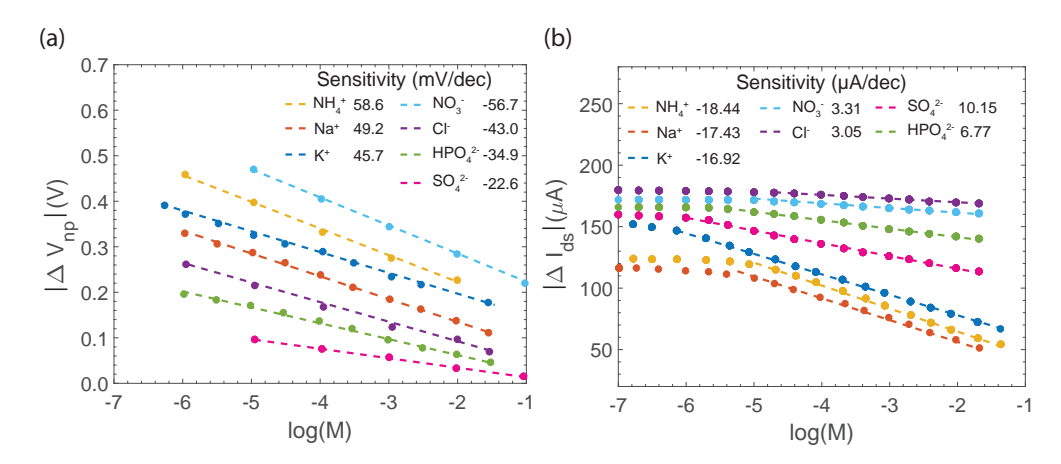


Fig. 6.4: (a) The changes in  $V_{np}$  for the different ISFETs with respect to concentrations of their respective target ions, with a linear fit to extract their voltage sensitivities. (b) The changes in  $I_{ds}$  for the different ISFETs with respect to concentrations of their respective target ions, with a linear fit to extract their current sensitivities.

Fig. 6.4(b) is a plot of the change in steady state  $I_{ds}$  of the different ISFETs versus the molar concentration of their respective target ions, extracted from Fig. 6.3(b) and other similar measurements. A linear fit gives us the current sensitivities of the ISFETs, which is a function of both the voltage sensitivity and the transistor transconductance. The relatively low current sensitivity for both the NO<sub>3</sub><sup>-</sup> and Cl<sup>-</sup> is most likely due to some damage to the graphene during the mounting to the PCB and hence lower transconductance. We also observe a similar linear response down to at least  $10^{-5}$  M concentration. A root mean square noise  $\sqrt{\langle i_n^2 \rangle} \sim 20$  nA in a 60 Hz electrical bandwidth is observed for the ISFETs, resulting in a minimum resolvable concentration of  $\sim 3 \times 10^{-3}$  log concentration for the cation ISFETs,  $\sim 3 \times 10^{-3}$  log concentration for the HPO<sub>4</sub><sup>2-</sup>, and  $\sim 2 \times 10^{-2}$  log concentration for both the NO<sub>3</sub><sup>-</sup> and Cl<sup>-</sup> ISFETs.

Encapsulating the graphene with parylene will most likely lower the resolution, as seen in chapter 5.

#### 6.4 ISFET Cross-Sensitivity

The ISFETs' response to interfering ions was studied by the separate solution method [91]. The ISFETs were placed in the same solution and the currents  $I_{ds}$  were measured concurrently in real-time while varying the ionic concentration. There was only one salt in the solution for each experiment. The currents  $I_{ds}$  were measured using a PalmSens4 potentiostat with one common reference electrode, where  $V_{ref} = -0.2 \text{ V}$ , and  $V_{ds} = 0.1 \text{ V}$ . The potential of  $V_{ref}$  was chosen to ensure that all ISFETs were operating far from their respective conductance minimum.

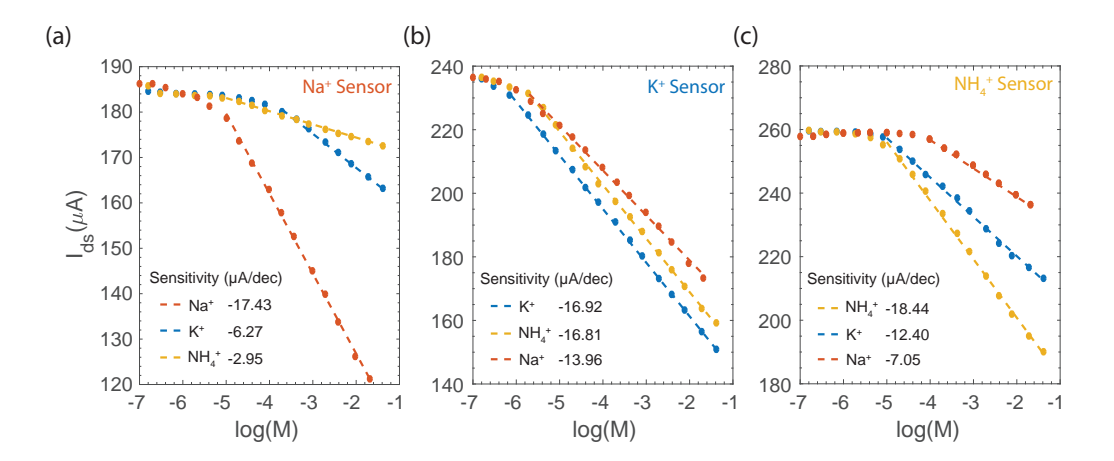


Fig. 6.5: The changes in  $I_{ds}$  for the cation ISFETs with respect to different cation concentrations using the separate solution method

Figs. 6.5 and 6.6 show the individual ISFETs' response to interfering ions. From this set of measurements, we can extract the selectivity coefficients  $K_{i,j}$ 

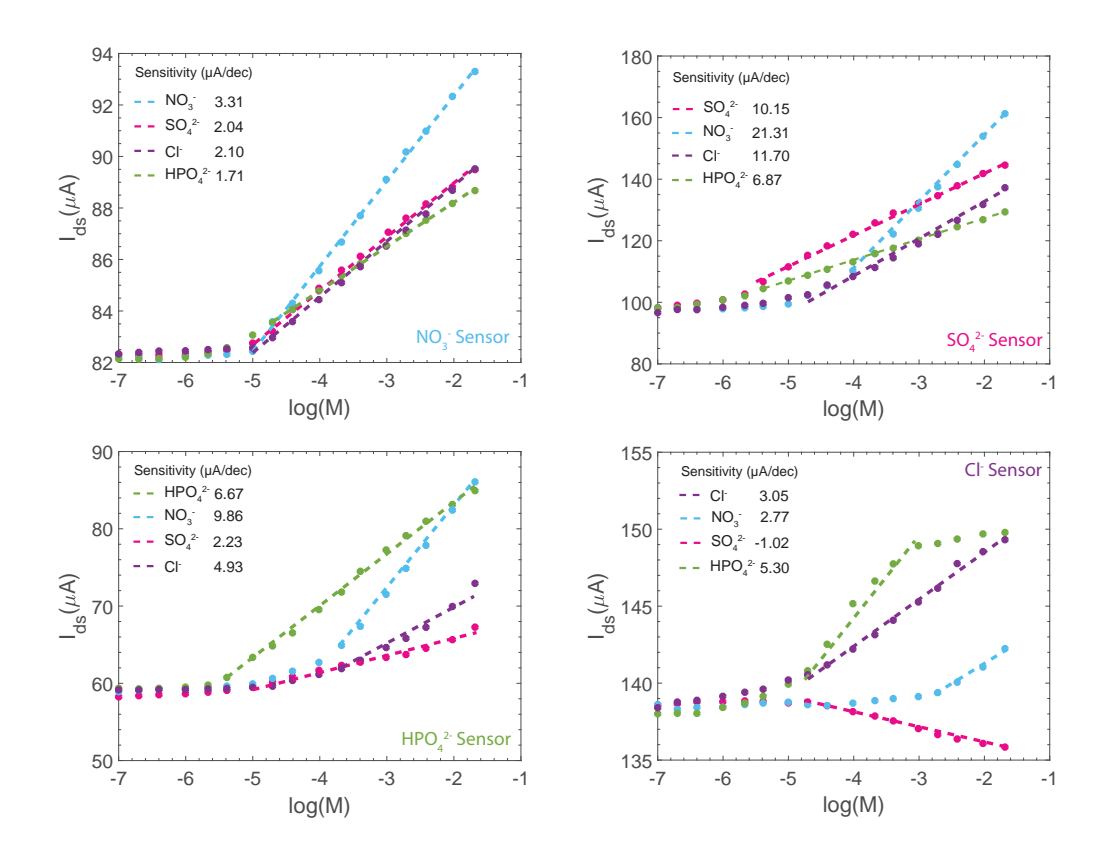


Fig. 6.6: The changes in  $I_{ds}$  for the anion ISFETs with respect to different anion concentrations using the separate solution method

and generate a series of equations to calculate the concentration of the ions in multiple analyte solutions. Firstly, since the ISFET response is measured as current and not voltage, the Nikolskii-Eisenman eq. 6.2 is rewritten as

$$I_i = I_i^0 + s_{ii} \log \left( a_i + \sum_{j \neq i} K_{i,j} a_j^{s_{ij}/s_{ii}} \right)$$
 (6.3)

where  $I_i$  is the current  $I_{ds}$  for sensor i,  $I_i^0$  is the current constant,  $s_{ii}$  is the current sensitivity for the ith sensor for the target ion i and  $s_{ij}$  is its current sensitivity for interfering ion j. Since the sensors have different sensitivities for

different ions despite having the same valency, the activity of the interfering ions is raised to the power of the ratio of sensitivities instead of the ratio of charge number (valency). When the sensors are placed in a solution only containing their respective target ion i, eq. 6.3 becomes

$$I_i = I_i^0 + s_{ii} \log(a_i) \tag{6.4}$$

which is a linear equation between current  $I_i$  and log concentration  $\log(a_i)$ . When the same sensor is being measured versus the concentration of an interfering ion j, eq. 6.3 becomes

$$I_i = I_i^0 + s_{ii} \log(K_{i,j} a_j^{s_{ij}/s_{ii}})$$
(6.5)

and can be written as

$$I_i = I_i^0 + s_{ij} \log(K_{i,j}) + s_{ij} \log(a_i)$$
(6.6)

which is also a linear equation between current  $I_i$  and log concentration  $\log(a_j)$ , and  $I_{ij}^0 = I_i^0 + s_{ii} \log(K_{i,j})$  is a constant. From the linear fits of  $I_i$  versus  $\log(a_j)$  in Figs. 6.5 and 6.6,  $K_{i,j}$  can be solved, where

$$K_{i,j} = 10^{(I_{ij}^0 - I_i^0)/s_{ii}} (6.7)$$

Tables 6.1 and 6.2 show the selectivity coefficients  $K_{i,j}$  for the cation and anion sensors respectively. For the cations, the K<sup>+</sup> ISFET is the most affected from the other cations. For the anions, due to the difference in valency, both

 $SO_4^{2-}$  and  $HPO_4^{2-}$  ISFETs are more sensitive to  $NO_3^-$  than their respective primary ions. As for the  $Cl^-$  ISFET, it is more sensitive to  $HPO_4^{2-}$  than  $Cl^-$ . Nevertheless, now that we have all the constants, we can infer the concentrations of all the ions in our study with the ISFETs, even in the presence of mixed solutions.

**Table 6.1**: Nikolskii selectivity coefficients for the cation ISFETs with respect to the different cations.

	$ m Na^+$	$\mathbf{K}^{+}$	$\mathbf{NH}_4^+$	
Na <sup>+</sup> ISFET	-	$9.13 \times 10^{-4}$	$1.99 \times 10^{-4}$	
K <sup>+</sup> ISFET	$6.45 \times 10^{-2}$	-	$3.16\times10^{-1}$	
$\mathbf{NH}_4^+$ ISFET	$2.13 \times 10^{-3}$	$2.14 \times 10^{-2}$	-	

**Table 6.2**: Nikolskii selectivity coefficients for the anion ISFETs with respect to the different anions.

	$\mathbf{NO}_3^-$	$\mathbf{SO}_4^{2-}$	$\mathbf{HPO}_4^{2-}$	Cl <sup>-</sup>
$\mathbf{NO}_3^-$ ISFET	-	$1.47 \times 10^{-2}$	$6.11 \times 10^{-3}$	$1.98 \times 10^{-2}$
${f SO}_4^{2-}$ ISFET	$8.85 \times 10^{3}$	-	$8.27 \times 10^{-3}$	$3.75 \times 10^{-1}$
$oxed{HPO_4^{2-} \ ISFET}$	$1.66 \times 10^{0}$	$1.09 \times 10^{-4}$	-	$2.10 \times 10^{-3}$
Cl <sup>-</sup> ISFET	$1.51 \times 10^{-3}$	$1.38 \times 10^{-7}$	$1.28 \times 10^{2}$	-

### 6.5 Multiple Analyte Sensing in Real-Time

With the relationship between the seven ISFETs and the different ions now mapped out, we tested them in multi analyte electrolytic solutions. The ISFETs were placed in a solution while their currents  $I_{ds}$  were measured in real time with  $V_{ref} = -0.2$  V and  $V_{ds} = 0.1$  V. The electrolytic solution was spiked

with different salt mixtures to alter the ion concentrations, and instantaneous changes in the currents were observed as seen in Fig. 6.7(a).

The ion concentrations of the solution were calculated from the measured currents using a set of equations eq. 6.3, one for each sensor. The cations and anions were solved separately since the counter-ions do not have any observable effect on sensor response. Fig. 6.7 (b) and (c) show the calculated concentration for cations and anions respectively with respect to time for the same measurement in Fig. 6.7(a). Despite the ISFETs responding to interfering ions, the non-linear system held up well, and changes in the calculated concentrations only occurred when their respective ions were added. The solution of the nonlinear system of equations failed at some points in time for the anions, where no real solutions can be determined, and these points are omitted from the plot. The failure is most likely due to the relatively poor current sensitivity of both the  $Cl^-$  and  $NO_3^-$  ISFETs.

The calculated concentrations were compared to the concentrations determined from the volume and mass of the added salts. Fig. 6.8 compares the expected and calculated concentrations for all seven ISFETs in the one minute time-frame represented by the grey shaded area in both Fig. 6.7(b) and (c). For the cations, the calculated concentrations are accurate within  $\pm 0.01 \log$  concentration, while the anions, due to a more complex interference relationship and lower sensitivities, are accurate within  $\pm 0.05 \log$  concentration. These accuracies are on par with spectrophotometric and chromatographic techniques.

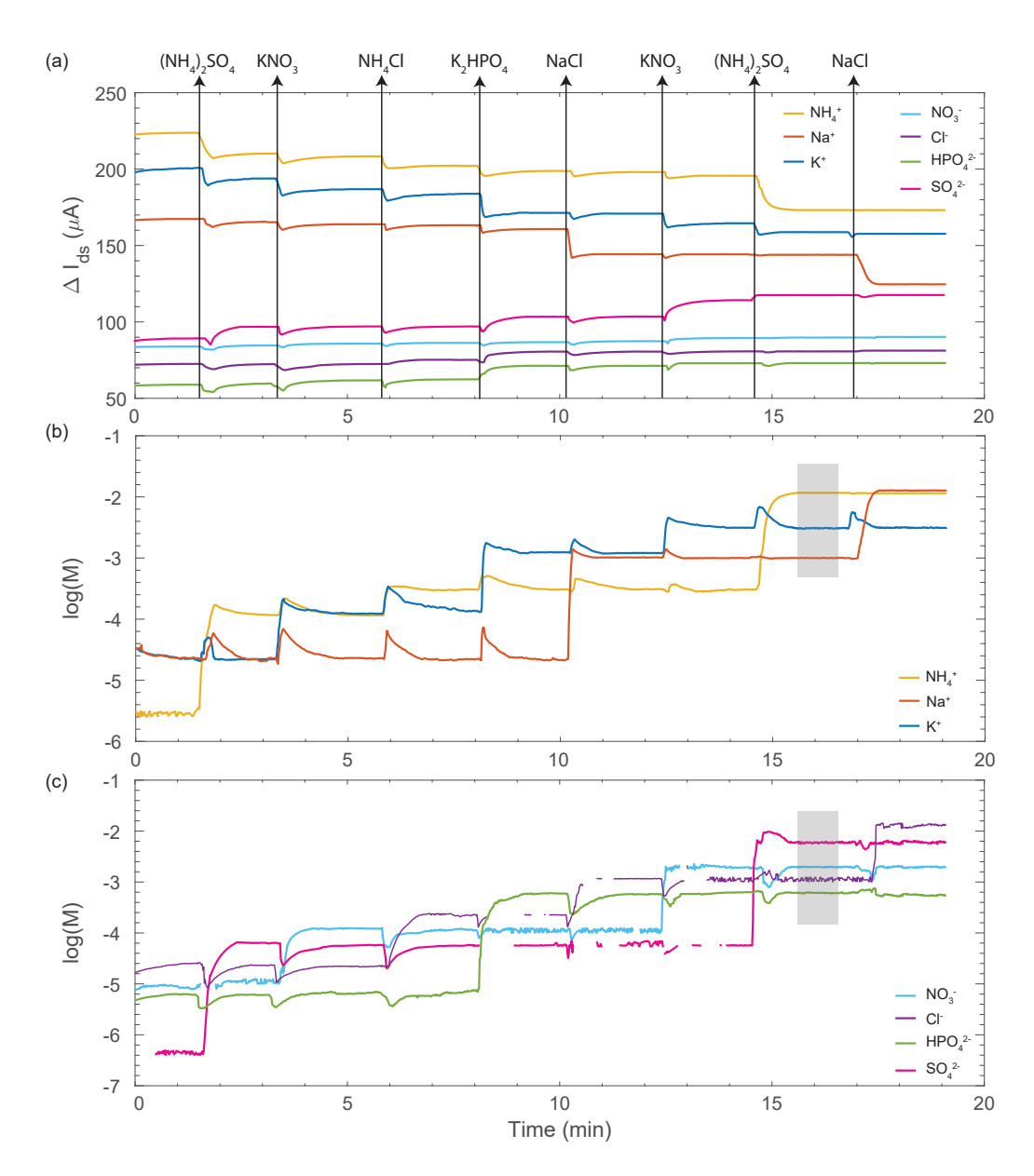
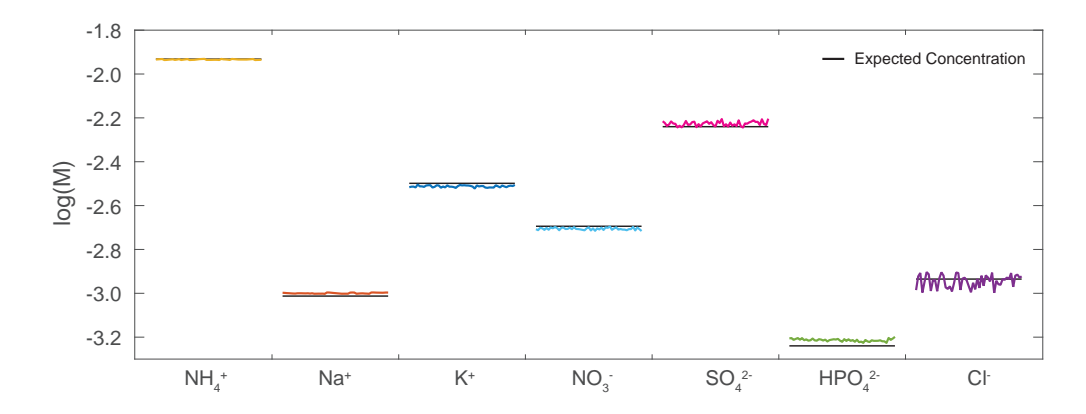


Fig. 6.7: (a) The change in current  $I_{ds}$  for all seven ISFETs measured concurrently in a complex electrolytic solution. The solution was spiked at different intervals with salt mixtures, illustrated by the arrows. (b), (c) The calculated concentrations of the cations and anions from the measured currents and solution of the nonlinear Nikolskii-Eisenman equations.



**Fig. 6.8**: The accuracy of our ISFET sensors by comparing the calculated concentrations in the shaded time window of Fig. 6.7 with the prepared concentrations as determined from the volume of the mixtures and added salts.

# 6.6 Monitoring Ion Concentrations in Complex

**Environment** 

The ISFET array was also tested in a more realistic application, where the ion concentrations were monitored in an aquarium with duckweed as seen in Fig. 6.9. Duckweed (genus Lemna) is a flowering aquatic plant that grow ubiquitously in fresh or polluted water throughout the world. To sustain growth, they require minerals including  $K^+$ ,  $NH_4^+$ ,  $Cl^-$ ,  $HPO_4^{2-}$  and  $SO_4^{2-}$  [92]. After placing the plants in an aquarium only containing tap water, the ion concentrations were more monitored with the ISFET array once a day over a period of three weeks. The plants were provided light 12 hours a day. After one week,  $(NH_4)_2SO_4$ ,  $K_2HPO_4$  and  $NH_4Cl$  were added to the aquarium to set the ion concentrations at  $\sim 3 \times 10^{-3}$  M for  $NH_4^+$  and  $Cl^-$ , and around  $\sim 5 \times 10^{-4}$  M for  $K^+$ ,  $SO_4^{2-}$  and  $HPO_4^{2-}$ . From Fig. 6.9(b) it can be seen that the ion concentration start to decrease with time. To confirm that the decrease in ion

concentrations was indeed due to duckweed intake, a control experiment was performed at the same time, under the same conditions, but without the duckweed. The ion concentrations remained constant after adding the salts in the control sample.

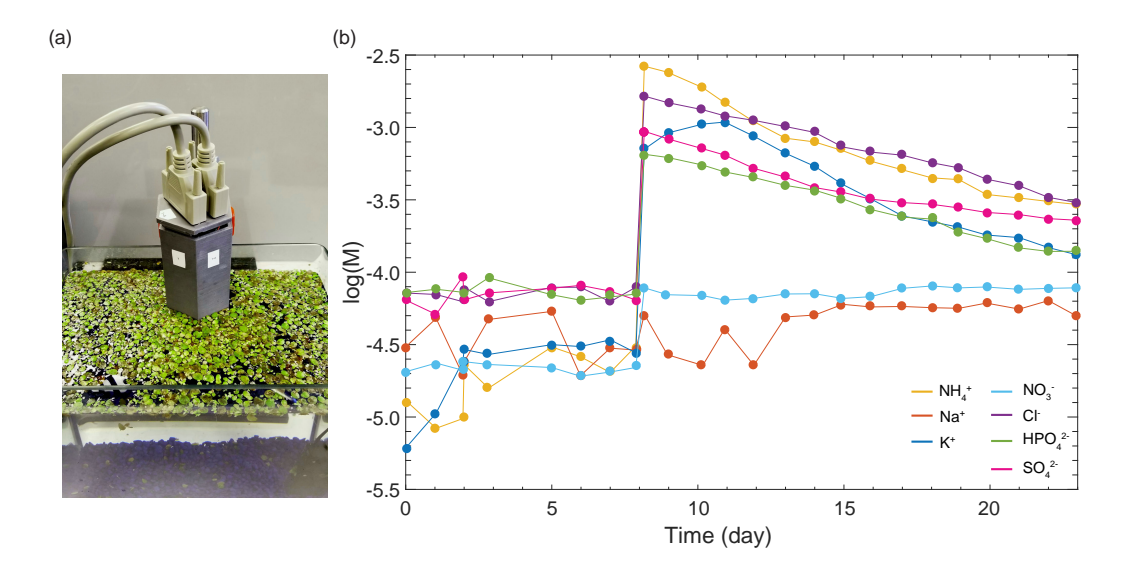


**Fig. 6.9**: (a) An optical image of the ISFET array in the aquarium containing duckweed while measuring ion concentrations. (b) The ion concentrations in the aquarium with the duckweed over the course of three weeks.

In conclusion, we were able to overcome the challenge of poor selectivity in potentiometric sensors by fabricating an array of large area graphene ISFETs. They have the advantage of being easily and inexpensively fabricated as large devices which is critical for achieving a high signal-to-noise-ratio and high resolution sensing. We use the separate solution method to extract the selectivity coefficients of the ISFETs and use a modified version of Nikolskii-Eisenman theory to calculate the concentrations of the ions. Despite the presence of heavily interfering ions, we were able to reach detection limits down to at least

 $10^{-5}$  M concentration, were accurate to within  $\pm 0.01$  and  $\pm 0.05$  log concentration for cations and anions respectively and were resolvable down to at least  $\sim 2 \times 10^{-2}$  log M. These sensor characteristics exceed the requirements for many real-time monitoring applications, and we demonstrate one such application by monitoring the uptake of ions by aquatic plants over the course of three week. The approach outlined here could be expanded upon, by incorporating more ISFETs into the array for different target ions, and utilizing them in even more complex applications.

# Chapter 7

## Conclusions and Future Work

While there are different techniques for measuring ion concentrations, only potentiometric sensors offer on-site and real time capabilities, which are necessary for many applications. However, they have yet to realize their full potential due to poor sensing resolution and selectivity. In this work, we overcome these challenges with large area graphene ISFETs, and our proof-of-principle experiments demonstrate that they are attractive candidates for real time sensing applications. In this chapter, the key findings and contributions are summarized, and we provide further ideas to improve graphene ISFETs for real-world applications.

#### 7.1 Key Findings and Contributions

We first presented a simple SNR model for ISFETs, whereby due to a thermodynamically limited signal, decreasing the ISFET noise is necessary for improving the SNR and therefore resolution. In the limit of a large transistor transconductance  $g_m$ , the ISFET noise is dominated by the charge fluctuation at the sensing layer. Therefore, to maximize the SNR, and in turn the ISFET resolution, it is necessary to maximize carrier mobility, device capacitance and device area. Consequently, graphene is an ideal material system to provide large-area devices with high charge-carrier mobility and high capacitive coupling to realize high resolution ion sensing.

We then developed large area graphene ISFETs ( $\sim 1 \times 1 \text{ cm}^2$ ) for measuring pH with a tantalum pentoxide Ta<sub>2</sub>O<sub>5</sub> sensing layer, whereby we showed that 150 nm of oxide grown via ALD is required to achieve high quality stochiometric oxide with complete coverage. With these devices, we were able to achieve a Nernstian limited response with graphene ISFETs for the first time. However, the thick oxide layers decreased capacitance significantly, as well as compromised the quality of the graphene by lowering the device mobility.

To overcome the challenges of ALD of metal oxides on graphene, we encapsulated the graphene with ultrathin layers of parylene C ( $\sim 4$  - 8 nm) to protect the graphene and to act as a seeding layer during ALD. As a result, we were able to achieve high quality stochiometric oxide with complete coverage with only 3 nm of metal oxide. Not only did these large area devices operate at the Nernst limit, but the device capacitance approached the quantum limit, and device mobilities were  $\sim 7000~\rm cm^2/Vs$ . Consequently, we observed record resolutions of 0.3 mpH for potentiometric sensors and which is on par with spectrophotometric and chromatographic techniques.

We then expanded this concept to detect other ions by substituting the oxide sensing layer with an ionophore membrane. We first demonstrated this for  $K^+$  ions and their respective ionophore, potassium ionophore III. The parylene encapsulated ISFETs were shown to achieve record detection limits of  $10^{-9}$  M, equivalent to 39 ng/L, as well as record resolutions of  $2\times10^{-3}$  log concentration for potentiometric  $K^+$  sensors. The devices also exhibited remarkable reversibility and stability over a 5 month period with minimal drift.

To overcome the issue of poor selectivity, we applied the Nikolskii-Eisenman equation, a modified Nernst equation, which includes weighted activity terms to account for ion cross-sensitivity. An ISFET array was developed for measuring the following ions:  $K^+$ ,  $Na^+$ ,  $NH_4^+$ ,  $NO_3^-$ ,  $SO_4^{2-}$ ,  $HPO_4^{2-}$  and  $Cl^-$ . The sensors were cross calibrated for interfering ions, and a series of equations was generated to solve for the ion concentrations, even in the presence of interfering ions. With this method, the ISFETs were accurate in multi analyte solutions to within  $\pm 0.01$  and  $\pm 0.05 \log$  concentration for cations and anions respectively.

Our devices were tested in multiple real-time applications to test their viability, and exhibited very promising results. The change in pH of carbonated water was observed as the carbon dioxide desorbed over time. K<sup>+</sup> concentration in beverages and blood was measured and compared to current state-of-the-art methods. The ion concentrations in an aquarium containing duckweed was also studied over three weeks, as the duckweed absorbed minerals to sustain its growth.

Finally, we demonstrated the viability of mass producing the graphene ISFETs with wafer scale processing in an economical fashion, making it much more cost effective than current techniques for measuring ions. Table 1.1 has

been modified to include our graphene ISFETs, and it shows the promise of these sensors. The current cost for our individual graphene ISFET is \$45, based on prototyping quantities; however, with economies of scale this should go down to less than \$5. An ISFET array with 40 sensors is estimated to retail at around \$3,000, which includes a meter and reference electrode. However, there remains further work to improve and characterize graphene ISFETs prior to their use in real world environmental monitoring.

**Table 7.1**: Comparison of the different analytical techniques for measuring ion concentration, including our graphene ISFETs

Technique	Selectivity	Resolution	Detection limit	Accuracy	Price
Chromatography	High	$10^{-4} \log M$	$10^{-10} { m M}$	$\pm$ 0.03 log M	> \$50,000
Spectrophotometry	High	$10^{-4} \log M$	$10^{-10} { m M}$	$\pm$ 0.03 log M	> \$10,000
Potentiometric ISE with meter	Poor	$10^{-2} \log M$	$10^{-6} { m M}$	$\pm$ 0.05 log M	\$2,000
Graphene ISFET array with meter	High	$10^{-3} \log M$	$10^{-9} { m M}$	$\pm$ 0.03 log M	\$3,000

#### 7.2 Future work

#### 7.2.1 Challenges with Parylene Encapsulation

In this work, we have shown that encapsulating parylene protects the graphene from degradation as well as acts as a seeding layer for ALD of metal oxides for sensing pH. Despite the encapsulating layer being only  $\sim$  4-8 nm, it still contributes to the overall capacitance of the device. It would be difficult to fabricate a thinner layer without compromising the graphene quality. Therefore, if there was a need to further improve the resolution, the parylene can be substituted with a hydrophobic, chemically inert, 2D insulator such

7.2 Future work 101

as hBN [93]. The atomic thinness of 2D insulators will admit gate capacitances even closer to the quantum limit. However, synthesis of large area hBN still has many challenges [94], making it some years away before it can be implemented with wafer scale processing. Furthermore, hBN has the same problem as graphene, where it does not have any dangling bonds, inhibiting ALD growth of metal oxides. Therefore, if hBN were to be the encapsulating material, it can only be used with ionophore membranes as sensing layers.

The other challenge with parylene is its reaction with the THF in the ionophore mixture. This reaction is not fully understood at the moment, but it does lead to a degradation in the dielectric properties of the parylene and heavily dopes the graphene. In some instances, the ISFETs were very unstable and not used as sensors. THF is the solvent of choice for ionophore membranes in order for it to dissolve the PVC and would be difficult to replace. One solution is to substitute the parylene with polytetrafluoroethylene (PTFE). PTFE is a hydrophobic, chemically inert polymer [95] which is not affected by THF [96]. CVD of ultra-thin layers of PTFE (~ 18 nm) of PTFE has been demonstrated on different substrates in 2019 [97]. Another solution is to encapsulate the parylene with an ultra-thin layer of oxide to protect it from the THF; however, the oxide should not be sensitive to pH, as the PVC membrane is permeable.

#### 7.2.2 Challenges with the Reference Electrode

A reference electrode is necessary for any potentiometric sensor to ensure a stable electrode potential, and therefore a stable measurement. Reference elec-

trodes function as a redox system, where a chemical reaction occurs between ions in the electrode. The Ag/AgCl reference electrode used in our experiments consists of a silver wire coated with silver chloride immersed in a high concentration KCl solution to stabilize the silver chloride reaction, and ensure a stable redox system. The electrode and solution are housed in a plastic body with a porous plug separating the electrode electrolyte from the field environment under measurement. The difference in concentrations between the electrode electrolyte and the field environment creates a liquid junction potential. Over time, the electrode electrolyte can leak into the field environment, varying the liquid junction potential, and creating errors in measurement [98]. Over time, variations in the liquid junction potential can reach up to  $\pm 2$  mV, and assuming a Nernstian limited response from the ISFETs, this could affect the accuracy of our ISFETs by  $\pm$  0.03 log concentrations. Most commercial reference electrodes on the market are also liquid junction electrodes and face similar challenges. Another issue is that they are quite bulky compared to our solid state sensors, making the ISFET unpractical for some applications such as wearable sensors.

Recently, it has been shown that replacing the KCl electrolyte with an ionic liquid gel overcomes the issues with leakage and variation of the liquid junction potential [99]. For our ISFETs, we can potentially integrate an Ag/AgCl electrode onto our PCB, and coat it with the ionic liquid gel. This will simultaneously improve stability and enable a more compact and rigid structure.

7.2 Future work 103

#### 7.2.3 Printed ISFETs

Advances in printable electronics, which combines conventional printing methods with conducting and semiconducting inks to economically produce electronic devices in a high throughput fashion, has widened the potential of potentiometric sensors. Industries are looking to incorporate them in food packaging and wearables. The challenge is fabricating high performance graphene ISFETs using printing methods. While there are many graphene inks on the market, they do not share the same properties as single layer graphene which is essential for ISFETs. However, with advances in roll-to-roll graphene manufacture [37], graphene rolls can be fed into printing machines, where inks can etch the graphene into the required dimensions, and metallic inks can be used as contacts, and the reference electrode. The ionic liquid gel for the reference electrode could be used as an ink for printing, while the ionophore mixtures can be modified to dry quickly while printing.

In summary, large-area graphene ISFETs are ideal for measuring ions at low concentrations. Their performance in terms of detection limits, accuracy, resolution and selectivity is on par with spectrophotometric and chromatographic techniques, yet they are compact and robust for on-site and real-time measurements. After overcoming some challenges regarding stability and the reference electrode, these sensors may find use in environmental monitoring and other real world applications.

- [1] J. M. Rothberg, W. Hinz, T. M. Rearick, J. Schultz, W. Mileski, M. Davey, J. H. Leamon, K. Johnson, M. J. Milgrew, M. Edwards, J. Hoon, J. F. Simons, D. Marran, J. W. Myers, J. F. Davidson, A. Branting, J. R. Nobile, B. P. Puc, D. Light, T. A. Clark, M. Huber, J. T. Branciforte, I. B. Stoner, S. E. Cawley, M. Lyons, Y. Fu, N. Homer, M. Sedova, X. Miao, B. Reed, J. Sabina, E. Feierstein, M. Schorn, M. Alanjary, E. Dimalanta, D. Dressman, R. Kasinskas, T. Sokolsky, J. A. Fidanza, E. Namsaraev, K. J. McKernan, A. Williams, G. T. Roth, J. Bustillo, An integrated semiconductor device enabling non-optical genome sequencing, Nature 475 (2011) 348–352.
- [2] A. D. Chapp, S. Schum, J. E. Behnke, T. Hahka, M. J. Huber, E. Jiang, R. A. Larson, Z. Shan, Q. Chen, Measurement of cations, anions, and acetate in serum, urine, cerebrospinal fluid, and tissue by ion chromatography, Physiol Rep. 6 (7) (2018) e13666.
- [3] Protocols manual for water quality sampling in Canada, Canadian Council of Ministers of the Environment, 2011.
- [4] Developing Drinking Water Quality Regulations and Standards, World Health Organization, 2018.
- [5] T. R. Martz, J. G. Connery, K. S. Johnson, Testing the honeywell durafet for seawater pH applications, Limnol. Oceanogr. Methods 8 (5) (2010) 172–184.
- [6] What are the Essentials of pH in Industrial Applications? URL https://automation.isa.org/what-are-the-essentials-of-ph-in-industrial-applications/
- [7] S. S. Nielsen, Food Analysis Laboratory Manual, Springer International Publishing, 2017.

[8] J. Weiss, Handbook of Ion Chromatography, third, completely revised and enlarged edition Edition, John Wiley and Sons, Inc, 2005.

- [9] R. B. Fulton, B. Kratochvi, Measurement of free ion concentrations by spectrophotometry: The sample ion increment method, Anal. Chem. 52 (3) (1980) 546–552.
- [10] S. Aßmann, C. Frank, A. Kortzinger, Spectrophotometric high-precision seawater ph determination for use in underway measuring systems, Ocean Sci. 7 (5) (2011) 597–607.
- [11] N. Gros, M. F. Camòes, C. Oliveira, M. C. R. Silva, Ionic composition of seawaters and derived saline solutions determined by ion chromatography and its relation to other water quality parameters, Journal of Chromatography A 1210 (1) (2008) 92–98.
- [12] St. Lawrence River: Monitoring Water Quality. URL https://www.canada.ca/en/environment-climate-change/ services/st-lawrence-river/water-sediment/monitoring-waterquality.html
- [13] A. J. Bard, L. R. Faulkner, Electrochemical Methods: Fundamentals and Applications, John Wiley and Sons, 2001.
- [14] E. Bakker, P. Bühlmann, E. Pretsch, Carrier based ion-selective electrodes and bulk optodes, Chem. Rev. 97 (1997) 3083–3132.
- [15] P. Bergveld, Thirty years of ISFETOLOGY: What happened in the past 30 years and what may happen in the next 30 years, Sens. Actuators B 88 (1) (2003) 1–20.
- [16] P. Bergveld, Development of an ion-sensitive solid-state device for neuro-physiological measurements, IEEE BME 17 (1970) 70–71.
- [17] Ion Concentraion Measurements (ISE).

  URL https://www.thermofisher.com/ca/en/home/life-science/
  lab-equipment/ph-electrochemistry/ion-concentrationmeasurement-ise/ise-electrodes-standards-solutions.html
- [18] M. Shibata, M. Kato, Y. Iwamoto, S. Nomura, T. Kakiuchi, Potentiometric determination of pH values of dilute sulfuric acid solutions with glass combination electrode equipped with ionic liquid salt bridge, J. Electroanal. Chem. 705 (2013) 81–85.

[19] K. Bedner, V. A. Guzenko, A. Tarasov, M. Wipf, R. L. Stoop, S. Rigante, J. Brunner, W. Fu, C. David, M. Calame, J. Gobrecht, C. Schönenberger, Investigation of the dominant 1/f noise source in silicon nanowire sensors, Sens. Actuators B 191 (2014) 270–275.

- [20] R. E. G. van Hal, J. C. T. Eijkel, P. Bergveld, A novel description of isfet sensitivity with the buffer capacity and double-layer capacitance as key parameters, Sens. Actuators B 24 (1-3) (1995) 201–205.
- [21] N. Moser, T. S. Lande, C. Toumazou, P. Georgiou, Isfets in cmos and emergent trends in instrumentation: A review, IEEE Sensors Journal 16 (17) (2016) 6496–6514.
- [22] B. Razavi, Design of Analog CMOS Integrated Circuits, McGraw-Hill, 2000.
- [23] O. Knopfmacher, A. Tarasov, W. Fu, M. Wipf, B. Niesen, M. Calame, C. Schönenberger, Nernst limit in dual-gated si-nanowire fet sensors, Nano Lett. 10 (2010) 2268–2274.
- [24] K. Nishiguchi, N. Clement, T. Yamaguchi, A. Fujiwara, Si nanowire ionsensitive field-effect transistors with a shared floating gate, Appl. Phys. Lett. 94 (2009) 163106.
- [25] S. Kim, T. Rim, K. Kim, U. Lee, E. Baek, H. Lee, C.-K. Baek, M. Meyyap-pan, M. J. Deen, J.-S. Lee, Silicon nanowire ion sensitive field effect transistor with integrated Ag/AgCl electrode: pH sensing and noise characteristics, Analyst 136 (2011) 5012–5016.
- [26] M. Myers, F. Khir, A. Podolska, G. Membreno, B. Nener, M. Baker, G. Parish, Nitrate ion detection using AlGaN/GaN heterostructure-based devices without a reference electrode, Sens. Actuators B 181 (2013) 301– 305.
- [27] Y.-H. Chang, Y.-S. Lu, Y.-L. Hong, S. Gwo, J. A. Yeh, Highly sensitive ph sensing using an indium nitride ion-sensitive field-effect transistor, IEEE 11 (5) (2011) 1157–1161.
- [28] H. Wang, P. Zhao, X. Zeng, C. D. Young, W. Hu, High-stability ph sensing with a few-layer mos<sub>2</sub> field-effect transistor, Nanotechnology 30 (2019) 375203.

[29] D. Sarkar, W. Liu, X. Xie, A. C. Anselmo, S. Mitragotri, K. Banerjee, Mos<sub>2</sub> field-effect transistor for next generation label-free biosensors, ACS Nano 8 (4) (2014) 3992–4003.

- [30] C. C. Cid, J. Riu, A. Maroto, F. X. Rius, Ion-sensitive field effect transistors using carbon nanotubes as the transducing layer, Analyst 133 (2008) 1001–1004.
- [31] F. Schedin, A. K. Geim, S. V. Morozov, E. Hill, P. Blake, M. I. Katsnelson, K. S. Novoselov, Detection of individual gas molecules adsorbed on graphene, Nat. Mater. B 6 (2007) 652–655.
- [32] K. S. Novoselov, A. K. Geim, S. V. Morozov, D. Jiang, Y. Zhang, S. V. Dubonos, I. V. Grigorieva, A. A. Firsov, Electric field effect in atomically thin carbon films, Science 306 (5696) (2004) 666–669.
- [33] The nobel prize in physics 2010.
  URL https://www.nobelprize.org/prizes/physics/2010/summary/
- [34] K. V. Emtsev, A. Bostwick, K. Horn, J. Jobst, G. L. Kellogg, L. Ley, J. L. McChesney, T. Ohta, S. A. Reshanov, J. Rohrl, E. Rotenberg, A. K. Schmid, D.Waldmann, H. B.Weber, T. Seyller, Towards wafer-size graphene layers by atmospheric pressure graphitization of silicon carbide, Nat. Mater. 8 (3) (2009) 203–207.
- [35] X. S. Li, W. W. Cai, J. H. An, S. Kim, J. Nah, D. X. Yang, R. Piner, A. Velamakanni, I. Jung, E. Tutuc, S. K. Banerjee, L. Colombo, R. S. Ruo, Large-area synthesis of high-quality and uniform graphene films on copper foils, Science 324 (5932) (2009) 1312–1314.
- [36] S. Rahimi, L. Tao, S. F. Chowdhury, S. Park, A. Jouvray, S. Buttress, N. Rupesinghe, K. Teo, D. Akinwande, Toward 300 mm wafer-scalable high-performance polycrystalline chemical vapor deposited graphene transistors, ACS Nano 8 (10) (2014) 10471–10479.
- [37] T. Kobayashi, M. Bando, N. Kimura, K. Shimizu, K. Kadono, N. Umezu, K. Miyahara, S. Hayazaki, S. Nagai, Y. Mizuguchi, Y. Murakami, D. Hobara, Production of a 100-m-long high-quality graphene transparent conductive film by roll-to-roll chemical vapor deposition and transfer process, Appl. Phys. Lett. 102 (2) (2013) 023112.
- [38] T. Fang, A. Konar, H. Xing, D. Jena, Carrier statistics and quantum capacitance of graphene sheets and ribbons, Appl. Phys. Lett. 91 (19) (2007) 092109.

[39] A. H. C. Neto, F. Guinea, N. M. R. Peres, K. S. Novoselov, A. K. Geim, The electronic properties of graphene, Rev. of Mod. Phys. 81 (1) (2009) 109–162.

- [40] J. Xia, F. Chen, J. Li, N. Tao, Measurement of the quantum capacitance of graphene, Nat. Nano. 91 (2009) 505–509.
- [41] J.-H. Chen, C. Jang, S. Xiao, M. Ishigami, M. S. Fuhrer, Intrinsic and extrinsic performance limits of graphene devices on SiO<sub>2</sub>, Nat. Nano. 3 (10) (2008) 206–209.
- [42] D. D. Fazio, D. G. Purdie, A. K. Ott, P. Braeuninger-Weimer, T. Khod-kov, S. Goossens, T. Taniguchi, K. Watanabe, P. Livreri, F. H. L. Koppens, S. Hofmann, I. Goykhman, A. C. Ferrari, A. Lombardo, Highmobility, wet-transferred graphene grown by chemical vapor deposition, ACS Nano 13 (8) (2019) 8926–8935.
- [43] F. Schwierz, Graphene transistors, Nat. Nano. 5 (7) (2010) 487–496.
- [44] P. Blake, E. W. Hill, A. H. C. Neto, K. S. Novoselov, D. Jiang, R. Yang, T. J. Booth, A. K. Geim, Making graphene visible, Appl. Phys. Lett. 91 (6) (2007) 063124.
- [45] F. Chen, Q. Qing, J. Xia, N. Tao, Graphene field-effect transistors: Electrochemical gating, interfacial capacitance, and biosensing applications, Chem. Asian J. 5 (2010) 2144–2153.
- [46] I. Heller, A. M. Janssens, J. Mannik, E. D. Minot, S. G. Lemay, C. Dekker, Identifying the mechanism of biosensing with carbon nanotube transistors, Nano Lett. 8 (2) (2008) 591–595.
- [47] R. Lanche, V. Pachauri, W.-M. Munief, A. Müller, M. Schwartz, P. Wagner, R. Thoelen, S. Ingebrandt, Graphite oxide electrical sensors are able to distinguish single nucleotide polymorphisms in physiological buffers, FlatChem 1 (9) (2018) 2452–2627.
- [48] F. Chen, J. Xia, N. Tao, Ionic screening of charged-impurity scattering in graphene, Nano Lett. 9 (4) (2009) 1621–1625.
- [49] F. Chen, Q. Qing, J. Xia, J. Li, N. Tao, Electrochemical gate-controlled charge transport in graphene in ionic liquid and aqueous solution, J. Am. Chem. Soc. 131 (29) (2009) 9908–9909.

[50] B. Mailly-Giacchetti, A. Hsu, H. Wang, V. Vinciguerra, F. Pappalardo, L. Occhipinti, E. Guidetti, S. Coffa, J. Kong, T. Palacios, ph sensing properties of graphene solution-gated field-effect transistors, J. Appl. Phys. 114 (8) (2013) 084505.

- [51] Z. Cheng, Q. Li, Z. Li, Q. Zhou, Y. Fang, Suspended graphene sensors with improved signal and reduced noise, Nano Lett. 10 (5) (2010) 1864–1868.
- [52] Y. Ohno, K. Maehashi, Y. Yamashiro, K. Matsumoto, Electrolyte-gated graphene field-effect transistors for detecting ph and protein adsorption, Nano Lett. 9 (9) (2009) 3318–3322.
- [53] W. Fu, C. Nef, A. Tarasov, R. S. M. Wipf, O. Knopfmacher, M. Weiss, M. Calame, C. Schönenberger, High mobility graphene ion-sensitive field-effect transistors by noncovalent functionalization, Nanoscale 5 (24) (2013) 12104.
- [54] W. Fu, C. Nef, O. Knopfmacher, A. Tarasov, M. Weiss, M. Calame, C. Schönenberger, Graphene transistors are insensitive to ph changes in solution, Nano Lett. 11 (9) (2011) 3597–3600.
- [55] J. Inczedy, T. Lengyel, A. Ure, Compendium of Analytical Nomenclature: Definitive Rules, International Union of Pure and Applied Chemistry, 1997.
- [56] D. E. Yates, S. Levine, T. W. Healy, Site-binding model of the electrical double layer at the oxide/water interface, J. Chem. Soc., Faraday Trans. 1 70 (1974) 1807–1818.
- [57] J. F. Dufrêche, O. Bernard, P. Turq, Transport in electrolyte solutions: are ions brownian particles?, Journal of Molecular Liquids 118 (1-3) (2005) 189–194.
- [58] H. Nyquist, Thermal agitation of electric charge in conductors, Phys. Rev 32 (1) (1928) 110.
- [59] I. Fakih, S. Sabri, F. Mahvash, M. Nannini, M. Siaj, T. Szkopek, Large area graphene ion sensitive field effect transistors with tantalum pentoxide sensing layers for pH measurement at the Nernstian limit, Appl. Phys. Lett. 105 (8) (2014) 083101.

[60] X. Wang, S. M. Tabakman, H. Dai, Atomic layer deposition of metal oxides on pristine and functionalized graphene, J. Am. Chem. Soc. 130 (26) (2008) 8152–8153.

- [61] R. H. J. Vervuurt, W. M. M. Kessels, A. A. Bol, Atomic layer deposition for graphene device integration, Adv. Mat. 4 (18) (2017) 1700232.
- [62] A. Guermoune, T. Chari, F. Popescu, S. S. Sabri, J. Guillemette, H. S. Skulason, T. Szkopek, M. Siaj, Chemical vapor deposition synthesis of graphene on copper with methanol, ethanol, and propanol precursors, Carbon 49 (13) (2011) 4204–4210.
- [63] S. S. Sabri, P. L. Levesque, C. M. Aguirre, J. Guillemette, R. Martel, T. Szkopek, Graphene field effect transistors with parylene gate dielectric, Appl. Phys. Lett. 95 (24) (2009) 242104.
- [64] P. L. Levesque, S. S. Sabri, C. M. Aguirre, J. Guillemette, M. Siaj, P. Desjardins, T. Szkopek, R. Martel, Probing charge transfer at surfaces using graphene transistors, Nano Lett. 11 (1) (2011) 132–137.
- [65] V. Barone, O. Hod, G. E. Scuseria, Electronic structure and stability of semiconducting graphene nanoribbons, Nano Lett. 6 (12) (2006) 2748– 2754.
- [66] D. D. Sarma, C. N. R. Rao, Xpes studies of oxides of second and thirdrow transition metals including rare earths, J. Electron Spectrosc. Relat. Phenom. 20 (1) (1980) 25–45.
- [67] S. F. Ho, S. Contarini, J. W. Rabalais, Ion-beam-induced chemical changes in the oxyanions (Moyn-) and oxides (Mox) where m=chromium, molybdenum, tungsten, vanadium, niobium and tantalum, J. Phys. Chem. 91 (18) (1987) 4779–4788.
- [68] G. E. McGuire, G. K. Schweitzer, T. A. Carlson, Core electron binding energies in some group IIIA, VB, and VIB compounds, Inorg. Chem. 12 (10) (1973) 2450–2453.
- [69] V. Nefedov, M. Firsov, I. Shaplygin, Electronic structures of MRhO<sub>2</sub>, MRh<sub>2</sub>O<sub>4</sub>, RhMO<sub>4</sub> and Rh<sub>2</sub>MO<sub>6</sub> on the basis of X-ray spectroscopy and esca data, J. Electron Spectrosc. Relat. Phenom. 26 (1) (1982) 65–78.
- [70] J. A. Alexander-Webber, A. A. Sagade, A. I. Aria, Z. A. V. Veldhoven, P. Braeuninger-Weimer, R. Wang, A. Cabrero-Vilatela, M.-B. Martin,

J. Sui, M. R. Connolly, S. Hofmann, Encapsulation of graphene transistors and vertical device integration by interface engineering with atomic layer deposited oxide, 2D Mater. 4 (1) (2016) 011008.

- [71] B. Fallahazad, K. Lee, G. Lian, S. Kim, C. M. Corbet, D. A. Ferrer, L. Colombo, E. Tutuc, Scaling of Al<sub>2</sub>O<sub>3</sub> dielectric for graphene field-effect transistors, Appl. Phys. Lett. 100 (9) (2008) 093112.
- [72] A. Hogg, T. Aellen, S. Uhl, B. G. abd H. Keppner, Y. Tardy, J. Burger, Ultra-thin layer packaging for implantable electronic devices, J. Micromech. Microeng. 23 (7) (2013) 075001.
- [73] G. N. Parsons, S. E. Atanasov, E. C. Dandley, C. K. Devine, B. Gong, J. S. Jur, K. Lee, C. J. Oldham, Q. Peng, J. C. Spagnola, P. S. Williams, Mechanisms and reactions during atomic layer deposition on polymers, Coord. Chem. Rev. 257 (23-24) (2013) 3323–3331.
- [74] G. Dhanaraj, K. Byrappa, V. Prasad, M. Dudley, Springer Handbook of Crystal Growth, Springer, 2010.
- [75] N. D. Spencer, Tailoring Surfaces Modifying Surface Composition and Structure for Applications in Tribology, Biology and Catalysis, World Scientific, 2011.
- [76] A. P. Shpak, P. P. Gorbyk, Nanomaterials and Supramolecular Structures, Springer, 2010.
- [77] M. Telting-Diaz, E. Bakker, Effect of lipophilic ion-exchanger leaching on the detection limit of carrier-based ion-selective electrodes.
- [78] Thermo scientific orion laboratory products catalog, Thermo Fisher Scientific, 2013.
  URL https://assets.thermofisher.com/TFS-Assets/LSG/Catalogs/ThermoScientific-Orion-Labratory-Catalog.pdf
- [79] HI4114-potassium combination ion selective electrode (ISE) (2018). URL https://hannainst.com/hi4114-potassium-combination-ion-selective-electrode.html
- [80] Cole-parmer combination ion-selective electrode (ISE), potassium (K<sup>+</sup>) (2018).
  URL https://www.coleparmer.ca/i/cole-parmer-combination-ion-selective-electrode-ise-potassium-k

[81] J. Pick, K. Toth, E. Pungor, A potassium-selective silicone-rubber membrane electrode based on a neutral carrier, Anal. Chim. Acta. 64 (3) (1973) 477–480.

- [82] CFR 355 The List of Extremely Hazardous Substances and Their Threshold Planning Quantities, United States Environmental Protection Agency.
- [83] W. S. Gibbons, H. M. Patel, R. P. Kusy, Effects of plasticizers on the mechanical properties of poly(vinyl chloride) membranes for electrodes and biosensors, Polymer 38 (11) (1997) 2633–2642.
- [84] L.-S. Park, Y.-J. Hur, B.-K. Sohn, Effect of membrane structure on the performance of field-effect transistor potassium-sensitive sensor, Sens. Actuators, B 57 (3) (1996) 239–243.
- [85] H. Lia, Y. Zhub, M. S. Islama, M. A. Rahmanc, K. B. Walshd, G. Koley, Graphene field effect transistors for highly sensitive and selective detection of K<sup>+</sup> ions, Sens. Actuators, B 253 (2017) 759–765.
- [86] B. P. Nikolskii, Theory of the glass electrode. I. theoretical, J. Phys. Chem. 10 (1937) 495–503.
- [87] G. Eisenman, D. O. Rudin, J. U. Casby, Glass electrode for measuring sodium ion, Science 126 (1957) 831–834.
- [88] S. Jørgensen, H. Löffler, W. Rast, M. Straskraba, Lake and Reservoir Management, Elsevier, 2005.
- [89] S. Jørgensen, B. D. Fath, Encyclopedia of Ecology, Elsevier, 2008.
- [90] K. J. Powell, P. L. Brown, R. H. Byrne, T. Gajda, G. H. S. Sjöberg, H. Wanner, Chemical speciation of environmentally significant heavy metals with inorganic ligands. Part 1: The Hg<sup>2+</sup>, Cl<sup>-</sup>, OH<sup>-</sup>, CO<sub>3</sub><sup>2-</sup>, SO<sub>4</sub><sup>2-</sup>, and PO<sub>4</sub><sup>3-</sup> in aquatic systems, Pure Appl. Chem. 77 (2005) 739–800.
- [91] G. G. Guilbault, R. A. Durst, M. S. Frant, H. Freiser, E. H. Hansen, T. S. Light, E. Pungor, G.Rechnitz, N. M. Rice, T. J. Rohm, W. Simon, J. D. R. Thomas, Recommendations for nomenclature of ion-selective electrodes, Pure Appl. Chem. 48 (1976) 127–132.
- [92] DUCKWEED: A tiny aquatic plant with enormous potential for agriculture and environment, World Watch, 1997.

[93] C. R. Dean, A. F. Young, I. Meric, C. Lee, L. Wang, S. Sorgenfrei, K. Watanabe, T. Taniguchi, P. Kim, K. L. Shepard, J. Hone, Boron nitride substrates for high-quality graphene electronics, Nat. Nanotech. 5 (2010) 722.

- [94] F. Mahvash, S. Eissa, T. Bordjiba, A. C. Tavares, T. Szkopek, M. Siaj, Corrosion resistance of monolayer hexagonal boron nitride on copper, Sci. Rep. 7 (2013) 42139.
- [95] J. R. Plunkett, Tetrafluoroethylene polymers.
- [96] Ptfe and teflon chemical compatibility chart.
  URL https://www.calpaclab.com/teflon-ptfe-compatibility/
- [97] S. Schröder, T. Strunsku, S. Rehders, K. K. Gleason, F. Faupel, Tunable polytetrafluoroethylene electret films with extraordinary charge stability synthesized by initiated chemical vapor deposition for organic electronics applications, Sci. Rep. 9 (2019) 2237.
- [98] R. Kadis, I. Leit, Evaluation of the residual liquid junction potential contribution to the uncertainty in ph measurement: A case study on low ionic strength natural waters, Anal. Chim. Acta 664 (2010) 129–135.
- [99] M. Shibata, M. Yamakuni, Y. Iwamoto, S. Nomura, T. Kakiuishi, Stability of a Ag/AgCl reference electrode equipped with an ionic liquid salt bridge composed of 1-methyl-3-octylimidazolium bis(trifluoromethanesulfonyl)-amide in potentiometry of ph standard buffers, Anal. Sci. 26 (2010) 1203–1206.